A FRACTURE MECHANICS STUDY OF THE FRACTURE TOUGHNESS TESTING TECHNIQUES APPLIED TO BRITTLE MATERIALS

by

Thevashen Naidu B.Sc. Eng. (Materials), (Cape Town)

A thesis submitted to the Faculty of Engineering, University of Cape Town, in partial fulfillment of the academic requirements for the degree of Master of Science in Engineering (June 2002).

ABSTRACT

This dissertation describes an investigation into the application of fracture mechanics to brittle materials, with particular emphasis on the fracture toughness testing techniques used on these materials.

A comprehensive literature review on the fracture mechanics principles, and fracture toughness testing techniques of brittle materials was undertaken to develop understanding and competence in this field. Fracture toughness testing techniques have been generally classified into two categories – (a) specimens with *macronotches*, and (b) specimens with indentation induced *microflaws*. The *macronotch* test techniques are generally well recognized, with some of them standardised, while the *microflaw* test techniques have been riddled with controversy, and thus no standards. The literature review of this study therefore includes more detail on these *microflaw* test techniques.

Test techniques from each category were chosen for experimental investigation on three alumina materials of varying alumina contents. The test techniques used were: *macronotches* – single edge notched bend bar (SENB), double torsion (DT), chevron notched bend bar (CVNB); and *microflaws* – indentation microfracture (IM), indentation strength in bending (ISB). Components also had to be designed and manufactured for certain tests.

The test results show the indentation induced *microflaw* techniques to be unreliable, with the data particularly sensitive to the grain size of the material. *Macronotch* test techniques are much more reliable, since they are consistent with each other in the trends between the different materials. From all the test techniques investigated in this project, the SEVNB test was shown to be the best fracture toughness test technique, in terms of suitability, precision, discrimination, and accuracy. It was also established that one of the materials provided for this study was in fact a lower quality material.

CONTENTS

ACKNOWLEDGEMENTS

I express my sincere gratitude to my parents, my brother Julian, and the rest of my family for their constant encouragement and belief in me, but mostly for their love.

I would like to thank the following people who assisted me in this project:

- My supervisor, Prof. R. B. Tait who was always willing to help me, and allowed me to ask many silly questions. Thanks for making things clearer to me.
- Glen Newins and Len Watkins for their constructive discussion on the designs of the test components as well as their expert machining of these components and the test specimens. Peter Jacobs for his machining of the test specimens. Arnold Warburton and Horst Emrich for their help in machining of the test specimens.
- Miranda Waldron of the E.M.U for her help with the scanning electron microscope.
- Mira Topic for her technical discussions and help with the equipment (hardness testers, furnaces, etc) in the Centre for Materials Engineering.
- My friends in the Department of Mechanical Engineering, Justin Williams and Ravindra Patil for their technical discussions, which helped me a lot in the designs of the test components.
- Andreas Hecht, and Multotec Wear Linings, for sponsoring the test materials for this study.
- Roy Achilles, for his belief in me and for presenting me with this opportunity. De Beers Diamond Research Laboratory for financial assistance.

I would also like to thank my friends in Cape Town – Anil, Nivan, Ravi, Vineeth, Kavindra, Kamal, Tony, Subashini, and Roshni – for their wonderful friendship and support.

Lastly, I thank my mentor in spirituality, Sagie Chetty, and my creator (Baba) for always making everything happen – hopefully I can fully grasp the plot soon!

Dedicated to my loving parents –

Jaya and Maya Naidu

NOMENCLATURE

Symbol	Meaning
K_{Ic}	Fracture toughness or critical stress intensity factor in mode I
K_c	Critical stress intensity factor
LEFM	Linear elastic fracture mechanics
ZrO_2	Zirconia
DEBID	De Beers Industrial Diamond Division
PCD	Polycrystalline diamond
PCBN	Polycrystalline cubic boron nitride
H_V	Vickers hardness
SiC	Silicon carbide
Si_3N_4	Silicon nitride
EPFM	Elastic plastic fracture mechanics
σ	Stress
c	Half crack length
ρ	Crack or notch tip radius
k_t	Stress concentration factor
E	Young's modulus
γ	Surface energy
σ_{th}	Theoretical fracture strength
σ_F	Fracture stress
U_a	Elastic strain energy
ν	Poisson's ratio
U_γ	Surface energy created by crack formation
W	Total energy for crack
F	Work done by external forces on crack
G	Strain energy release rate
R	Crack resistance
G_c	Critical strain energy release rate

P	Force or load
K_a	Applied stress intensity factor
SCG	Subcritical crack growth
V-K_I curve	Curve of crack velocity versus mode I stress intensity factor
K_{Ith}	Threshold stress intensity factor for subcritical crack growth
DT	Double torsion
DCB	Double cantilever beam
P_c	Critical load
σ_c	Strength
$Y(a/W)$	Shape factor used in determining K_{Ic}
ρ^*	Critical notch tip radius
SENB	Single edge notched bend bar or beam
CT	Compact tension
SENB-S	Single edge notched bend bar or beam – saw cut notch only
SEVNB	Single edge V notched bend bar or beam
W_m	Moment arm in DT test
μ	Shear modulus
Y^*	Geometric factor used to determine K_{Ic} in chevron notched specimens
Y_m^*	Minimum of Y^*
CVNB	Chevron notched bend bar or beam
CVSR	Chevron notched short rod
K_{Ia}	Indentation fracture toughness
CSF	Controlled surface flaw
IM	Indentation microfracture
ISB	Indentation strength in bending
Al_2O_3	Alumina
PSZ	Partially stabilized zirconia
SiO_2	Silica
CaO	Calcium oxide
MgO	Magnesium oxide
SEM	Scanning electron microscope
EDS	Energy dispersive spectroscopy

CHAPTER 1:

INTRODUCTION

1.1 Background

Ceramics have many attractive properties, such as low electrical conductivity, low thermal conductivity, low density, chemical stability, high temperature strength, corrosion resistance, high hardness, good wear resistance, and high melting points. These properties are essential for the use of ceramics as engineering components in many applications, such as insulating components, heat exchangers, cutting tools, gas turbines, etc[1, 2]. However a major drawback of ceramics, inhibiting their greater utilisation in industrial applications, is their extremely low fracture toughness, K_{Ic}, values (typically in the range $K_{Ic} = 0.5 - 5$ MPam$^{1/2}$) due to their inherent brittleness.

Here, fracture toughness may be defined as the critical stress intensity factor, K_c, in the plain strain condition, and is denoted by K_{Ic} for a crack in the opening or tensile mode. This fracture toughness may be considered a characteristic material parameter, a measure of the characteristic resistance to cracking or fracture of the material. The concept of fracture toughness is an essential factor in the application of linear elastic fracture mechanics (LEFM) to the safe design of engineering structures [1, 3].

In the practical design of engineering structures using ceramics, ceramic brittleness can lead to catastrophic failure under relatively low stress levels[1]. The fracture toughness is therefore considered one of the most important fracture properties of structural ceramic materials[4]. Fortunately, research within the last three decades have led to tremendous improvements in the mechanical properties of ceramics[1, 2, 4 - 20]. These improvements have been made through the availability of very pure and sinterable fine ceramic powders, as well as by incorporating novel toughening mechanisms, such as the stress induced martensitic phase transformation in zirconia (ZrO_2), microcracking toughening, fibre/whisker reinforcement, and others[1, 2, 4 - 20].

Although fracture toughness testing techniques have long been standardised for metallic materials[21 - 24], standards for measuring K_{Ic} of ceramics have only begun to emerge relatively recently[25 - 27]. This may possibly be due to the methods adapted from the techniques already in practice for the metallic materials having led to controversial results in the case of structural ceramics[28]. The fundamental difference in the fracture behaviour of ceramics (primarily controlled by cracks), and metals (primarily controlled by dislocations, which relieve stress concentrations, even though cracks may be present in the material) may be responsible for the difficulty of adapting the techniques to ceramic materials[29]. Difficulties in generating sharp precracks (which is a prerequisite in K_{Ic} testing and is discussed further in Chapter 3) in ceramics, again due to their inherent brittleness, have probably also contributed to the controversial results, and consequently the lack of standard testing techniques.

There are, however, a wide variety of methods to determine K_{Ic} of ceramic materials described in the literature. Fracture toughness testing techniques can broadly be divided into two categories: (a) testing with *macrocracks*, which are usually saw-cut, and (b) testing involving indentation induced *microcracks*. These are discussed in detail in Chapter 3. In addition to the K_{Ic} values differing between the test techniques of these two broad categories, it is now also well known that different techniques, within each category, can produce different K_{Ic} values for the same material[28, 30 - 33]. The literature gives ample evidence that the determined value of K_{Ic} is sensitive to the method of measurement, as well as to the experimental parameters of a given method[28].

Some of this difference in results may be due to various complicated microfracture processes in modern brittle materials, which in turn may be a consequence of the improvements achieved in the mechanical properties of ceramics[1]. Other contributions to the differences could be the inherent micro-flaw distribution in the material, and difficulties with machining and preparing specimens, which are both characteristic of ceramics. The different techniques could also be resulting in variable strain energies in the specimens. All these contributions to the different values in K_{Ic} are sometimes a direct consequence of the fabrication techniques used, with statistical methods such as Weibull analysis being frequently needed to determine the effects of fabrication techniques on toughness. This awareness of a need for reliable toughness

measurements of brittle materials forms the basis of this thesis. This dissertation entails a comparative investigation into the fracture toughness testing techniques, as applied to particularly brittle materials, as characterised by an alumina ceramic.

1.2 Motivation for project

De Beers Industrial Diamond Division (DEBID) products, such as polycrystalline diamond (PCD) and polycrystalline cubic boron nitride (PCBN) are ultrahard ceramic composite materials used as cutting tools. Although they have a better combination of hardness and fracture toughness (Vickers hardness, H_V = 28 – 50 GPa; K_{Ic} = 3 – 8 MPa.m$^{1/2}$) than conventional cutting tool ceramics, such as silicon carbide, SiC, and silicon nitride, Si_3N_4, (H_V = 3 – 30 GPa; K_{Ic} = 2 – 9 MPa.m$^{1/2}$), they are still susceptible to premature catastrophic failure, and improvements in K_{Ic} are always desirable. Different techniques have been used to determine K_{Ic} of these ultrahard products with the now well-known result of differing values for K_{Ic} [28, 30-34]. There is therefore a need for a clear understanding of the different test techniques and the fracture mechanics fundamental principles involved. It is believed that this understanding may contribute to giving an insight into the most suitable fracture toughness testing techniques, not only for alumina, but also for DEBID ultrahard cutting tool materials.

The purpose of this project, therefore, was to develop competence in fracture mechanics for application to brittle materials.

1.3 Objectives

The prime objective was to investigate the fracture toughness testing techniques used on brittle materials, and thus determine the best fracture toughness test technique/s for engineering ceramics in terms of suitability, accuracy, precision and discrimination. It was hoped that the usefulness or applicability as well as the shortcomings of each test technique could also be established through this project.

1.4 Scope and Constraints

The scope of this thesis covered an aspect of the application of fracture mechanics to brittle materials, i.e. the field of linear elastic fracture mechanics (LEFM). The investigation was selectively confined to alumina, as being representative, yet still economic material for the study. Although toughening mechanisms in brittle materials do exist and pose challenges to K_{Ic} testing, the influence of these mechanisms lies outside the scope of the investigation, since toughened materials, through zirconia, for example, could not readily be obtained for testing. Other constraints experienced during this project are listed below:

- Due to brittleness, machining of the ceramics was extremely difficult and time consuming, with the result of different specimen sizes and fewer tests being performed in certain cases; and
- Lack of definitive and established K_{Ic} testing standards for brittle materials.

1.5 Plan of Development

The report begins with a literature review of the fundamental principles of LEFM followed by a review of the relevant existing fracture toughness testing techniques. These two reviews were purposely set in different chapters so as to introduce the fundamental concepts necessary for fracture toughness testing, before actually discussing the test techniques. Due to controversies surrounding the microflaw techniques for determining toughness, much more detail has been placed on these techniques in the review. Selected techniques were then chosen for more detailed experimental investigation in the project. All the experimental techniques used in the project are then presented together with the test program, after which the results of these are given together with the analysis and discussion. Lastly conclusions are drawn and recommendations made for possible future work.

CHAPTER 2:

LITERATURE REVIEW –

FRACTURE MECHANICS PRINCIPLES

The presence of flaws in practical and industrial polycrystalline materials result in the strength being much less than that of a corresponding perfect crystal. Therefore, understanding the strength and fracture behaviour of a polycrystalline material involves knowledge of the behaviour of microcracks under applied stress. Due to the fracture dominant behaviour (i.e. fracture before general yielding) of brittle materials, LEFM has been used to study the fracture behaviour of brittle materials. Elastic plastic fracture mechanics (EPFM) is used for the study of more ductile materials such as metals that exhibit greater ductility and generally have very large crack tip plastic zones[1, 3, 29].

2.1 Stress Concentrations

Inglis performed a stress analysis of an elliptical hole in a uniformly stressed plate in 1913 [35]. This analysis showed that the local stresses about a sharp notch or corner could be several times higher than the applied stress. Furthermore it became apparent that even sub-microscopic flaws could be potential sources of weakness in solids. Figure 2.1 shows a plate with an elliptical hole subjected to uniform applied tension, and when the ellipse collapses down to be an infinitesimally narrow ellipse, it may be considered to represent a crack.

From Inglis's stress analysis, the greatest stress concentration for the plate in figure 2.1 occurs at point C, and was derived as[35]:

$$\sigma_{yy}(c,0) = \sigma_L\left[1+2\left(\frac{c}{\rho}\right)^{1/2}\right] \qquad \textbf{(2.1)}$$

where ρ is the radius of curvature a C, and c is half the crack length.

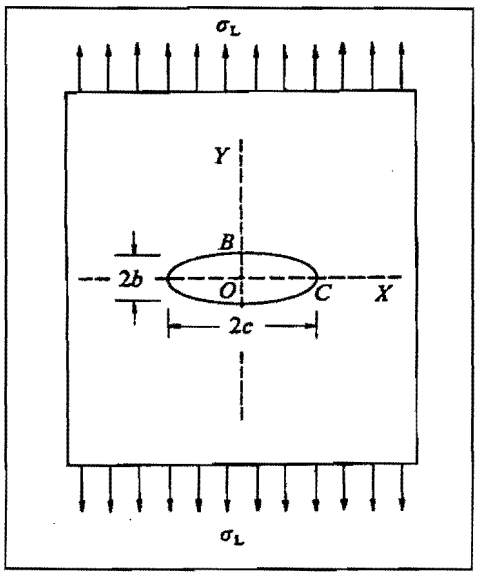

Figure 2.1: *An elliptical hole (with major and minor axes Y and X respectively) subjected to a uniform applied tensile stress* σ_L *[after ref. 35].*

For $b << c$, as would be the case for a very sharp crack, equation 2.1 is reduced to[35, 36]:

$$\frac{\sigma_{yy}(c,0)}{\sigma_L} = 2\left(\frac{c}{\rho}\right)^{1/2} = k_t \qquad \textbf{(2.2)}$$

The ratio of stresses on the left hand side of the equation is referred to as the stress concentration factor k_t. From this equation it is evident that for long thin cracks the stress concentration can be greater than the strength of the material, and thus result in failure even though the applied stress is well below the intrinsic material strength.

2.2 Griffith theory

2.2.1 Griffith fracture strength

Griffith reported in 1920 that the theoretical fracture strength σ_{th} of a solid could be characterised by the following equation[3, 37, 38]:

$$\sigma_{th} = \left(\frac{E\gamma}{b_0}\right)^{1/2} \tag{2.3}$$

where E is the elastic modulus, γ is the surface energy and b_0 is the equilibrium interatomic spacing. This theoretical strength is therefore of the order of $E/10$, but strengths in practice have been found to be at least two orders of magnitude lower than this theoretical strength σ_{th}[37, 38]. Griffith supposed that this discrepancy between theoretical and actual strengths was due to the presence of defects in the material[37, 38].

He then proceeded to evaluate, both experimentally and theoretically, the fracture stress of a brittle material (such as glass) containing a defect using Inglis's stress analysis (Section 2.1). Setting σ_{yy} and ρ from equation 2.2 as the maximum stress σ_{max} and the lattice spacing b_0 respectively and equating with Griffith's theoretical strength yields[37, 38]

$$2\sigma_L\sqrt{\frac{c}{b_0}} = \sqrt{\frac{E\gamma}{b_0}} \tag{2.4}$$

At fracture $\sigma_L = \sigma_F$, hence

$$\sigma_F = \sqrt{\frac{E\gamma}{4c}} \tag{2.5}$$

For many materials γ is of the order of $0.01\ Eb_0$[37]. Substituting this for γ into equation 2.5, it can be seen that a defect length $2c$ of $5000b_0$, say approximately 1 μm, is sufficient to lower the fracture strength by two orders of magnitude. It must be remembered that the Inglis solution for stresses around an elliptical hole was derived strictly on the basis of linear elasticity, yet a crack tip stress which is outside the realm of linear elasticity is predicted from equation 2.5. Linear elasticity was used to derive the left hand side of equation 2.5, while a sinusoidal stress-strain curve was used for the right hand side. The left hand side relates to the macroscopic applied stress and the right hand side to the atomic force-displacement relations[37].

2.2.2 Griffith Energy Balance Approach

Griffith derived a thermodynamic criterion for fracture by considering the total energy balance of a cracked body as the crack length increased. He postulated that the change in the potential energy of the fracture test system during an increment of crack surface must balance the requirement of the surface energy increment[1, 3, 37, 38]. The crack extends spontaneously under the applied stress only if the total energy decreases. The advantage of the energy approach is that, by considering energy changes in the body as a whole, attention is removed from the very highly strained region immediately surrounding the crack tip, with a useful expression for fracture stress still being derived[37].

The stored strain energy per unit volume U_a for a stressed brittle material is given by[39]:

$$U_a = \frac{\sigma^2}{2E'} \tag{2.6}$$

where σ is the applied stress and E' is the Young's modulus E in plane stress, (or $E'=E/(1-\nu^2)$ in plane strain), with ν the Poisson's ratio of the material. For an infinite plate of such material with unit thickness and surface energy per unit area γ, stored strain energy would be released immediately above and below the crack region since the crack surface cannot sustain a stress normal to its surface[3, 39] (figures 2.2 and 2.3).

The strain energy is merely the energy per unit volume multiplied by the volume per unit thickness or surface area. Griffith showed that this relaxed area was equal to $2\pi a^2$ for a crack of length $2a$ [39]. Hence

$$U_a = \left(-\frac{\sigma^2}{2E'}\right)\left(2\pi a^2\right) = -\frac{\sigma^2 \pi a}{E'} \tag{2.7}$$

The released strain energy is used up in the creation of new surfaces due to the crack. A crack of length $2a$ and unit thickness gives a surface energy U_γ according to

$$U_\gamma = 4a\gamma \tag{2.8}$$

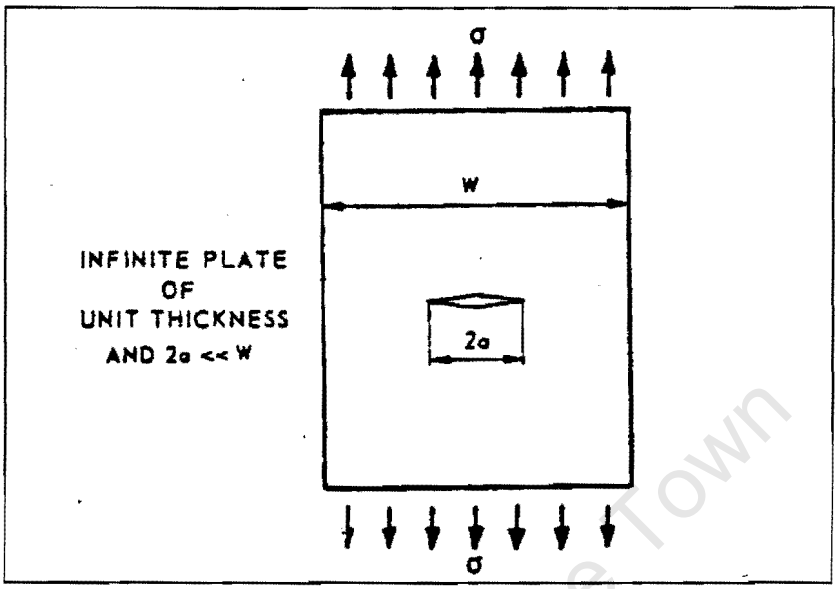

Figure 2.2: *A through cracked plate of unit thickness with crack length 2a and subjected to applied stress σ [after ref. 3].*

The total energy W for the crack with the work done by external forces F is therefore

$$W = U_a + U_\gamma - F = -\frac{\sigma^2 \pi a^2}{E'} + 4a\gamma - F \tag{2.9}$$

This energy balance is represented on a schematic energy versus crack length plot in figure 2.3[39]. Crack growth instability will occur as soon as W no longer increases with increasing crack length a, i.e. if

$$\frac{dW}{da} \le 0 \Rightarrow \frac{d}{da}\left(U_a + U_\gamma - F\right) \le 0 \tag{2.10}$$

which can be rearranged to give

$$\frac{d}{da}(F - U_a) \ge \frac{dU_\gamma}{da} \tag{2.11}$$

The term $\frac{d}{da}(F - U_a)$ is known as the strain energy release rate G and $\frac{dU_\gamma}{da}$ the crack resistance R [ref. 3]. The fracture condition in equation 2.11 can thus be rewritten as

$$G \geq R \tag{2.12}$$

It has been shown that the magnitude of G is equal to $\frac{dU_a}{da}$ for both the fixed grip condition (release of elastic strain energy) and the constant load condition (increase of elastic strain energy)[3].

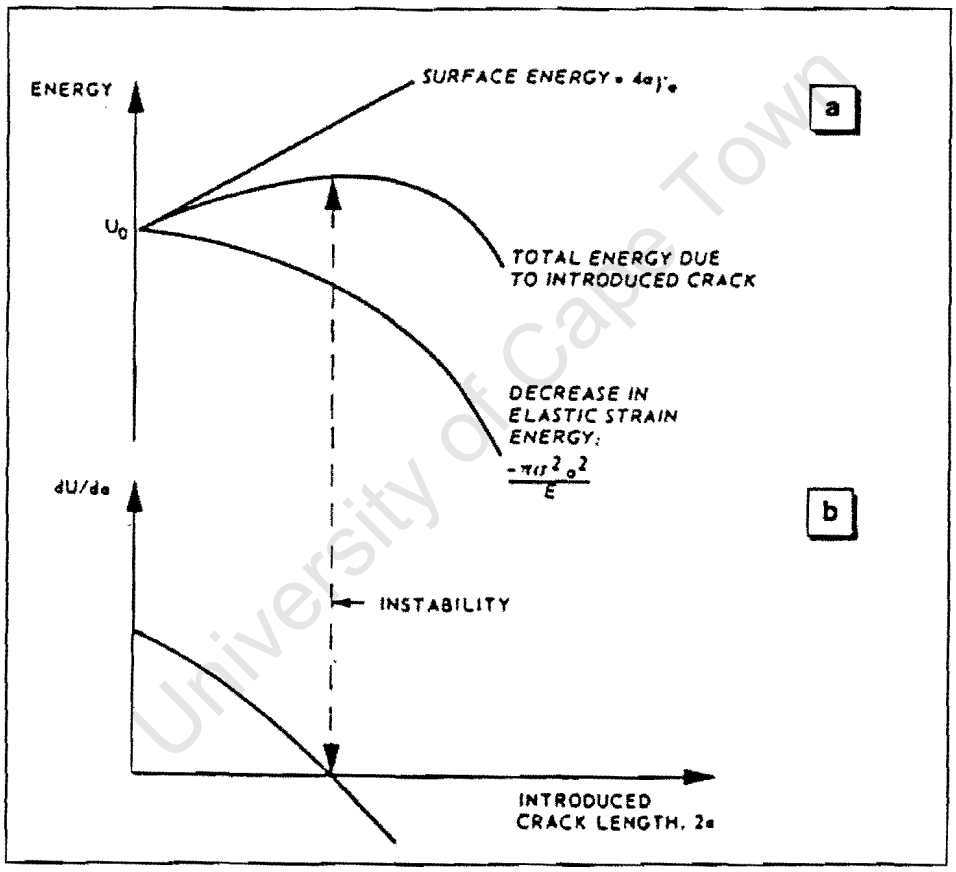

Figure 2.3: *Energy balance as crack extends in brittle material – (a) energy W, (b) energy derivative dW/da [after ref. 3].*

At the point of unstable fracture

$$\frac{dW}{da} = \frac{d}{da}(F - U_a) + \frac{dU_\gamma}{da} = -\frac{2\sigma^2 \pi a}{E'} + 4\gamma = 0 \tag{2.13}$$

This reduces to

$$\sigma_f = \sqrt{\frac{2E'\gamma}{\pi a_c}} \text{ or } \sigma_f \sqrt{\pi a_c} = \sqrt{2\gamma E'} = \text{a constant} \quad \textbf{(2.14)}$$

where a_c is the critical crack length at the fracture stress σ_f. This relationship of $\sigma_f \sqrt{\pi a_c}$ being a constant agreed with Griffith's experimental investigations for glass.

If R is a constant, then G must exceed a critical value G_c for unstable crack growth to occur. Thus fracture occurs when

$$G = \frac{dU_a}{da} = \frac{\pi\sigma^2 a}{E'} \geq R = \frac{\pi\sigma_c^2 a}{E'} = G_c \quad \textbf{(2.15)}$$

2.3 Modes of failure

All stress systems in the vicinity of a crack tip may be derived from one or more of the three modes of loading, as shown in figure 2.4. Mode I is the predominant stress situation in many practical cases. Most materials have a higher shear (mode II) and torsional (mode III) fracture toughness than in tension (mode I), and thus mode I cracking is the most commonly investigated mode of fracture[3, 40]. Only mode I fracture toughness testing is covered in this report.

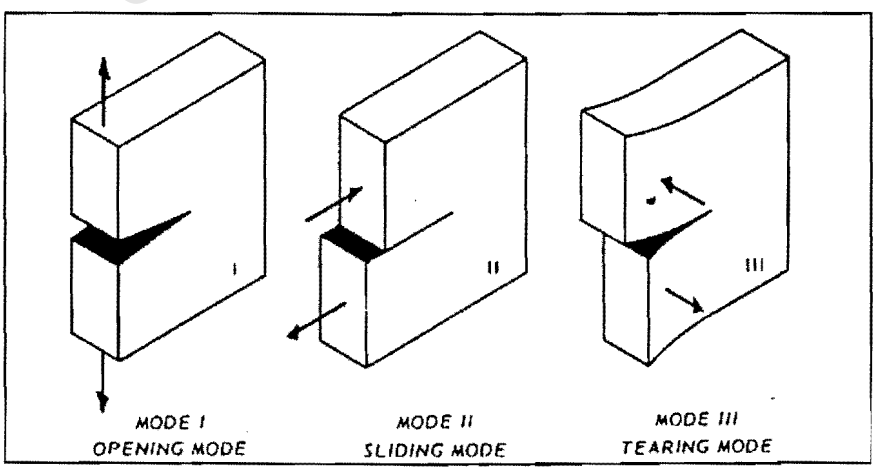

Figure 2.4: *The three modes of loading – (a)* I *opening / tension; (b)* II *sliding / in plane shear; and (c)* III *tearing / anti-plane shear [after ref. 3].*

2.4 Irwin's Stress Intensity Approach

The stress intensity approach was developed by Irwin in the 1950's. The magnitude of the elastic stress field is given by the stress intensity factor K, which in its general form is given by the following equation[3]:

$$K = \sigma\sqrt{\pi a} \cdot f\left(\frac{a}{W}\right) \tag{2.16}$$

where $f\left(\frac{a}{W}\right)$ is a dimensionless parameter depending on the specimen and crack geometries.

Irwin then demonstrated that for a crack extending by an amount da, the work done by the stress field ahead of the crack when moving through the displacements corresponding to a crack length (a+da) is equal to the change in strain energy Gda. The achievement of a critical stress intensity factor K_c is therefore exactly equivalent to the Griffith energy balance approach, where a stored strain energy G_c is attained[3].

The critical stress intensity factor, K_c, may therefore be used as the parameter governing fracture instead of the critical energy value G_c. For tensile loading the relationships between K_c and G_c are given by

$$G_c = \frac{K_c^2}{E} \qquad \text{plane stress; and}$$

$$G_c = \frac{K_c^2}{E}(1-\nu^2) \qquad \text{plane strain} \tag{2.17}$$

For plain strain it is customary to write G_{Ic} and K_{Ic}, where the subscript I indicates mode I tensile loading. The subscript is also used for expressions including the stress intensity factor as a variable, i.e. K_I [ref. 3]. K_c of metals in plane stress is always higher than that in plane strain due to the less constrained deformation for the plane stress state. The triaxial stress state dominated fracture in the plane strain condition reduces the ductility and leads to crack extension at a lower K_c value[1].

The Griffith-Irwin solution for a through cracked plate can now be written as

$$\sigma\sqrt{\pi a} = \sqrt{2E\gamma} = \sqrt{EG} = K \tag{2.18}$$

and the failure criterion thus becomes

$$K = \sigma\sqrt{\pi a} \geq \sigma_c\sqrt{\pi a} = K_c \tag{2.19}$$

The use of a critical stress intensity indicates that crack extension occurs when the product $\sigma\sqrt{a}$ attains a constant critical value. Using the stress intensity factor as the characterising parameter for crack extension is a fundamental principle of LEFM[3].

2.5 Elements of LEFM

LEFM provides a quantitative description for failure phenomena due to fracture and also the capability of the prediction of engineering structure lifetimes. There are several important hypotheses within LEFM that require consideration before application in practice[1]:

1. The origin of failure is always assumed to be a sharp crack or flaw with zero curvature of the tip radius, embedded within a continuum elastic body.
2. Relative to the geometrical dimensions of the elastic body, only a small-scale process zone is assumed at the crack tip. This implies a linear far-field relation between the load (stress) and the displacement (strain).
3. A single parameter, the stress intensity factor K, is used to describe the stress-strain field in the vicinity of the crack tip. K varies linearly with both the applied external force and the boundary displacement.
4. Fracture occurs under the linear condition of small scale processing.
5. Crack extension initiates when the stress intensity factor reaches a certain critical value K_c, which is achieved through increasing either the applied load or displacement.

In a cracked body, the strength σ_c or critical load P_c for failure is controlled by the presence of the crack due to the stress concentrating effect of the crack. For an equilibrium crack at a critical load P_c [1]:

$$P_c = P_c(a, D, K_c) \tag{2.20}$$

where D is a measure of the characteristic dimensions of the brittle material, and K_c is the critical value of the stress intensity factor K. Due to the linear relation of K to P, equation 2.20 can be rewritten as

$$P_c = K_c f_p(a, D) \tag{2.21}$$

or in terms of the strength σ_c as

$$\sigma_c = K_c f_\sigma(a, D) \tag{2.22}$$

where $f_p(a,D)$ and $f_\sigma(a,D)$ are shape factors that account for the effect of the crack and specimen geometries on the stress intensity of the cracked body[1].

K_c is dependent on the deformation conditions such as plane stress or plane strain, as discussed in Section 2.4, and in general is not a material characteristic. The critical stress intensity factor for the plain strain condition, however, is a material characteristic, since in plane strain the triaxiality at a crack tip does not change appreciably with variation of thickness. This critical stress intensity factor is known as the fracture toughness and is denoted by K_{Ic} for a crack in the opening mode. It represents the lower limit of the critical K_c value[1].

When using the K_I stress intensity parameter, attention must be confined to a sufficiently small region, the K-dominant region in the vicinity of the crack tip to ensure the validity of the LEFM approximation (figure 2.5). The frontal process zone must be small enough compared with the characteristic size of the K-dominant region, and is thus called the *small-scale process zone*. The crack length and geometrical

dimensions of the elastic body must be large in comparison to the *K*-dominant region[1].

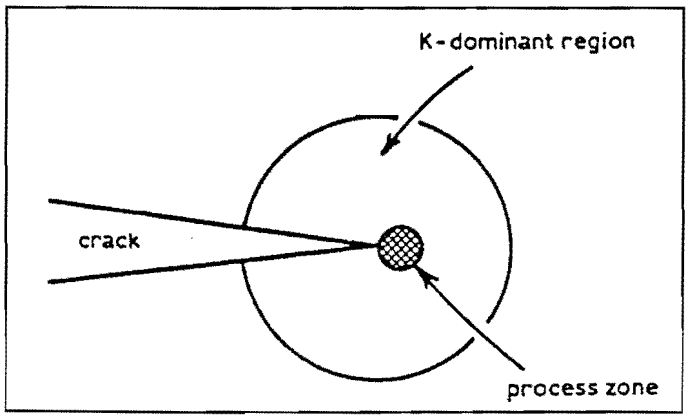

Figure 2.5: *Crack tip configuration and basis of LEFM [after ref. 1].*

2.6 R-curve behaviour

The crack resistance, R, per unit thickness was defined as $R = \frac{d}{da}(U_\gamma)$, where U_γ represents the elastic surface energy of the crack surfaces. This is the energy needed to propagate the crack (Section 2.2.2)[3].

Using Griffith's energy balance approach, it has been shown that crack growth instability occurs if $G \geq R$, where G is the elastic energy release rate, which is also termed the crack driving force. To guarantee that an excess of driving force persists as the crack extends, the additional condition

$$\frac{dG}{dc} \geq \frac{dR}{dc} \qquad \textbf{(2.23)}$$

is required[2, 3, 41].

Figure 2.6 shows G and R plotted as a function of crack length for the case of a constant crack resistance.

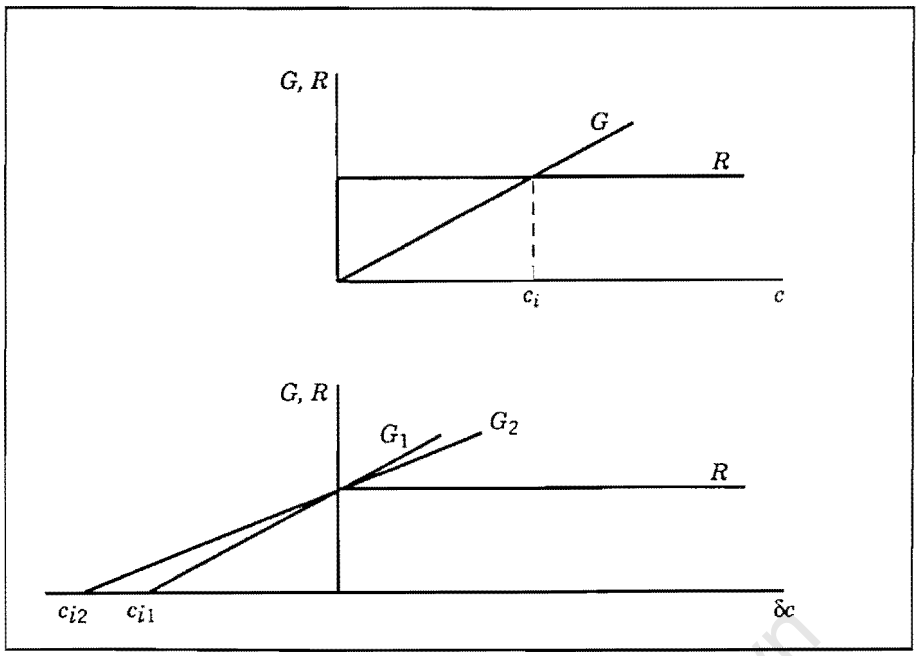

Figure 2.6: *Representation of energy balance with constant resistance [after ref. 41].*

For the upper portion of figure 2.6, $G = R$ at the initial crack length c_i and since the other condition, $\frac{dG}{dc} > \frac{dR}{dc}$ is also satisfied, the slightest increase in crack length or stress will result in crack instability and propagation. The lower portion of figure 2.6 is merely the upper portion redrawn with the origin taken at the initial crack tip. G curves for two different initial crack lengths, c_{i1} and c_{i2} are shown in this lower portion. Different values of stress have been taken so that either crack is just in balance and would propagate catastrophically for any slight disturbance[41].

Figure 2.7 illustrates the behaviour for the case in which resistance increases as a crack grows from its initial length. This is a common and very important case in polycrystalline ceramics and ceramic composites. R-curve behaviour can arise from several types of crack shielding and crack bridging toughening mechanisms[5 - 19]. Extensive discussion on R-curve behaviour is considered beyond the scope of this thesis, but can be found in the literature[1, 2, 5 – 19, 30, 33, 35, 41 - 43].

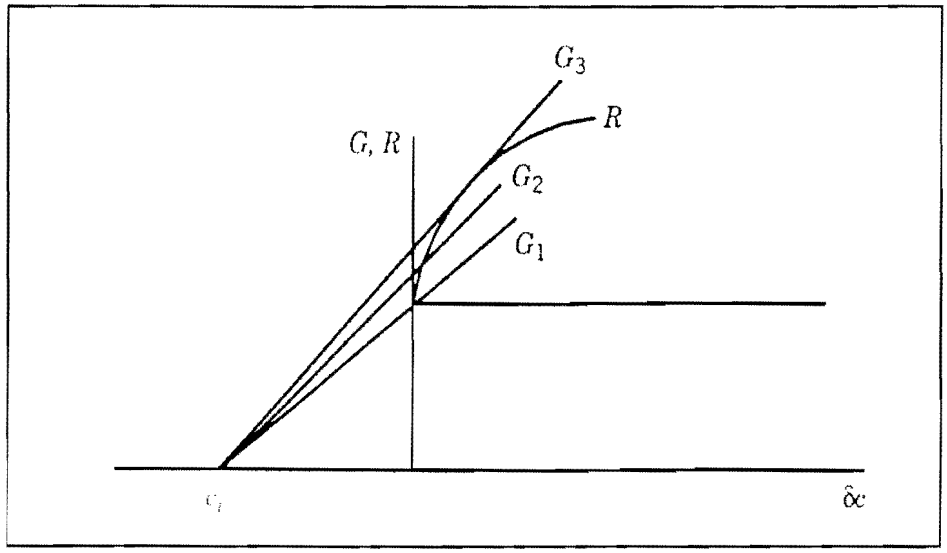

Figure 2.7: *Representations of energy balance with increasing resistance [after ref. 41].*

For the rising R-curve of figure 2.7, the G_1 curve is drawn for a stress such that $G_1(c_i) = R(c_i)$. However $\frac{dG_1}{dc} < \frac{dG_2}{dc}$, therefore the crack will not extend. For a higher value of stress the curve G_2 exceeds the initial crack resistance, so that the crack will extend an amount δc such that $G_2(c_i + \delta c) = R(c_i + \delta c)$. Since $dG_2/dc < dR/dc$ at crack extension δc, the crack will not extend further. Therefore a rising R-curve can lead to a region of *stable crack propagation* under stress. Further increase in stress results in the G_3 curve, which is tangent to the R-curve. The crack extends from its initial length as before, but will continue to propagate catastrophically since $dG_3/dc = dR/dc$ at the point of tangency. Therefore a region of stable crack propagation exists for stresses between the G_1 and G_3 curves[41].

The R-curve behaviour can also be described in terms of the applied stress intensity factor by converting to stress intensities via the relation $K = \sqrt{EG}$ [ref. 3]. When this behaviour is discussed in terms of stress intensity factor, the term T-curve (i.e. toughness curve) is used. The conditions for fracture are analogous to those involving G and R, i.e.

$$K \geq T \text{ and } \frac{dK_a}{dc} \geq \frac{dT}{dc} \qquad \textbf{(2.24)}$$

where $T = K_{Ic}$, and K_a is the applied stress intensity factor. Figure 2.8 shows an example of a T-curve with K lines, and is analogous to figure 2.7, which is plotted in terms of G and R[41].

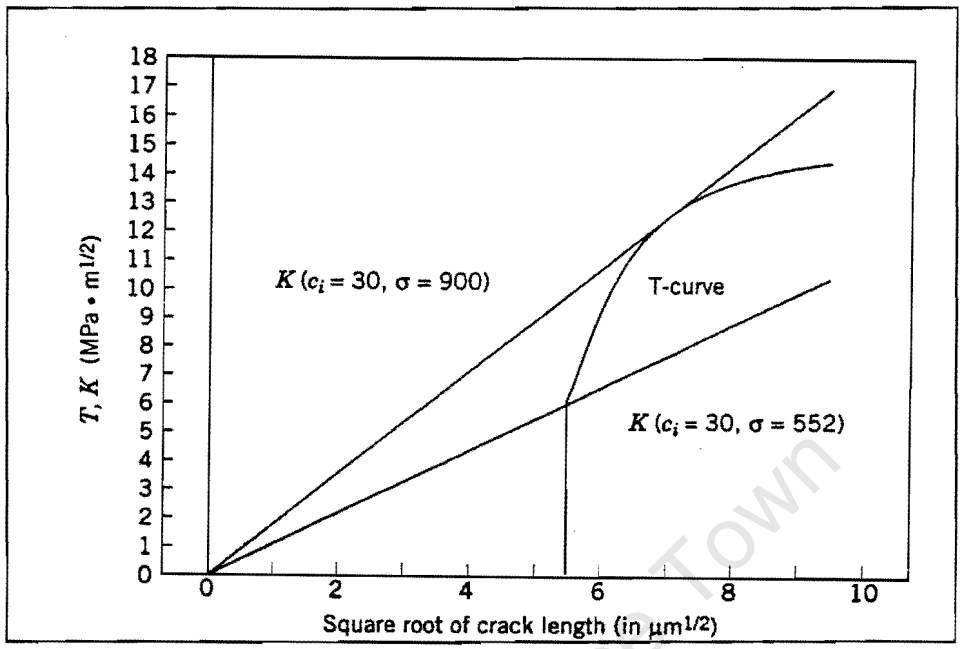

Figure 2.8: *T-curve in K linear format with square-root crack length scale [after ref. 41]*

R-curves are usually determined from specimens containing macrocracks[2]. The development of natural flaws during loading has also been investigated for some cases such as alumina and a magnesia-partially stabilised zirconia (figure 2.9). Munz and Fett have reported that the R-curves for the small surface cracks were below the R-curves for macrocracks in both these cases[2].

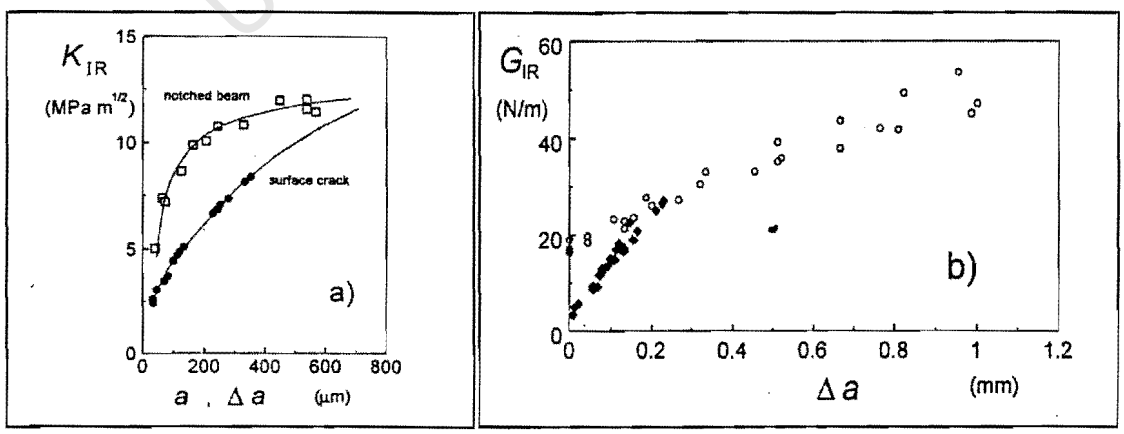

Figure 2.9: *R-curves for macro- and microcracks – (a) MgO-doped zirconia; (b) alumina. Open symbols – macrocracks, closed symbols – microcracks [after ref. 2].*

2.7 Subcritical crack growth

Two types of crack extension have thus far been considered, viz. unstable crack extension when $K_I = K_{Iinst}$ (or at $K_I = K_{Ic}$ for a material with a flat R-curve) and stable crack growth when $K_I = K_{I0}$ (K_{I0} is initial value of T on the T-curve) as demonstrated in Section 2.6. A third type of crack extension called *subcritical crack growth* (SCG) will now be discussed[2].

A crack of initial depth a_i propagates slowly to a critical load-dependent size a_c, at which unstable crack extension occurs. The crack growth is governed only by the stress intensity factor K. A unique relation exists between the crack growth rate V and K_I for a given material and environment[2]:

$$V = \frac{da}{dt} = f(K_I) \tag{2.25}$$

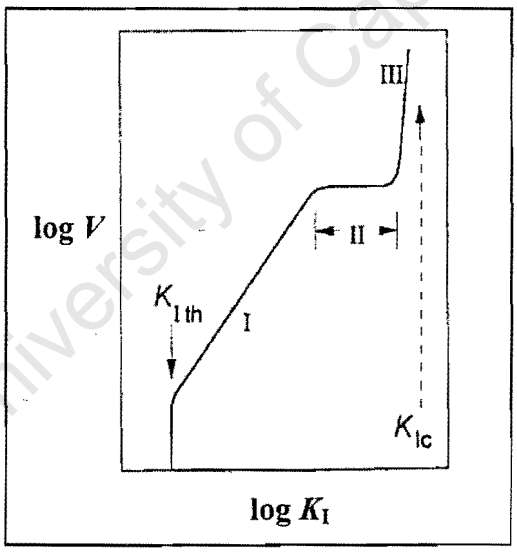

Figure 2.10: *Typical V-K_I curve with logs plotted on both axes [after ref. 2].*

A log-log plot of a V-K_I curve is shown in figure 2.10. At low crack growth rates an extended linear region is observed – region I. In this region the crack growth rates follow a power-law relation[2]:

$$V = AK_I^n = A^*\left(\frac{K_I}{K_{Ic}}\right)^n \tag{2.26}$$

with parameters A, A^* and n dependent on the material, temperature and environment, with $n > 15$ for most ceramics[2].

In certain cases (such as glass) a threshold value K_{Ith} can be detected, below which no subcritical crack growth is found. A plateau (region II) in V may occur at relatively high crack growth rates, with the growth rates independent of K_I. Further increasing K_I results in high crack growth rates (region III), followed by unstable crack extension with the crack growth rates in the order of the sound velocity [2]. Lifetime predictions **can** be calculated based on the lower crack growth rates of region I, but are largely impractical because of complications introduced by the high exponent values, since crack growth rates of $V \cong 10^{-12}$ m/s are relevant in predicting natural crack lifetimes of about a year[2].

Various methods have been used to determine V-K curves. V-K curves for macrocracks in the order of several millimetres can be obtained through the following tests: double torsion (DT), double cantilever beam (DCB), and bending (controlled fracture or constant load) tests with notched specimens. The crack growth properties of natural cracks in the order of ~50 μm can be measured using the dynamic bending strength test, and lifetime measurements in static tests. Differences in crack growth results between micro- and macrocracks have been observed[2]. The double torsion technique (DT) is discussed further in Section 3.2.2.

2.8 Summary of Chapter 2

This chapter reviewed the fundamental principles of LEFM, as applied to brittle materials or materials that display behaviour within the linear elastic load regime. Stress concentrations were introduced and showed the deleterious effect a flaw can have on the strength of a material. Brief reviews of fracture theory, contributed mainly by early researchers such as Griffith and Irwin were presented, together with the all-important assumptions made in LEFM. Lastly, fracture behaviours (such as R-curve behaviour and subcritical crack growth) observed to be relevant to ceramic materials were discussed.

The concepts and theory presented in this chapter are necessary in understanding the fracture behaviour of ceramic materials in practice. Fracture toughness testing techniques, which are ultimately derived from the fundamentals presented in this chapter, are reviewed next in Chapter 3.

CHAPTER 3:

LITERATURE REVIEW –

FRACTURE TOUGHNESS TESTING TECHNIQUES

3.1 Introduction

Fracture parameter measurements are based on the equations 2.21 or 2.22 from Section 2.5[1]. Determining the fracture toughness in an actual fracture test therefore requires either the critical load P_c, or strength σ_c, and a shape factor $Y(a/W)$, under plane strain conditions for a known specimen geometry[1, 2, 29]. In addition to the plane strain condition, elastic brittle behaviour or 'fast fracture' is a test pre-requisite in many ceramics and glasses, which exhibit slow crack propagation (subcritical crack extension – Section 2.7) by stress corrosion cracking at stress intensity values lower than K_{Ic}[1].

3.1.1 Measuring fracture toughness

The measurement of fracture toughness or other fracture mechanics parameters basically consists of the following three steps: generating a crack; recording the failure load; and calculating the toughness based on the observations[1, 2, 29]. These are discussed in turn.

i. Generating a crack in the test specimen

Pre-existing randomly oriented cracks of different sizes in brittle materials make it virtually impossible to determine which one will initiate catastrophic failure. Artificially introducing a crack or notch, which is much greater than the size of the critical inherent crack in the material is therefore necessary, so as to ensure that when

failure occurs, it is due to propagation of the specific artificially introduced crack [29]. Precracking is then undertaken to ensure that the crack introduced is a sharp one to satisfy the conditions of LEFM, and thus obtain an accurate K_{Ic} value – this is discussed further in Section 3.1.2, part ii[1, 2, 29].

ii. Measurement of the failure load

For materials that exhibit perfectly elastic brittle behaviour until failure, the load – displacement (P-u) relation is linear till fracture, and the critical load for crack extension P_c coincides with the peak load, P_{max}. However, many refractories, ceramic composites, coarse-grained polycrystalline ceramics, and phase transformation toughened ceramics exhibit a distinct and often substantial discrepancy between the P_c value and P_{max}, which is related to their rising R-curve behaviour[1]. Crack initiation always occurs somewhat below the peak load and extends in a stable fashion in relation to the peak load. The linear elastic load-displacement relation is altered as a result of this stable crack growth. Therefore, in such cases P_{max} cannot be used to determine the true fracture toughness. The required precise critical load, P_c, is then determined via clip gauge displacement measurements (as in ASTM E399[21, 23]) and / or by direct observation of the onset point of crack tip extension by visual methods [1].

iii. Calculating the fracture toughness K_{Ic}

K_{Ic} is calculated from the failure load P_c or the failure stress σ_c, and crack depth a using the equations 3.1 and 3.2, which are derived from equations 2.21 and 2.22 from Section 2.5:

$$K_{Ic} = (P_c/BW^{1/2})Y(a/w) \quad \textbf{(3.1)}$$

$$K_{Ic} = \sigma_c (\pi a)^{1/2} F(a/w) \quad \textbf{(3.2)}$$

where B is the specimen thickness, W is the specimen width, and $Y(a/W)$ and $F(a/W)$ are appropriate shape factors.

3.1.2 Specimen geometry and test methods used to determine K_{Ic}

A number of different procedures have been developed to determine the fracture toughness K_{Ic} of brittle materials, resulting in a wide range of specimen geometries. The type of measurement required, research objectives, fracture behaviour and material microstructure all govern the selection of the most convenient specimen geometry and test method. Selecting the appropriate specimen geometry and test method requires the following factors to be taken into consideration[1]:

i. Specimen size constraints

Due to the very limited plasticity of most ceramics, specimens as thin as 2 mm may be sufficient for the usual engineering ceramics. The only real constraint on specimen thickness is therefore that of microstructural representation. The structure of polycrystalline ceramics must be statistically representative over the specimen section, with the characteristic dimensions (such as thickness and width) being much larger than the grain or crystal size (~50 times)[1].

ii. Notch and crack geometries

In principle, any notch or crack geometry can be used for fracture toughness measurements, provided that the shape factor expressed as either $Y(a/W)$ or $F(a/W)$ is known. There are, however, two specific types of crack geometry prevalent in brittle materials testing, i.e. *macrocracks* (or *macronotches* – Section 3.2) and indentation induced *microcracks* (or *microflaws* – Section 3.3). *Macrocracks* include straight through cracks and chevron V notches, while the *microcracks* comprise both the Vickers and Knoop indentation induced surface flaws[1].

Numerical or analytical determinations of the shape factors $Y(a/W)$ and $F(a/W)$ for numerous macronotch geometries are simple and straightforward, and can be found in published stress intensity handbooks[1, 22]. Indentation induced cracks are almost always associated with undesirable residual stresses around the impression caused by the indentation plastic deformation[1, 2]. This leads to ambiguity and complexity of the

stress intensity calculations, resulting in indentation methods being qualitative and semi-empirical[1].

When discussing the fracture behaviour of strength controlling intrinsic flaws in brittle ceramics, the information obtained from indentation induced microflaws will be more straightforward and possibly more significant than similar results obtained for macronotched specimens. This is due to indentation induced microcracks being similar in size to the flaws controlling the strength of many ceramics[1]. Differences in toughness values obtained from macro- and micro-cracks have been reported in numerous ceramic systems[1, 2, 29]. This is due to the substantial difference in microstructural interactions at a macrocrack tip and a microflaw tip[1].

i. Notch tip acuity

Thin copper wheels coated with diamond powder have mainly been used for notch preparation. This technique can produce notches of about 50 – 60 μm width[2].

The final notch tip radius, ρ, is thus approximately half the width of the notch slit or saw blade thickness. LEFM, however, makes the assumption that $\rho = 0$ to simulate an ideal planar crack, but unfortunately diamond sawed notches do not perfectly fulfill this requirement. Apparent fracture toughness values, which are calculated from the maximum load, decrease with decreasing notch tip radii[1, 2, 30]. Below some critical notch tip radius, ρ^*, the derived fracture toughness values become constant, or rather approaches the true K_{Ic} value. This is demonstrated in figure 3.1.

The critical value ρ^* is strongly dependent on the microstructure of the tested material. For example, some refractory materials have ρ^* values as large as 1 mm, while ρ^* appears to be less than 10 μm in some fine-grained ceramics. A very narrow notch is necessary for fine-grained ceramics. In all cases it must be ensured that the saw cut is narrow enough[1, 2].

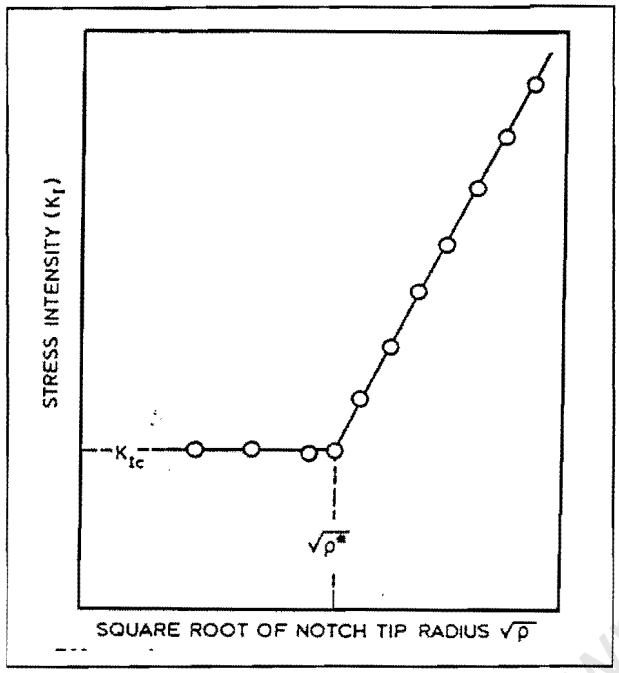

Figure 3.1: *Effect of notch tip radius on apparent fracture toughness [after ref. 1].*

Nishida *et al.* proposed a procedure to introduce notches with notch tip radii in the range 1 – 10 μm[ref. 2]. This procedure involved first introducing a conventional saw cut, and then producing a sharp V-shaped notch by using a razor blade with diamond paste[2].

Generating an ideal sharp crack is much more difficult. Natural cracks such as fatigue cracks are considered to be the sharpest cracks that can be produced in the laboratory, leading to cyclic fatigue cracking ahead of a sawed or machined notch being conventionally applied to metals and metallic alloys. This cyclic fatigue technique is however inconvenient for ceramics due to the limited plasticity at the notch tip of brittle materials[2].

Static slow crack growth in environments where stress corrosion can occur, has been observed in many oxide ceramics and non-oxide materials. This static slow crack growth is used to generate a precrack from the sawed notch. The precrack can be arrested by unloading once it has extended the required distance. The pop-in crack technique has been used to generate precracks in materials that are not susceptible to stress corrosion cracking. This technique involves wedge loading at the root of a

sawed notch, combined with a crack arrestor, such as either a vice attachment that applies compressive stress ahead of the notch or a crack stabiliser[1, 2].

Other techniques used to introduce precracks in brittle materials with the notch bend geometry include[2]:

(a) *Compressive cyclic fatigue* – A bend specimen with finite notch tip radius is loaded in the specimen length direction with pulsating compressive stresses. During the compressive phases a microcrack zone develops ahead of the notch, with unloading resulting in a residual tensile stress field. These tensile stresses result in a continuously growing fatigue crack, but is limited to relatively short cracks of the order of a few millimetres[2].

(b) *Bridge indentation method* – A Vickers indentation is introduced in the specimen surface with one diagonal normal to the specimen length axis. The specimen is then placed on a plane support and loaded with a bridge as illustrated in figure 3.2. The precrack starts from the indentation and extends through the specimen thickness[2, 44].

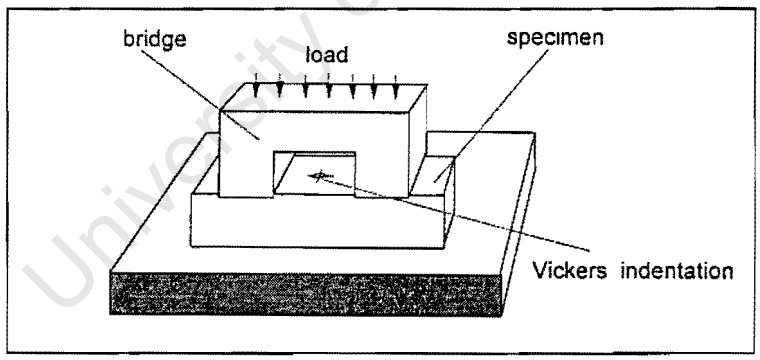

Figure 3.2: *Crack generation with the bridge indentation method [after ref. 2]*

For brittle materials with *R*-curve behaviour, precracking poses a serious difficulty to K_{Ic} determinations[1, 2]. A precrack extension, Δa_{pc}, leaves an active following wake region between the fracture surfaces behind the precrack tip[1]. Toughening mechanisms such as compressive residual stresses by crystallographic phase transformations, microcracking, crack bridging, etc. operate in this wake, and are believed to be the cause of the *R*-curve behaviour[1]. Fracture toughness values obtained from precracked specimens of materials with sharply rising *R*-curve

behaviour will thus always be higher than the true K_{Ic} value (which is defined as the critical stress intensity at the onset of crack extension)[1]. Precracking should therefore be avoided for straight through notches, as well as slow crack growth for chevron notches before determining K_{Ic} in materials with rising R-curve behaviour[1]. A diamond sawed sharp straight through notch with tip radius $\rho < \rho^*$ is preferable for testing these materials[1,2].

iv. Miscellaneous test conditions

Most structural applications of ceramics are at elevated temperatures. Examples include components for gas turbines and combustion engines. It is therefore important that toughness testing techniques can be used effectively at very high temperatures (in excess of 1000 ^{0}C). Bend tests are particularly suitable for this purpose[1].

Specimen geometries that are more complicated to machine should also be avoided whenever possible, since the inherent brittleness and high hardness of ceramic materials already make them difficult to machine. The most convenient tests in terms of ease of machining appear to be the indentation induced surface flaw techniques and the bend tests in the case of macronotch geometries[1].

3.2 Fracture mechanics specimens with macronotches

The fracture toughness testing techniques that have been most rigorously standardised for metals at ambient temperatures are the single edge notched bend (SENB) and compact tension (CT) specimens[1, 21, 23]. Other test methods that have been widely used on strong metals, as well as brittle ceramics include the double cantilever beam (DCB), double torsion (DT), and chevron notch geometries[1, 24, 25]. The literature shows a wide variation in fracture toughness values for similar materials of differing specimen geometry and / or test method[1, 28, 30 - 33]. This scatter of results has been partially attributed to differences in material composition and microstructure, and partially to real differences in the fracture behaviour (fast cracking, subcritical crack growth, *R*-curve behaviour, etc) among the different test techniques used[1]. Four of the most common and suitable (in terms of machining and test simplicity) *macronotch* test techniques for measuring K_{Ic} of brittle materials are discussed in the following sections.

3.2.1 Single edge notched bend bar (SENB) specimen

One of the most popular fracture toughness testing specimens is the single edge notched bend bar or beam (SENB). The specimen has gained its popularity through its simplicity of geometry and loading. Figure 3.3 shows a schematic diagram of a SENB specimen in 4-point loading.

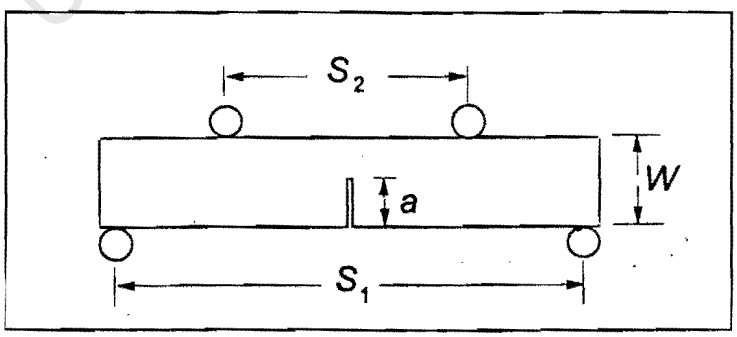

Figure 3.3: *SENB specimen in 4 point loading [after ref. 2].*

The SENB specimen has length L, thickness B, and height W. The outer (lower) and inner (upper) spans are S_1 and S_2 respectively. In the case of 3-point loading $S_2 = 0$. Either 3-point or 4-point loading can be used. The bending moment diagram for 4-

point loading has a maximum bending moment along the inner span length while the maximum bending moment in 3-point loading occurs at the application of the upper load at a single point. Alignment of the specimen is therefore critical in 3-point loading, whereas 4-point loading is not as critical, and therefore easier and more common in practice.

A notch of finite width and depth a is introduced into the specimen by a saw cut. The relative depth, $\alpha=a/W$, of the notch should lie in the range $0.45 \leq \alpha \leq 0.55$ according to K_{Ic} standards of metallic materials[21, 23], while an ESIS TC 6 round robin on K_{Ic} recommended a relative notch depth range of $0.3 \leq \alpha \leq 0.4$ [30]. The effect of notch width and tip radius ρ has already been discussed in Section 3.1.2, part iii. ASTM E399 – 90 recommends notch widths less than or equal to one-tenth the height, i.e. $2\rho \leq W/10$ [21]. Sherman showed that a notch of 0.3 mm width, which is a commonly used diamond blade thickness, could cause an overestimate of more than 30 % in K_{Ic} of ceramics[46].

The fracture toughness is computed from the specimen dimensions B and W, load spans S_1 and S_2, maximum load P_{max} and the relative crack length α according to[2]:

$$K_{Ic} = \frac{P_{max}}{B\sqrt{W}} \cdot \left(\frac{S_1 - S_2}{W}\right) \cdot \frac{3\Gamma_M \sqrt{\alpha}}{2(1-\alpha)^{3/2}} \qquad \textbf{(3.3)}$$

with

$$\Gamma_M = 1.1215\sqrt{\pi}\left[\frac{5}{8} - \frac{5}{12}\alpha + \frac{1}{8}\alpha^2 + 5\alpha^2(1-\alpha)^6 + \frac{3}{8}e^{-6.1342\frac{\alpha}{1-\alpha}}\right] \qquad \textbf{(3.4)}$$

Precracking ceramics is a very challenging task as described in Section 3.1.2, part iii. One of the precracking techniques described merely involves using a razor blade with diamond paste to sharpen the tip of the saw-cut notch to form a V-shape notch tip. This technique is simple, quick and economical. SENB specimens prepared with their notches sharpened will result in different stress intensity factors than the pure machined notches, due to the smaller notch tip radii (figure 3.1).

It is therefore necessary to distinguish between these two different types of SENB specimens:

- SENB-S for a specimen with only the saw-cut notch in it, S – for saw-cut; and
- SEVNB for a specimen with a sharpened notch using the razor blade and diamond paste, V- for sharpened V notch.

Advantages of the SENB-S method include a well-defined notch, easy measurement of the notch depth, and relatively inexpensive machining. The disadvantages include the absence of a sharp notch tip, and a need to determine ρ_{crit} to ensure a valid K_{Ic}[30]. Advantages of the SEVNB method include those of the SENB-S method in addition to a sharper well-defined crack. A possible disadvantage could be the presence of cracks at the tip of the V notch in some materials leading to underestimates in K_{Ic}[46].

Good to excellent results using SENB methods have been reported in the literature for a wide variety of ceramic materials[1 – 2, 4, 21, 23, 28 – 31, 41, 47 - 59]. Appendix A summarises some of the SENB test parameters reported in the literature. More comprehensive details on SENB fracture toughness testing can be found in the literature[1 – 2, 4, 21, 23, 27 – 31, 33, 41, 45 - 59].

3.2.2 Double torsion (DT) specimen

The double torsion (DT) test was first proposed by Outwater *et al.* and subsequently developed experimentally by Kies and Clarke[1, 39, 60]. It has been widely used successfully for studies of subcritical crack growth in ceramic materials, as well as for evaluating K_{Ic} of very brittle materials, such as ceramics, cements, brittle polymers and metals[1, 60].

The DT specimen is essentially a flat rectangular plate with proportions t:10t:30t for the thickness t, width W, and length L, respectively, as shown in figure 3.4 [39, 60]. The specimen can be loaded in either 3-point or preferably 4-point loading. Analysis of the specimen loading for K calculation treats the specimen as two separate bars subjected to torsion, hence the name *double torsion*.

A starter notch is cut from one end through the full thickness to about a quarter of the length along the centre line. Subsequent precracking induces a sharp 'natural' crack to satisfy the assumptions of LEFM. Grooves are sometimes formed in the top and / or bottom faces to force the crack to grow straight along the centre. The grooves however could be a source of stress concentration and have thus been a contentious issue[39, 60 - 62]. Careful control of specimen and load span positioning and alignment, however, improves the probability of straight cracks along the centre, whilst avoiding the contentious effects of grooves[39, 60]. Whether the mode of failure is actually strictly mode I has also been subject to huge debate[39, 60 - 69].

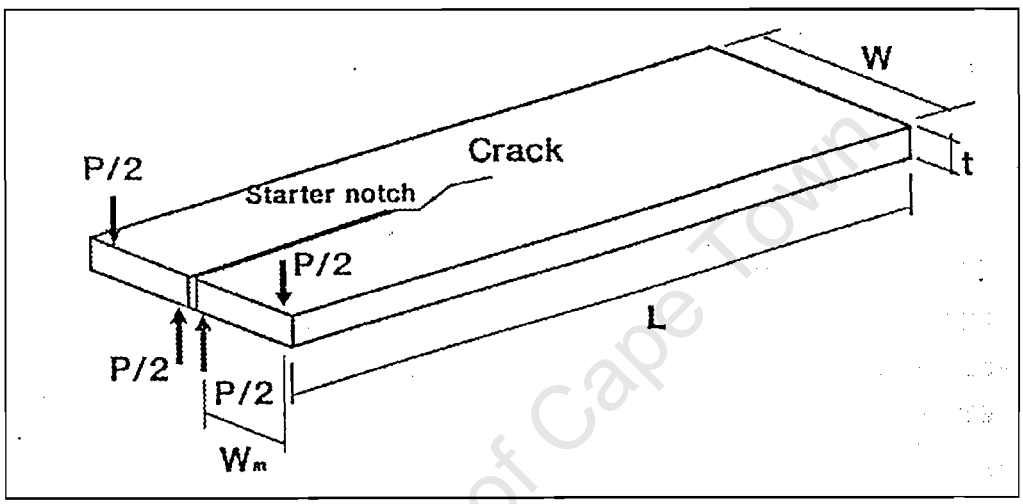

Figure 3.4: *The DT specimen in 4-point loading [after ref. 39]*

The stress intensity factor K_I of a DT specimen without grooves for plane strain conditions is given by equation 3.5 [1, 39, 60 - 69].

$$K_I = PW_m\left[\frac{3}{Wt^4(1-\nu)\xi}\right]^{1/2} \qquad \textbf{(3.5)}$$

where P is the applied load, W_m the moment arm, ν Poisson's ratio, and □ a correction factor, given in equation 3.6.

$$\xi \approx 1 - 0.6302\left(\frac{2t}{W}\right) + 1.20\left(\frac{2t}{W}\right)e^{\left(\frac{-\pi W}{2t}\right)} \qquad \textbf{(3.6)}$$

A specific advantage of the DT specimen design is that K_I is independent of crack length over a substantial portion of the specimen length, except for the initial and final 15 to 20 percent[39, 60 - 69]. Experimental studies as well as finite element calculations recommend the following crack length region to yield constant K_I [1]:

$$0.55(W/L) < (a/L) < [1-(W/L)] \tag{3.7}$$

where a is the crack length.

A critical disadvantage of the DT specimen is that the crack front is long and considerably curved – figure 3.5 [1, 39, 60 - 69]. It extends further along the tensile surface than the compressive surface, which is contradictory to the straight through crack assumption used in deriving the equation for K_I.

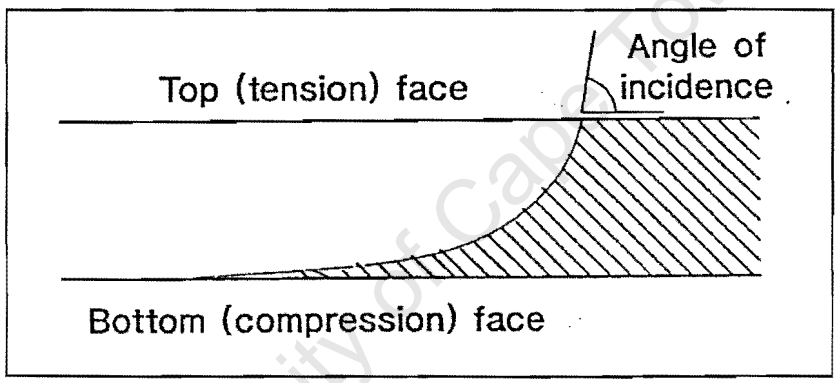

Figure 3.5: *Profile of the crack front for a DT specimen [after ref. 39].*

The displacement of the loading points u varies linearly with the applied load P according to $u = CP$, where C is the specimen compliance (which is the reciprocal of stiffness). The compliance C in turn varies linearly with crack length a

$$C = Ba + \mathrm{D} \tag{3.8}$$

where B and D are constants depending on the material. A theoretical value for B (= $\frac{dC}{da}$), B_{th}, is given in equation 3.9.

$$B_{th} = \frac{3W_m^2}{\mu W t^3 \xi(t/W)} \tag{3.9}$$

where μ is the elastic shear modulus of the specimen, and all the other variables have already been defined. It is easily seen that B is independent of the crack length. Experimental values of B are sometimes different from B_{th} [64, 65]. Kahraman *et al.*, working on Nicalon-Fiber-Reinforced CAS-II Glass-Ceramic Matrix Composites, reported a difference of less than 2% between the experimental and analytical values of B [64, 65].

There are two ways of performing a DT test, viz. [2, 32, 39, 60 – 69]:

- *Load-relaxation method*

This method involves applying and maintaining a constant displacement during the test. Inserting equation 3.8 into $u=CP$, and differentiating with respect to time leads to equation 3.10.

$$\frac{du}{dt} = (Ba + D)\frac{dP}{dt} + BP\frac{da}{dt} \tag{3.10}$$

If P_f is the load at the beginning of relaxation, with the corresponding crack length a_f, then with constant displacement $u=u_f$,

$$P(Ba + D) = P_f(Ba_f + D) \tag{3.11}$$

Further substituting 3.11 into 3.10 results in

$$\frac{da}{dt} = -\frac{P_f}{P^2}\left(a_f + \frac{D}{B}\right)\frac{dP}{dt} \tag{3.12}$$

The crack growth rate or velocity, V (= da/dt), therefore results directly from the load-relaxation rate dP/dt, the actual load P and the values P_f and a_f.

- *Constant loading method*

A constant displacement rate is applied at the loading points and the steady state value of the load P (obtained after a transient period) is recorded. Substituting $dP/dt = 0$ into 3.10 yields

$$\frac{du}{dt} = BP\frac{da}{dt} \tag{3.13}$$

The crack growth rate da/dt under the constant load P and prescribed displacement rate du/dt can consequently be computed. The entire V-K_I curve can be generated through incrementally changing du/dt.

Crack growth can be determined directly under a microscope or indirectly by using the compliance relation in equation 3.8. In principle a complete V-K_I curve can be determined from a single specimen. The effect of influencing parameters such as temperature and environment can be determined immediately by changing them during the test. The measurable crack growth rates however are limited to $V > 10^{-9}$ m/s [2].

Taylor used "ramp" tests with constantly increasing displacement with the machine in displacement control, and the measured load recorded on a chart plotter against time or displacement[39]. The signal was manually spiked as the crack passed marks on the specimen. This enabled correlation of the slope of the plot with crack length as well as calculation of the crack velocity[39].

Using the DT test, the fracture toughness K_{Ic} is determined as the right-hand limit of the V-K_I curve (figure 2.10). K_{Ic}, however, can be estimated for a particular crack velocity from the strain energy release rate G_{Ic}, where for plane strain[61, 64, 65],

$$K_{Ic}^2 = EG_{Ic}/(1-\nu^2), \text{ and } G_{Ic} = \tfrac{1}{2}B(P_c^2/t) \tag{3.14}$$

where P_c is the load corresponding to crack propagation at a given overall velocity, and B is the derivative of the *experimentally* determined compliance[60].

The literature covers much more detail on the DT technique[1 - 2, 32, 39, 60 - 69]. Appendix A summarises different specimen dimensions used for DT testing by previous researchers, as found in the literature review of this study.

3.2.3 Chevron notched (CVN) specimens

Chevron notched specimens are used to determine K_{Ic} of brittle ceramics from the maximum fracture load P_{max} without any information regarding the crack length. The elegance of these specimens is that they are designed such that, when using an adequately stiff testing machine, the crack is stable in its initial extension and requires an increasing load to keep it advancing until the load reaches a smooth maximum P_{max}, at which catastrophic fracture occurs[1, 2]. The fracture toughness thus determined from P_{max} is therefore always for an ideally sharp crack. This stable crack growth approach contrasts to that of other test techniques such as SENB, where catastrophic fracture occurs as soon as the critical stress intensity is attained.

Figure 3.6 shows the trapezoidal form of the crack profile of a chevron notched specimen after some crack extension.

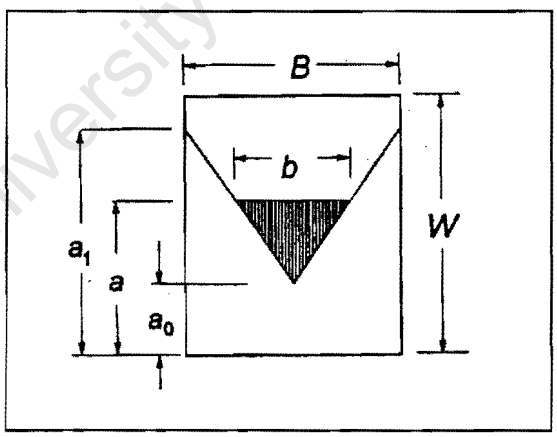

Figure 3.6: *Cross-section of chevron notch, with crack plane illustrated by shaded region; $\alpha_0=a_0/W$, $\alpha=a/W$, $\alpha_1=a_1/W$ [after ref. 2].*

Typical load-displacement (*P-u*) curves for chevron notched specimens are shown in figure 3.7.

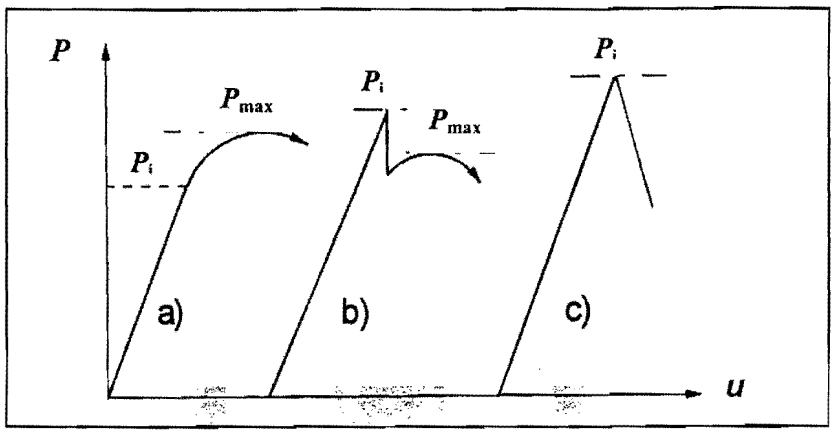

Figure 3.7: *Typical load-displacement plots for chevron-notched specimens [after ref. 2].*

For an ideally machined chevron notch with disappearing notch root radius, crack extension starts immediately upon loading. Due to the finite notch width, crack propagation would start at a finite initial load P_i. Curve (a) shows the desirable case $P_i<P_{max}$, where the crack extends stably from a_0 at P_i to a_{max} (which is independent of the specimen material[1]) at P_{max}, after which unstable catastrophic crack propagation follows. The non-linearity is due to crack propagation and an associated increase in compliance. $P_i>P_{max}$ in curve (b), with the sudden decrease in load indicating a limited amount of unstable crack extension. The load then increases again and reaches the smooth maximum P_{max}. In curve (c) crack arrest is not attained, resulting in catastrophic failure, and a maximum load therefore cannot be measured. Consequently K_{Ic} cannot be determined in such cases[2]. This occurs due to considerable overloads being applied, which in turn happens when the chevron size exceeds some critical value and the energy stored in both the specimen and the test machine is too high[1]. The load displacement curves of chevron notched specimens are therefore necessary to ensure the validity of the test[2].

The following expression was derived for the fracture toughness of chevron notched specimens[2, 70 – 77]:

$$K_{Ic} = \frac{P}{B\sqrt{W}} Y^* \qquad \textbf{(3.15)}$$

where Y^* is a geometric factor related to the relative crack length α – figure 3.8.

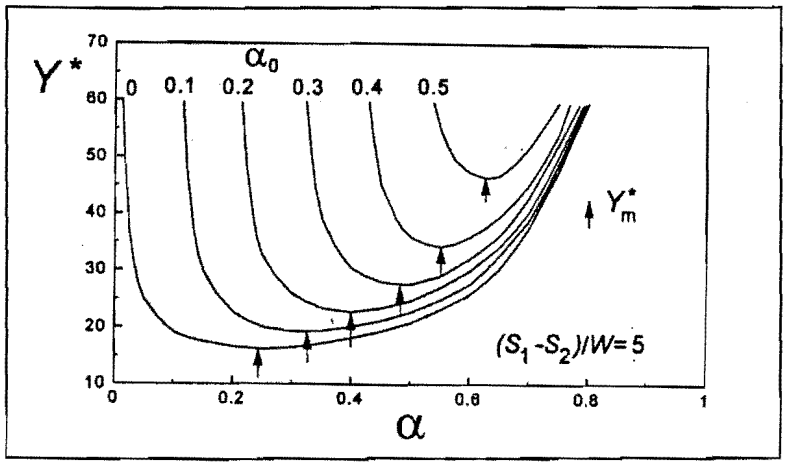

Figure 3.8: *Geometric function Y^* for a four point bending specimen with α_1=1 [after ref. 2].*

The function Y^* exhibits a minimum Y^*_m, (as indicated by the arrows in figure 3.8), which corresponds to the maximum load P_{max}. Equation 3.15 can therefore be rewritten as[2]

$$K_{Ic} = \frac{P_{max}}{B\sqrt{W}} Y^*_m \qquad \textbf{(3.16)}$$

Calculating K_{Ic} therefore requires the geometric function Y^* for different specimen geometries (W, H, B) and notch geometries (α_0, α_1). These can be found in references 70 – 71, and 80 - 83. For ceramic materials with R-curve behaviour, chevron notched specimens measure a larger K_{Ic} than other testing methods, with the K_{Ic} value dependent on specimen geometry and size[30].

Advantages of chevron notched specimens include a sharp crack being formed at the chevron tip as soon as the crack initiation load P_i is reached, easy measurement of maximum load, and crack length measurements not being necessary. The major disadvantage is the relative expensive machining of the chevron notch[30].

The three most common types of specimens with chevron notches are the short bar, short rod, and 3-point or 4-point bending specimens. Two of these, viz. the four-point bending and the short rod specimens are discussed next.

3.2.3.1 Chevron notched bend bar (CVNB) specimen

The chevron notched bend bar is simply a bend bar with a chevron notch in its centre, as illustrated in figure 3.9. The specimen can also be loaded in either 3-point or 4-point bending, with 4-point bending being preferable, due to reasons already given in Section 3.2.1

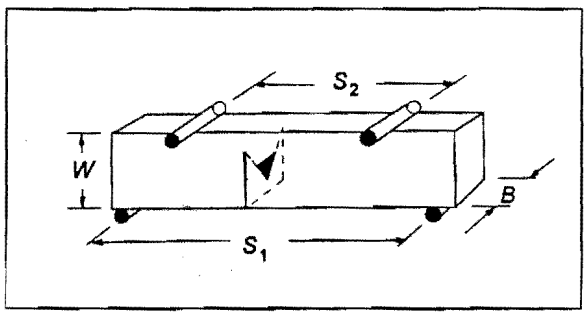

Figure 3.9: *Chevron notched bend bar to be loaded in 4 point bending [after ref. 2]*

K_{Ic} is calculated from equation 3.16, with geometric factors Y^*_m for 4-point bending in references 2, and 71 – 72. More information regarding the application of the CVNB technique can be found in the literature[1, 2, 24, 25, 70 - 73]. Appendix A summarises CVNB specimen dimensions used by previous investigators, as found in the literature.

3.2.3.2 Chevron notched short rod (CVSR) specimen

The chevron notched short rod (CVSR) was first introduced by Barker in 1977[74]. A schematic of the CVSR is shown in figure 3.10.

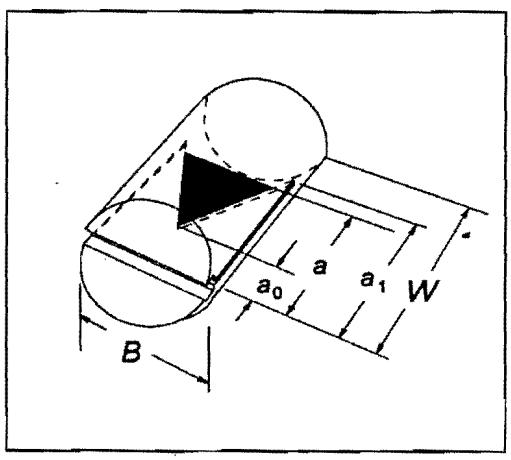

Figure 3.10: *Chevron notched short rod [after ref. 2]*

The CVSR specimen is pulled apart in tension through either the use of loading grips, or by applying pressure to a thin inflatable bladder called a flatjack placed inside the specimen[75, 84].

K_{Ic} is again calculated using equation 3.16. The dimension W is neither the height of the specimen (as in the CVNB) nor the specimen length, but is measured from the load line (line of application of load) to the end of the specimen, as illustrated in figure 3.11. Y^*_m can be found in references 2, and 80 – 83.

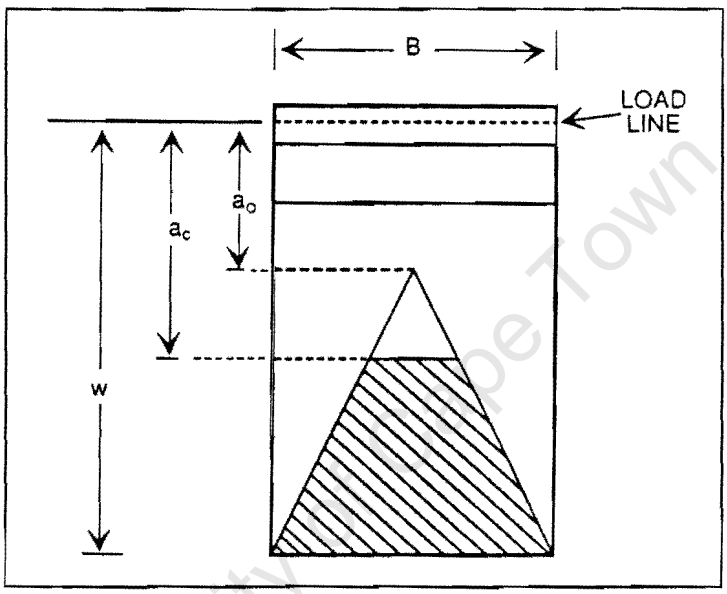

Figure 3.11: *Section view of chevron notched specimen with the various dimensions defined. The crack is shown at the critical length a_c [after ref. 76].*

The CVSR test has been standardised for metallic and carbide materials[24, 25]. More details regarding the CVSR test can be found in the literature[1, 2, 24, 25, 74 - 88]. Appendix A summarises some of the CVSR test dimensions used by previous researchers, as found in the literature review of this study.

3.3 Fracture mechanics specimens with microflaws

Fracture around hardness indentations in brittle materials has been observed since the inception of hardness testing, with the cracks initially being considered a detriment to effective hardness measurements on brittle materials[1, 89]. Fortunately, early investigators such as Palmqvist recognized that such cracking must serve as some measure of the toughness of the material[90]. Since then, indentation fracture has become an important technique in studying the mechanical properties of ceramics[1, 2, 4, 5, 30, 32 – 34, 41, 89].

The indentation technique to estimate fracture toughness has two unique advantages, in that the technique is[89]:

- Easy to perform and can be applied to very small specimens, as the technique requires only a small polished area on the specimen surface, from which a large number of data points can be rapidly generated.

- Capable of measuring the local crack growth resistance $(K_c)_i$ of a material, e.g. the micro-toughness pertinent to cracks on the order of the microstructural dimensions.

The dimensions of the indentation impression and the induced flaws are readily controlled through the contact load[1]. The two major pointed indenter geometries used to induce surface microflaws have been the Knoop and Vickers configurations, since these are readily available commercially[1]. Figure 3.12 shows the typical surface crack patterns produced by Vickers and Knoop indenters respectively. Curved indenters result in the formation of *hertzian cone cracks*[90].

Sakai and Bradt classified the microflaw techniques used to determine fracture toughness into two categories, viz. the controlled surface flaw technique and semi-empirical techniques[1]. Sections 3.3.1 – 3.3.3 discuss indentations and their associated residual stresses and resulting crack patterns, while Sections 3.3.5 and 3.3.6 discuss

the techniques that use indentations to measure K_{Ic}, viz. the controlled surface flaw and semi-empirical techniques.

3.3.1 Residual stresses

Indentations result in an effective plastic central zone with associated residual stresses beneath the immediate contact area[1]. The residual stress field is complex and poses problems in determining the fracture toughness[1, 89 - 91]. Figure 3.12 shows cross-sectional schematics of Vickers and Knoop indentations together with the residual stress fields.

In situ. observations of radial crack evolution during Vickers indentation in transparent materials indicated that the final crack configuration was achieved as the indenter was removed from the surface[90, 91]. This demonstrated that the driving force for crack growth is provided by the residual stress field[90, 91].

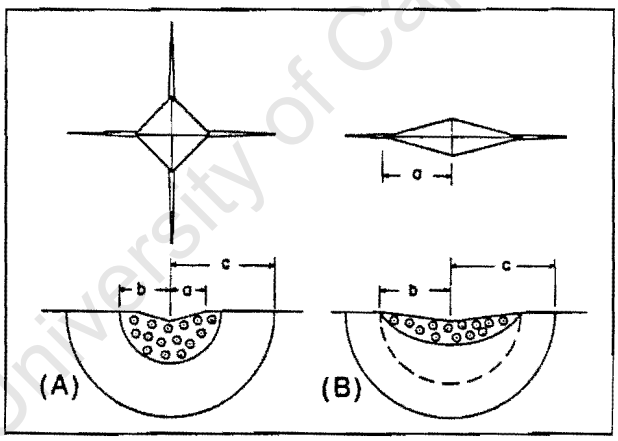

Figure 3.12: *Surface (top) and cross-sectional (bottom) schematic diagrams of (A) Vickers and (B) Knoop indentations. Residual stresses act normal to the crack plane, which lies in the plane of the page, and are represented by the circled points within the plastic zone [after ref. 91].*

3.3.2 Knoop indentations

Knoop indentations create a single, nearly semicircular surface crack, which is shown in figure 3.13. The dimensions of the hardness indent at the surface are length, L, and width, b. The crack formed has depth a, and width $2c$.

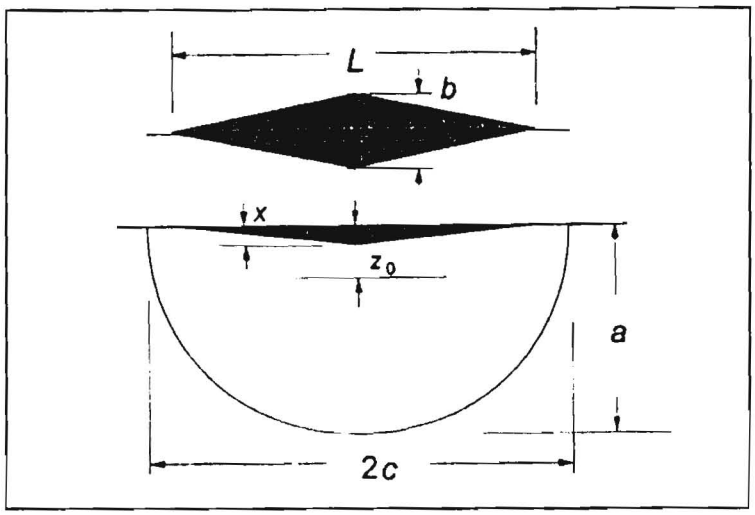

Figure 3.13: Geometrical data of a Knoop indentation crack [after ref. 2].

The different stages of crack development are illustrated in figure 3.14 and described below[2].

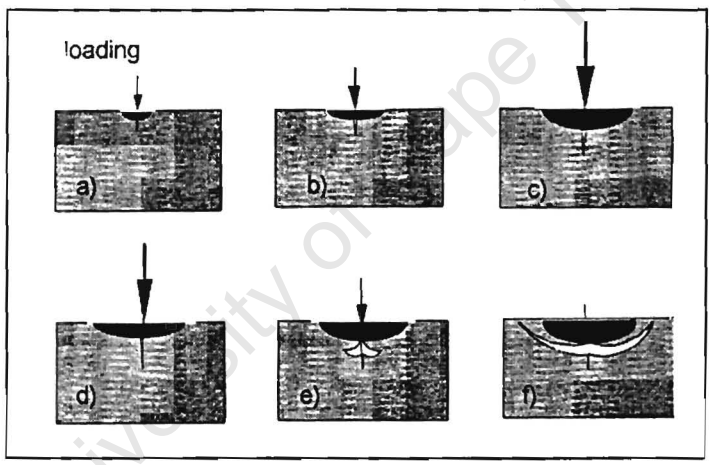

Figure 3.14: Development of cracks under a Knoop indenter [after ref. 2].

(a) In the region close to the contact location, non-linear deformations occur, due to plasticity and predominantly the creation of microcracks.

(b) At a critical load, the main crack arises from the initial damaged region.

(c) The crack propagates with increasing load.

(d) The damaged region closes due to unloading.

(e) – (f) Lateral cracks also develop during the unloading phase[2].

After unloading, the damaged region is under compressive residual stresses (figure 3.12 b), which are balanced by the tensile stresses near the crack tip region[2].

3.3.3 Vickers indentations

A Vickers indenter results in a two-crack system, with the cracks at right angles to each other, and parallel to the indentation diagonals. The development of Vickers indentation cracks is illustrated in figure 3.15 and described below[2].

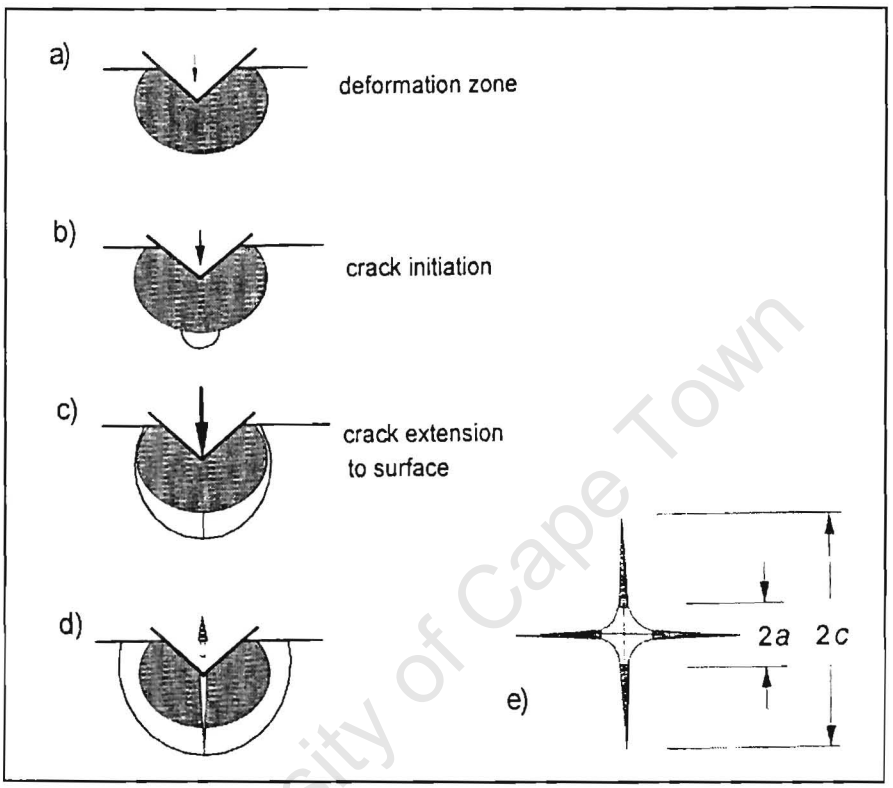

Figure 3.15: Development of Vickers indentation cracks [after ref. 2].

(a) A deformation zone develops below the Vickers pyramid close to the point of contact,

(b) Loading and unloading results in two perpendicular cracks being initiated at the deepest location of the deformation zone,

(c) These cracks then propagate to the specimen surface to result in the radial cracks at the surface,

(d) The final crack is nearly semicircular,

(e) The crack length at the surface is taken as $2c$ and the length of the indentation diagonal $2a$ [ref. 2].

After unloading, the damaged region is under compressive residual stresses (figure 3.12 a), which are balanced by the tensile stresses near the crack tip region[2].

Vickers indentations result in two dominant crack profiles, viz. median and Palmqvist, which are illustrated in figure 3.16[1, 2, 4, 5, 89, 90].

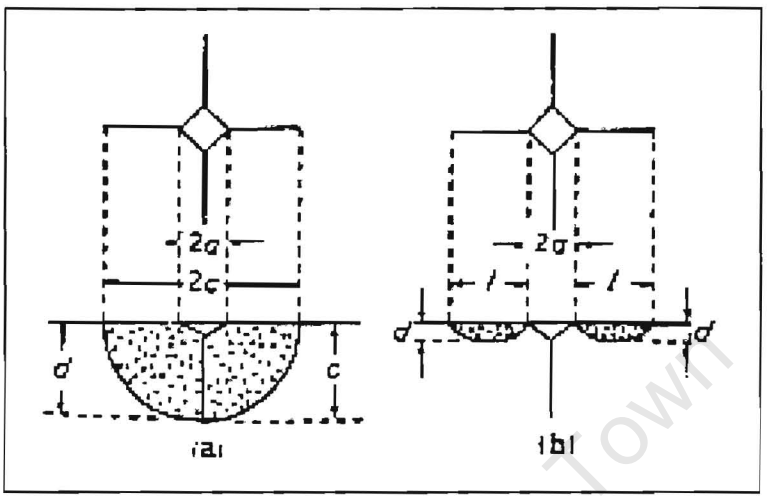

Figure 3.16: *Comparison of (a) median, and (b) Palmqvist cracks around a Vickers hardness indentation [after ref. 4].*

Palmqvist cracking (as shown in figure 3.16) occurs in relatively high toughness materials such as WC-Co materials, and at relatively low loads, before the subsurface median crack can be formed. The length of the Palmqvist cracks, l, is measured from the ends of the impression diagonals, with $c = a + l$ [1, 2, 4, 89 - 93]. Both median and Palmqvist cracks show similar patterns on the specimen surface, as evident in figure 3.16, thus making it difficult to distinguish which crack system develops from the surface alone[30].

Niihara *et al.* distinguished Palmqvist cracks from median cracks by using different ratios of c/a. They found that the crack profile is of median type for higher c/a ratios ($c/a \geq 2.5$) and of Palmqvist type for lower l/a *or* c/a ratios ($l/a \leq 2.5$ or $c/a \leq 3.5$)[1, 2, 4, 89 - 93].

The median and Palmqvist cracks are empirically distinguished by their load, P, and induced crack length, c_o, relations[1, 2, 4, 89 - 93]:

$$\textit{Median cracks} \quad - \; c_o = A' P^{2/3} \tag{3.17}$$

$$\textit{Palmqvist cracks} \; - \; l = P/4\omega \;\; OR \;\; c_o = BP + DP^{1/2} \tag{3.18}$$

where P is the applied indenter load, A', B, and D are constants related to the fracture toughness and hardness of the indented material (and ω is the crack resistance defined by Exner, based on the observed linear relationship between the indentation load and average crack length l)[1, 2, 4, 89 - 93]. Large errors in measurements of the crack lengths can make it very difficult to distinguish between the two crack profile systems from the experimental data, due to the experimental relationship between c_o and P for the median and Palmqvist cracks being similar. Sakai and Bradt, however, modified the equations 3.17 and 3.18 to yield a more sensitive form, which will differentiate between the different crack systems[1]:

$$\textit{Median-radial cracks:-} \; c_o/P = A' P^{-1/3} \tag{3.19}$$

$$\textit{Palmqvist cracks:} \; - \; c_o/P = B + DP^{-1/2} \tag{3.20}$$

The expression of c_o/P versus $P^{-1/3}$ or $P^{-1/2}$ emphasises the indentation cracking behaviour at low load, as shown in figure 3.17.

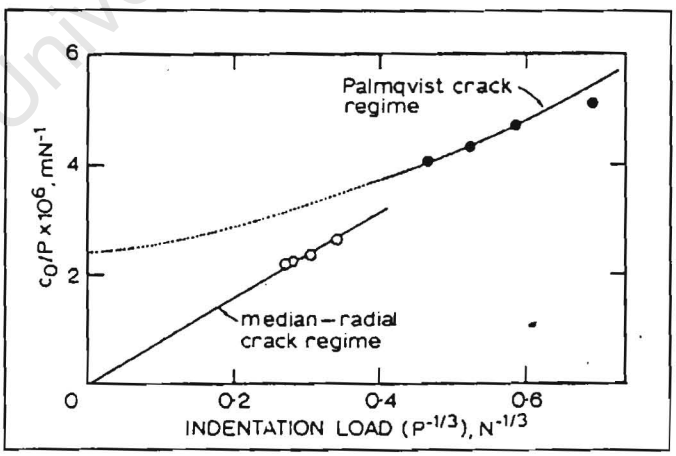

Figure 3.17: *Interrelation of indentation induced crack length c_o and indentation load P for hot pressed SiC ceramic. These relations were calculated using equations 3.19 and 3.20, where $A' = 7.85$ $\mu mN^{2/3}$, $B = 2.45$ μmN^{1}, and $D = 5.08$ $\mu mN^{1/2}$ [after ref. 1].*

From figure 3.17 it can be seen that there is an obvious transition from Palmqvist to median regimes with increasing indentation load (or decreasing $P^{-1/3}$). Liang *et al.* in fact showed that the crack profile changes from Palmqvist type to median type more easily when the material is more brittle, or rather when the material has a low toughness[4]. Therefore the crack profile is mainly of median type when the toughness values are low, and of Palmqvist type when the toughness values are high enough. They also observed that this transition is a function of the applied load. The crack profile is therefore a function of the properties of the material and the applied load[4]. Figure 3.18 shows crack profiles on different materials that Liang *et al.* worked on.

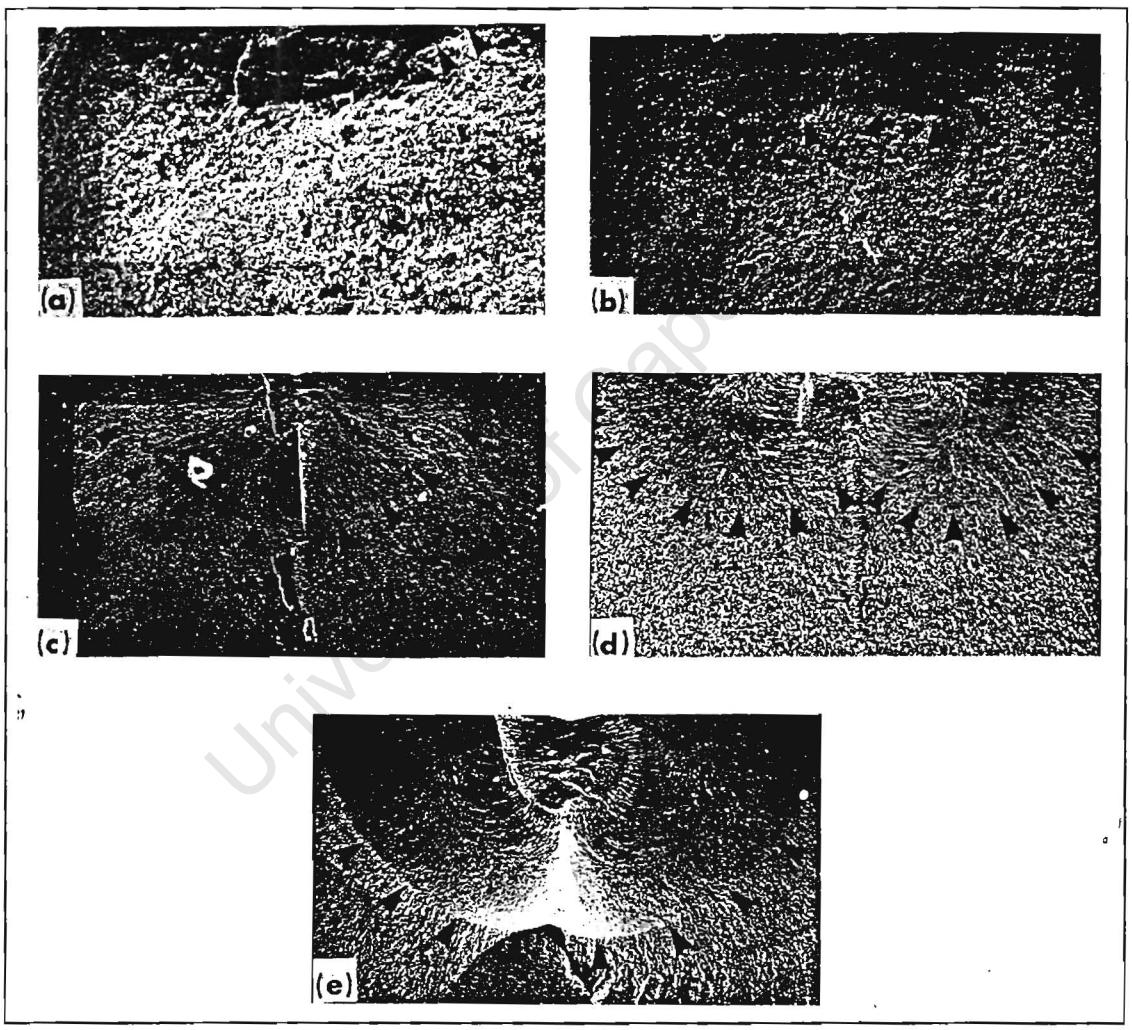

Figure 3.18: *Crack profiles on different materials, arrows indicate the edge of the crack front in each figure. (a), (b), (c) Al_2O_3 with 15 % ZrO_2 – (a) 10 N indentation load, Palmqvist, (b) 100 N load, Palmqvist, (c) 500 N load, median; (d), (e) TZP – (d) 100 N load, Palmqvist, (e) 500 N load, median [after ref. 4].*

When the applied load P is smaller than some load P_A, then the crack length corresponds to the Palmqvist model, and when P is larger than a greater load P_B it corresponds to the median model. P_A and P_B values are greater in the tough materials than in the lower toughness materials[4]. The load range of the Palmqvist type is therefore larger in the high-toughness materials than in the low-toughness ones. The crack profile is in a transition state, i.e. between these two types, when $P_A \leq P \leq P_B$. When the crack profile is in a transition state, the *c/a* ratio is at a median ratio, i.e. is not large (for median cracks), and not small (for Palmqvist cracking). Liang *et al.* reported P_A and P_B values for alumina as 88N and 176N respectively[4].

3.3.4 Controlled surface flaw (CSF) technique

The controlled surface flaw (CSF) technique was developed in the early 1970's by Petrovic and colleagues as an alternative to classic fracture mechanics tests using large saw-cut precracks[94]. This method is also called the surface crack in flexure (SCF) technique.

The technique involves placing a single controlled surface flaw of suitable size on the polished tensile surface of a bend specimen and accurately aligning it perpendicular to the tensile stress direction, to result in fracture initiation at the site of this flaw since it is the worst flaw in the specimen[94]. A schematic of a controlled surface flaw in a bend specimen is shown in figure 3.19.

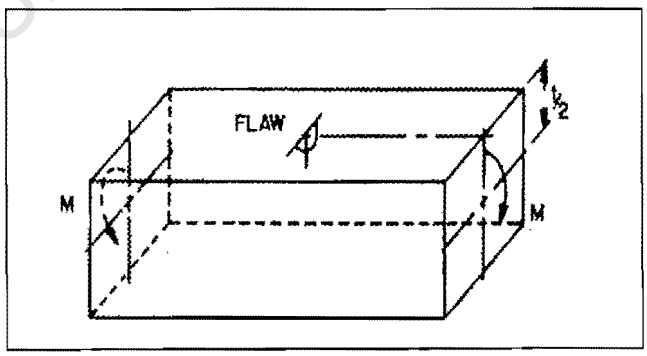

Figure 3.19: *Schematic of a controlled surface flaw on the tensile surface of a four-point bend specimen [after ref. 94].*

Knoop indenters were most commonly used to introduce the surface flaw into the material for the following reasons. First, there is no crack perpendicular to the primary surface flaw with the Knoop indentation as opposed to the Vickers indentation. Secondly, orientation of Knoop surface flaws is more convenient and controllable, since alignment is achieved by aligning the long axis of the Knoop indentation. The surface flaws produced by Knoop indentation are highly reproducible, and are "controlled" in the sense that their basic sub-surface shape is semi-elliptical and their size is determined from the applied indenter load[1, 94]. Loads commonly used to induce the Knoop surface flaws are 24.5 N (2.5 kg) and 49 N (5 kg). The 2,5 kg was the lowest load found to be used in the literature[94 - 97].

Petrovic *et al.* made the critical observation that the residual stresses underneath the impression were influencing the computed fracture toughness (figure 3.20)[94, 96]. They demonstrated that annealing or polishing were effective means to eliminate the residual stresses. Most researchers however avoid annealing due to the possibility of crack tip blunting or flaw healing at elevated temperatures[96]. The indent and sub-surface damage zone are usually removed to a depth of 3 to 5 times the depth of the indentation in order to remove residual stresses, as well as force the maximum stress intensity to be at the deepest portion of the crack front (figure 3.21).

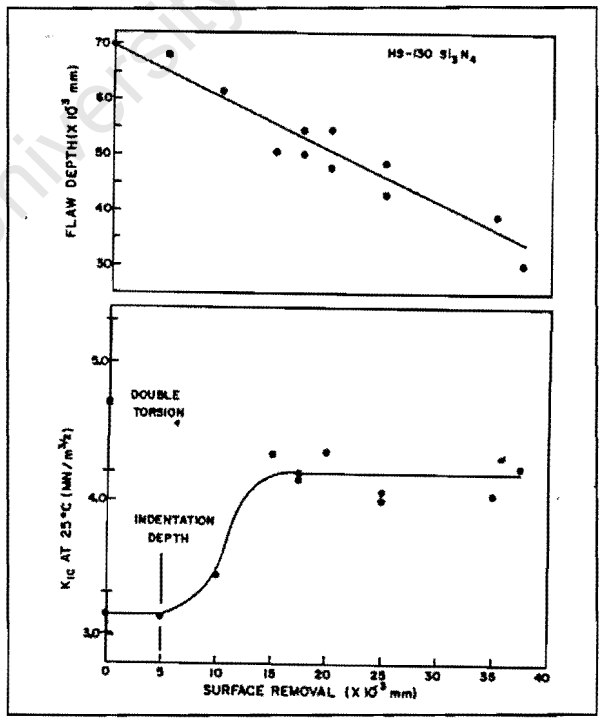

Figure 3.20: *Effect of surface polishing on room temperature K_{Ic} values obtained by the CSF technique for hot-pressed Si_3N_4 [after ref. 94].*

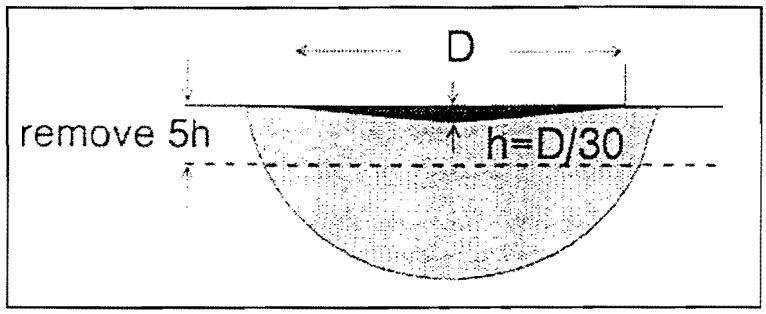

Figure 3.21: *Schematic of a Knoop indentation with semi-elliptical pre-crack formation in flexure specimen. The Knoop hardness impression has a depth h. Removing by polishing approximately 5h from the specimen's surface has been recommended by researchers to ensure complete removal of the damage and residual stress zone [after ref. 97].*

The CSF technique requires the measurement of the semi-elliptical surface crack depth a, and width $2c$ (figure 3.22). The stress intensity factor K_I varies along the crack front, and it has extreme values at the ends of the major and minor axes of the semi-elliptical flaw. The stress intensity shape factor Y is determined for both the deepest point, Y_{depth}, and at the surface, $Y_{surface}$ using the empirical stress intensity factor equation developed by Newman and Raju (Appendix B)[2, 97]. The maximum Y (either Y_{depth} or $Y_{surface}$) is used in the conventional equation for fracture toughness.

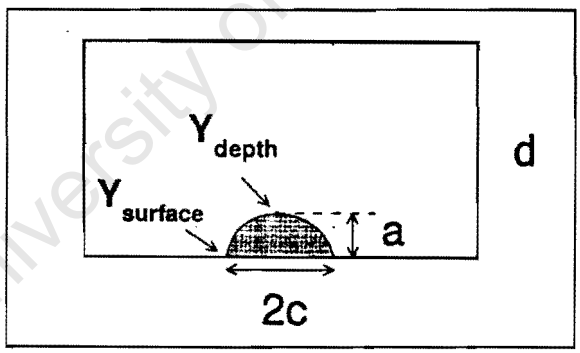

Figure 3.22: *Schematic of pre-crack configuration – d is the specimen height, a the crack depth, 2c the crack width, $Y_{surface}$ and Y_{depth} are the stress intensity shape factors at the surface and deepest point of the crack periphery [after ref. 97].*

Fracture toughness K_{Ic} is computed from the simple formula

$$K_{Ic} = Y_{max}\sigma\sqrt{a} \qquad \textbf{(3.21)}$$

where Y_{max} is the maximum of Y_{depth} or $Y_{surface}$, σ_f the fracture stress or flexure strength of the specimen, and a is the crack depth.

The calculated toughness therefore depends on the stress at fracture, and the precrack size and shape. The stress is usually measured very accurately and precisely. Since toughness is proportional to the square root of crack size, the uncertainty in the size measurement is diminished in the calculated results. Fractographic experience, however, has been identified as a prerequisite for the assurance of correct results, since precrack detection has been a problem[95, 96]. Quinn *et al.* identified some new techniques to enhance precrack detection[96]. These include tilting the specimen during indentation, illuminating from low angles with optical microscopy, sputter coating at a grazing angle, tilting the specimen in the SEM, using backscattering mode in the SEM, and stereo SEM photography[96].

The crack depth at fracture ($a_{critical}$) may be different from the initial flaw ($a_{initial}$) due to stable crack extension, slow crack growth (SCG), or chemically assisted slow crack growth (figure 3.23). These effects are discussed in more detail by Scherrer *et al.*[97]. The final crack dimension $a_{critical}$ is used for the fracture toughness determination[97].

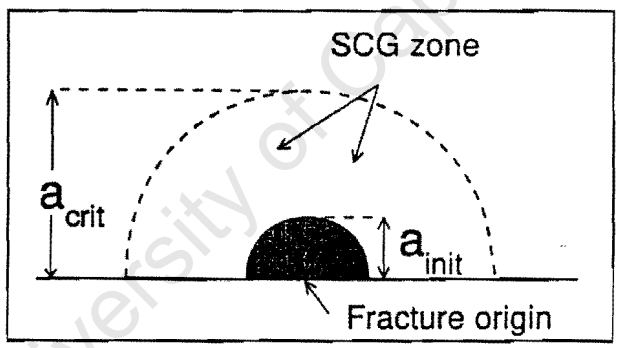

Figure 3.23: *Schematic of growth of a pre-crack due to stable crack extension. Initial crack depth $a_{initial}$ corresponds to the indentation crack formation and extends to a critical size $a_{critical}$, which corresponds to the final crack dimension just prior to fracture [after ref. 97].*

Some advantages of the CSF technique are[94]:

- A simple bend bar specimen geometry is used;
- Potential exists for adaptation of the technique to other specimen geometries, and;
- The controlled surface flaw approximates natural failure defects in brittle materials.

There are also certain disadvantages associated with this test method[94]:

- Residual stress effects;
- Flaw "healing" at elevated temperatures during annealing;
- Difficulty in observation of the flaw profile on fracture surfaces, and;
- Possible applicability of the technique to a limited range of brittle materials. For example the CSF method using a Knoop indenter has been unsuccessful in zirconia due to the inability to form a sufficiently large median precrack, which is most probably due to the much higher toughness of zirconia when compared to other brittle materials[95, 96].

Very consistent results have been reported by different researchers using this technique on a variety of materials[95 - 97]. This section on the CSF technique is probably best concluded by Evans summary of the state of indentation microflaw testing: "Many of the indentation methods are only approximate and do not provide the quality of fracture resistance data needed to rigorously relate toughness to microstructure. The surface flaw methods, introduced first by Petrovic and Jacobson, seem to be the most precise, provided that residual stresses are eliminated by polishing out the plastic zone"[95].

3.3.5 Semi-empirical techniques

3.3.5.1 Indentation microfracture (IM)

Micro-indentation techniques, where the lengths of the cracks emanating from the corners of a hardness indentation are used to estimate the fracture toughness of brittle materials were proposed over three decades ago. The IM method has attained considerable popularity, due to its ease of application, since no extensive machining or preparation of test specimens is required, with only a small specimen being needed.

The Knoop hardness indenter produces surface cracks, which are difficult to measure, and not much longer than the long indent diagonal[98]. The Knoop indenter also requires higher loads than a Vickers indenter to produce cracks of the same length[98].

In a study of cracks produced by various indenter types on soda-lime glass, Marion showed that the cracks produced by Vickers indenters were the easiest to measure and had the smallest scatter[98]. Most of the literature on indentation microfracture techniques also focuses much more on the Vickers indenter geometry. This review will therefore also focus exclusively on the Vickers indentation microfracture analyses.

Note that the symbol K_{Ia} is used to define the fracture toughness determined from indentation, since the result is different in kind from conventional K_{Ic}, tests which measure the ability of the material to resist the initiation of crack propagation from a pre-existing macroscopic defect, such as a crack or notch. In an ideal brittle material K_{Ic} and K_{Ia} are equivalent[99].

It is difficult to determine fracture toughness from the Palmqvist crack system in brittle materials due to the relatively short crack lengths produced. This results in significant errors in the measurements of the crack length l, and a large statistical variation[1]. This suggests that the median-radial crack system is more applicable to brittle materials. Spiegler *et al.* however concluded that Palmqvist crack models were much more applicable to WC-Co cermets than the median crack models, as median cracks were **not** generated in these materials, even at high loads[90]. This is due to the much higher fracture toughness of the WC-Co cermets compared to brittle materials.

Considering the median-radial crack system, it has been convenient to separate the problem into the elastic and residual plastic components[1]. After the necessary fracture mechanics analyses (which can be found in reference 1), a simple expression for fracture toughness was found[1]:

$$K_{Ia} = A(E/H)^n P/c_o^{3/2} \qquad \textbf{(3.22)}$$

where the constants A and n are determined empirically.

Table 1 gives a summary of empirically determined values of A and n for a number of toughness expressions proposed for median crack systems. Figure 3.24 depicts the dimensionless forms of equation 3.22, i.e. $(K_{Ia} / P/c_o^{3/2})$ $(= A(E/H)^n)$ as functions of

E/H. Values of *E/H* for most ordinary brittle ceramics range from 15 to 30, and therefore this region is hatched in figure 3.24.

Table 1: Fracture toughness expressions in median-radial crack system [after ref. 1].

Researcher	***Figure 3.24, equation?***	***A***	***n***
Lawn-Fuller	A	0.0726	0
Tanaka	B	0.0725	0
Tanaka	C	0.035	0.25
Niihara-Morena-Hasselman	D	0.0309	0.50
Anstis-Chantikul-Lawn-Marshall[92]	E	0.016	0.40
Lawn-Evans-Marshall	F	0.0175	0.50
Miyoshi	G	0.018	0.50

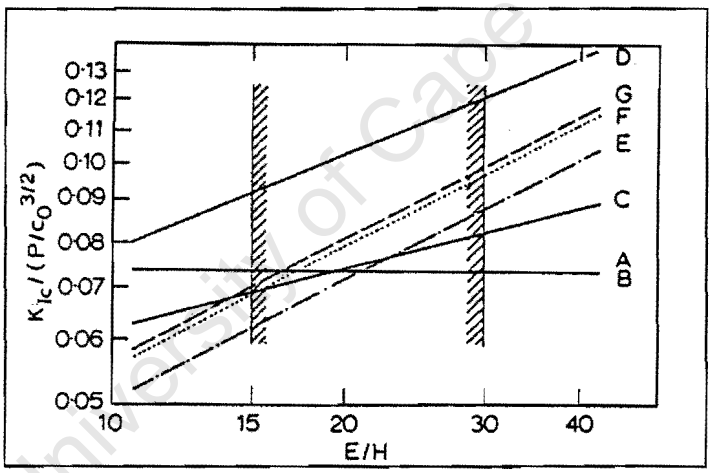

Figure 3.24: *Fracture toughness expressions (A-D) in median-radial crack system plotted against E/H – hatched region (15<E/H<30) represents E/H range for ordinary brittle materials [after ref. 1].*

The empirical equations *E-G* in Table 1 have been generally recognized to be the most reliable for obtaining fracture toughness estimates[1]. Equations *A-G* should be applied only to median-radial crack systems, and only if the following conditions are met[1]:

1. The thickness of the test specimen must be great enough to allow for the full development of the median-radial crack system. It has been suggested that the thickness exceed ten times the radial crack length c_o.

2. Only perfect indentation induced cracks must be used for each Vickers indentation, i.e. a symmetrical pyramidal impression, a well defined symmetrical crack pattern of four nearly equal straight cracks originating from the indentation corners. Chipping or side cracks should not be allowed.

3. The crack system must satisfy the relation $P/c_o^{3/2} = constant\ (=K_{Ia} / A(E/H)^n)$ *or* $c_o/P = [A(E/H)^n / K_{Ia}]^{-2/3}P^{-1/3}$. The fracture toughness should be estimated from the slope of the linear plot of P versus $c_o^{3/2}$ or c_o/P versus $P^{-1/3}$, which must go through the origin of the graph. The test should encompass a relatively wide range of indentation loads from at least 10 to 300 N. Figure 3.25 shows an example for an alumina ceramic.

4. Pre-existing (residual) stresses - such as in tempered glasses, machining induced compressive stresses, phase transformation induced compressive stresses, etc. – are not permissible on the test surface.

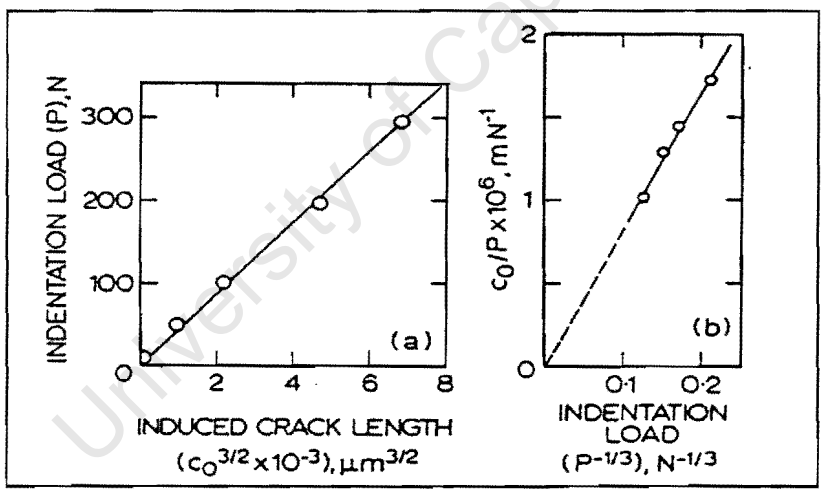

Figure 3.25: *Relations between indentation load P and indentation induced median-radial crack length c_0 for Al_2O_3 ceramic. K_{Ic} is computed from the slopes of the straight lines – (a) $K_{Ic}/A(E/H)^n$ and (b) $[A(E/H)^n/K_{Ic}]^{2/1}$ [after ref. 1].*

5. The material *must* show a flat R-curve behaviour. Rising R-curve behaviour will yield a curved line for the P versus $c_o^{3/2}$ plot, so that the indentation fracture toughness of the material will have an ambiguous meaning. Fracture toughness K_{Ic} is defined and measured at crack initiation, not evaluated after a certain amount of crack extension as in the IM method, where fracture toughness is

estimated using arrested crack lengths, perhaps related to some ill-defined toughness value for crack arrest K_a.

6. To avoid possible disruption of the crack patterns, the indentation induced crack length, c_o, must be much greater than the characteristic dimension of the ceramic microstructure, such as the grain size. Crack lengths at least ten times the grain size have been recommended[1].

It can be seen from equation 3.22 that the fracture toughness in an indentation microfracture test is dependent on the applied load P, the indentation diagonal length $2a$ (which also determines the hardness of the material), the crack length $2c$, and the elastic modulus E. Over the last two decades, several expressions have been determined by different authors to estimate fracture toughness through indentation techniques. Some of these formulae are restricted to median cracks, others to Palmqvist cracks; while some are even restricted to certain materials[4]. Most of the formulae include a non dimensional factor $(E/H)^a$, which attempts to account for the residual stresses beneath the indentation.

Liang *et al.* developed a new formula in 1990 to obtain independent values of K_{Ic} for brittle materials, by treating K_{Ic} as function of Poisson's ratio ν, as well as hardness H and elastic modulus E. They state that this new formula can be used with any load in an indentation test for any crack profile (i.e. Palmqvist, median, or transition). Guillou *et al.* performed a study on the application of indentation fracture testing to ZrO_2, SiC, and Si_3N_4, to compare 20 indentation data analysis formulae, with the idea of enabling the use of a single equation to interpret the results in a self-consistent manner[99]. A few of these formulae are listed in Table 2. Guillou *et al.* concluded that the equation of Liang *et al.* had potentially the greatest range of applicability, with the equations by Evans and Anstis *et al.* being the main alternatives.

Some of these equations are listed in Table 2[99]. More equations can be found in Guillou *et al's.* paper[99] and in the literature[1, 2, 4, 5, 30, 32 – 34, 41, 89 - 104].

Table 2: Some expressions for indentation fracture toughness K_{Ia}. [after ref. 100].

Equation	**Researcher/s**	**Year**
[1] $K_{Ia} = 0.4636(P/a^{3/2})(E/H_v)(10^F)$	A. G. Evans	1979
[2] $K_{Ia} = 0.0154(P/c^{3/2})(E/H_v)^{1/2}$	G. R. Anstis *et al*[92]	1981
[3] $K_{Ia} = 0.0089P/(al^{1/2})(E/H_v)^{2/5}$	K. Niihara	1983
[4] $K_{Ia} = (0.3474/f(\nu))(E^{0.4}P^{0.6}/a^{0.7})(c/a)^Y$	K. M. Liang *et al*[4]	1990

The exponent F in equation [1] from Table 2 is given by[99]:

$$F = -1.59 - 0.34\log(c/a) - 2.02[\log(c/a)]^2 + 11.23[\log(c/a)]^3 - 24.97[\log(c/a)]^4 + 16.32[\log(c/a)]^5$$

The function $f(\nu)$ and the exponent Y from equation [4] are given below[4, 99]:

$$f(\nu) = \left[1 - 8\left(\frac{4\nu - 0.5}{1+\nu}\right)^4\right]$$

and

$$Y = \left(\frac{c}{18a}\right) - 1.51$$

Spiegler *et al.* in their study of fracture toughness testing of WC-Co alloys by indentation testing, found that the median models due to Lawn *et al.*, and Evans and Charles show a clear load dependence[90]. This is illustrated in figure 3.26 a. They attributed this load dependence of toughness to the inadequate description of the Palmqvist cracks in WC-Co by the median models. Figure 3.26 b shows the load independence of K_{Ic} in the Palmqvist models. It is interesting however that the Anstis *et al.* median model (in figure 3.26 a), and some other median models such as those due to Laugier or Niihara (not shown in figure 3.26 a) also show no load dependence. These models may however result in large overestimates for K_{Ic}[90].

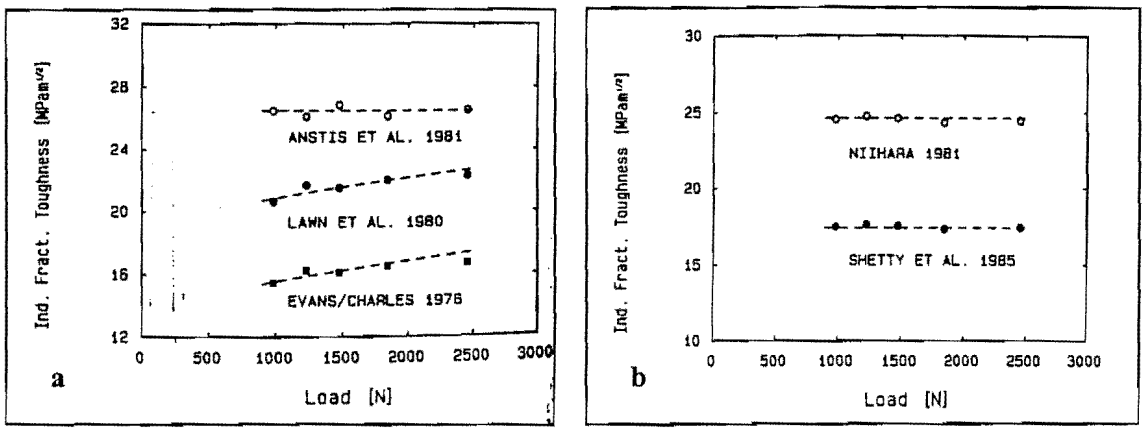

Figure 3.26: Indentation fracture toughness values for WC-Co alloy calculated with (a) median crack models, and (b) Palmqvist crack models [after ref. 90].

It therefore appears that the equations by Anstis *et al.* and Liang *et al.* are the best to use for estimating K_{Ic} through indentation.

3.3.5.2 Indentation strength in bending (ISB)

The indentation strength in bending (ISB) method for measuring fracture toughness, K_{Ic}, was first proposed by Chantikul *et al.* as a modified form of the controlled surface flaw (CSF) concept[105]. It has long been recognized that the chief source of discrepancy of K_{Ic} evaluated from strength equations, and that determined from more conventional specimens such as double cantilever beam, double torsion, etc has been the residual contact stress field associated with the radial crack system[105]. In strength methods such as the CSF technique, no attempts have been made to incorporate a residual stress intensity factor term into the strength / toughness formulation. Rather, experimental techniques such as annealing and removing the central deformation zone, which result in removing this residual stress, have been investigated. Chantikul *et al.* stated that this approach complicates test procedure and also runs the risk of altering the indentation flaw[105]. These investigators therefore developed the ISB method with a residual stress term introduced explicitly into the strength equations.

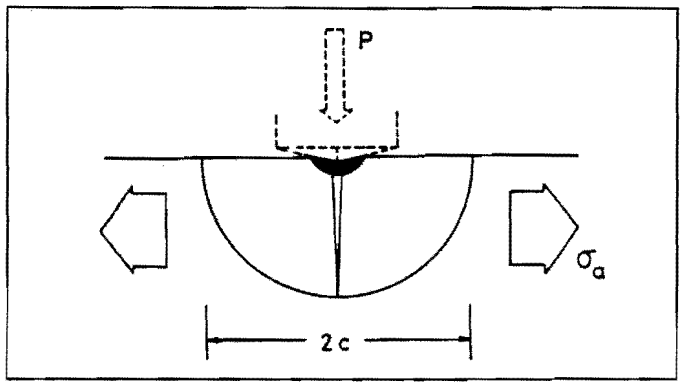

Figure 3.27: *Schematic of Vickers median-radial crack system, characteristic dimension, with contributions to tensile loading from applied field at stress σ_a and residual field (via central deformation zone) at (preceding) contact load P [after ref. 105].*

The ISB technique utilises a Vickers induced radial crack system as the primary surface flaw in the specimen (figure 3.27). The test involves subjecting this flaw to a tensile stress σ_a, which can be achieved through bending, i.e. by placing the flaw on the tensile surface of a bend specimen. For uniaxial loading, the indentation must be aligned with one set of pyramidal edges parallel to the tensile axis, while no such alignment is necessary for biaxial loading[105]. The tensile surface, of course, has to be ground flat and highly polished before indentation, to result in a clearly defined surface flaw. Prior to indentation, specimens should be annealed to relieve the grinding and polishing-induced surface compressive stresses.

The stress intensity factor appropriate to the tensile loading has the standard form:

$$K_a = \sigma_a(\pi\Omega c)^{1/2} \qquad \textbf{(3.23)}$$

where Ω is a shape factor with free-surface effects[1, 105].

However the residual contact stresses from the indentation radial crack system also contribute a stress intensity factor, given by[1, 105]:

$$K_r = \chi_r P / c^{3/2} = \S_V^R (E/H)^{1/2} (P/c^{3/2}) \qquad \textbf{(3.24)}$$

where $\chi_r = \S_V^R (E/H)^{1/2}$, which is a geometrical constant for Vickers-produced radial

cracks and *E/H* is the modulus-hardness ratio[105].

The total stress intensity factor of the indentation induced surface crack under tensile load is expressed by superimposing these stress intensities in a linear elastic system[1, 105]:

$$K_I = K_a + K_r \tag{3.25}$$

At the equilibrium condition for crack growth, $K_I = K_{Ic}$, equation 3.25 may be solved for the tensile stress, σ_a, as a function of crack size[1, 105]:

$$\sigma_a = [K_{Ic}/(\pi\Omega c)^{1/2}](1- \chi_r P/K_{Ic}c^{3/2}) \tag{3.26}$$

which has a maximum at,

$$\sigma_m = 3K_{Ic}/4(\pi\Omega c_m)^{1/2} \tag{3.27}$$

and, at a crack length of

$$c_m = (4\chi_r P/K_{Ic}) \tag{3.28}$$

Equations 3.26 – 3.28 indicate that the indentation crack undergoes stable growth in its initial stage of extension, but becomes unstable at $c = c_m$. The maximum stress σ_m now defines the as indented strength σ_f [1, 105].

Combining equations 3.27 and 3.28 results in a fracture toughness expression in terms of the tensile fracture strength σ_f and the indentation load P.

$$\begin{aligned} K_{Ic} &= [(4^4/3^3)\chi_r(\pi\Omega)^{3/2}]^{1/4}(\sigma_f P^{1/3})^{3/4} \\ &= \eta_r(E/H)^{n/4}(\sigma_f P^{1/3})^{3/4} \end{aligned} \tag{3.29}$$

where η_r is another geometrical constant.

If the geometrical constant η_r is known, then K_{Ic} may be determined easily from two readily measurable quantities, σ_f and P. Provided that the failure occurs at the indentation flaw, no crack length measurements are necessary to determine K_{Ic}. Chantikul *et al.* have empirically estimated η_r and n in equation 3.29 as $\eta_r = 0.59 \pm 0.12$ and $n = ½$ to result in the following expression used to calculate K_{Ic} [105]

$$K_{Ic} = 0.59(E / H)^{1/8}(\sigma_f P^{1/3})^{3/4} \qquad \textbf{3.30}$$

Scherrer *et al.*, used the above expression for K_{Ic} of dental porcelains, determined the hardness, H, at low loads of 1.96 N, at which no radial cracks were formed, so as to avoid an ambiguous meaning for the hardness[106].

Sakai *et al.* stipulated that the following conditions be satisfied in order for equations 3.29 and 3.30 to be sufficiently accurate for application to ceramics:

1. Test conditions 1, 4, and 5 for the IM method from Section 3.3.5.1 must be satisfied.

2. The test must show a linear relation between σ_f and $P^{-1/3}$. K_{Ic} can be determined from the slope of the σ_f versus $P^{-1/3}$ linear plot, which when extrapolated must pass through the origin. An example of a good σ_f versus $P^{-1/3}$ linear plot is shown in figure 3.28.

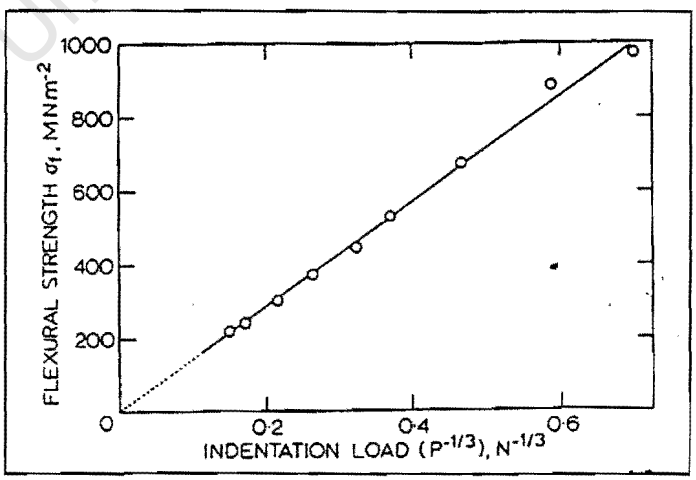

Figure 3.28: *Flexural strength σ_f vs. indentation load $P^{-1/3}$ for Si_3N_4 ceramic in ISB test; slope of straight line $[K_{Ic}/0.59(E/H)^{1/8}]$ is used to determine K_{Ic} [after ref. 1].*

Special attention is required if the indentation-induced crack has dimensions of the order of the ceramic microstructure or the strength controlling intrinsic flaws. In such cases log σ_f versus log P plots are used. An example of such a plot is shown in figure 3.29. In the higher indentation load region, the slope of 1/3 ensures applicability of equations 3.29 and 3.30 for calculating K_{Ic}. The relation however gradually deviates from the 1/3 power rule as the indentation load decreases, i.e. as the crack size decreases. This is due to the competition and the microfracture interaction between the indentation induced cracks and pre-existing strength controlling natural flaws as the failure origins.

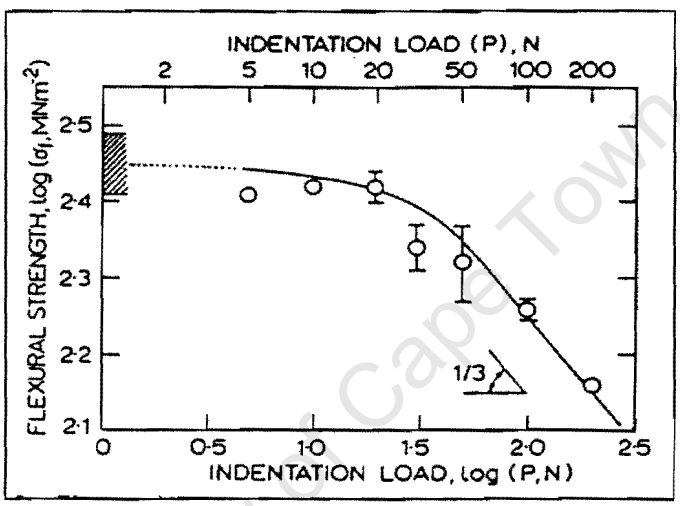

Figure 3.29: *Flexural strength σ_f and indentation load P relation for ISB test of Al_2O_3 ceramic; sizeable deviation from 1/3 power rule for median-radial crack system is demonstrated; hatching marks region of flexural strength controlled by natural intrinsic flaws [after ref. 1].*

3. Subcritical crack growth of ceramics by stress corrosion is an undesirable effect for fracture toughness testing. To minimise this effect, the use of dehydrated silicon oil is recommended during indentation as well as during the bend tests of the indented ceramics. The oil shields the indentation induced surface flaws from the moisture in the air.

Some advantages of the ISB technique are given below[105]:

- The technique attempts to take the residual stresses into account when calculating K_{Ic};

- Flaw size is eliminated as a variable in favour of indentation load. The need for accurate crack length measurements is thus avoided, an obvious and distinct benefit in any form of fracture testing;
- Relatively insensitive to slow crack growth effects;
- Departures from well-defined crack geometries due to microstructural or other complications do not pose the same limitations as in the IM method. In such cases the test provides a measure of the "effective" toughness, which may not be representative of K_{Ic} values obtained from macroscopic crack measurements in conventional fracture mechanics tests, but most probably reflects more closely the behaviour of the microscopic flaws which control the strengths of real ceramics.

A few disadvantages of this technique are[1, 105]:

- Test-piece economy – one specimen results in one data point as opposed to many data points being generated from one test piece in an IM test;
- The technique is still only semi-empirical. Although it attempts to account for the residual stresses from the deformed zone of the indentation into account, the technique still only leads to an estimate of K_{Ic}.

Appendix A summarises the test parameters used by previous researchers, as found in this review, for the IM and ISB techniques[33, 46, 57, 58, 97, 105 - 108].

3.4 Summary

Fracture toughness testing techniques, which were introduced in this chapter, are generally divided into two broad categories, viz. specimens with *macronotches*, and specimens with indentation induced *microcracks*. Test techniques from both these categories were reviewed in this chapter.

Four of the most common macronotch test techniques, viz. the SENB, DT, CVNB, and CVSR specimens were described. The SENB and chevron notched K_{Ic} tests have been standardised for metallic and carbide materials. In a chevron notched specimen, K_{Ic} can be determined without any information regarding the crack length. Chevron notched specimens can be tested in *bending*, as in the case of the CVNB specimen, or *pure tension*, as for the CVSR specimen. The DT test is used mainly for subcritical crack growth studies, but can also be used to estimate K_{Ic} at a particular crack velocity.

Three microflaw test techniques, viz. the CSF, IM, and ISB specimens were described. The CSF technique appears to be the best indentation technique to determine fracture toughness of brittle materials. Other indentation techniques, such as the IM and ISB test specimens, are semi-empirical and only lead to an estimate of K_{Ic}. These semi-empirical methods are particularly sensitive to uncertainties in the experiment and interpretation[32]:

- The subjective nature of estimating the location of the crack tip makes it difficult to measure the indentation crack length accurately. This leads to underestimates in the crack length measurements, and hence overestimates in K_{Ic}.

- The numerous alternative equations that have been published in the literature to derive K_{Ic} increase the level of uncertainty of the indentation microfracture techniques.

The IM, ISB, SENB-S, SEVNB, DT and CVNB test techniques were selected for experimental investigation in this project. Chapter 4 describes all the experimental details relevant to this project.

CHAPTER 4:

EXPERIMENTAL DETAILS

This chapter discusses all the experimental details undertaken in the project. The material selection process is described first, followed by details on the microstructural analysis and the ESH machine, which was used for the fracture toughness tests on the specimens with *macronotches*, followed by a section on the designs of the testing components. Specimen preparation in the form of machining, and the test techniques used in this project are described next, followed by a brief summary of this chapter.

4.1 Material selection

A material with similar hardness and fracture toughness to PCBN and PCD was required for investigation in this study. Since the hardness of these ultrahard materials is far superior to other materials, the ratio of hardness to toughness was taken as a comparative measure to find a similar material for testing. Table 4.1 summarises the mechanical property ranges (as found in the literature review of this study) of commercial ceramic composite materials, together with the defined H_v/K_{Ic} "index ratios".

Table 4.1: Mechanical properties of commercial ceramic composite materials.

Material family	H_v GPa		K_{Ic} MPa.m$^{1/2}$		Flexural Strength MPa		H_v/K_{Ic} Index Ratio m$^{-1/2}$		Within PCD / PCBN ranges?
	from	to	from	to	from	to	from	to	
PCD	35	50	3	8	-	-	4.38	16.67	-
PCBN	28	45	3	7	-	-	4.00	15.00	-
Al_2O_3	12	23	3	6	200	520	2.00	7.67	Yes
SiC	14	26	2.5	7.3	300	600	1.92	10.40	Yes
Si_3N_4	3	16	2	9	200	1200	0.33	8.00	Yes
PSZ	11	12.5	5	11	500	1300	1.00	2.50	No
Al_2O_3 - ZrO_2	9	15	4	15	-	-	0.60	3.75	No

The index ratios of the Al_2O_3, SiC, and Si_3N_4 families lie within the index ratio range of PCD and PCBN. Al_2O_3 was the most economical as well as the most easily available material from these three, and was therefore chosen as the test material for this study. Three grades of material with differing Al_2O_3 contents – 92 % (MP 92), 96% (MP 96) and 99 % (MP 99) - were obtained from Multotec Wear Linings in Pretoria, South Africa. Material properties (at room temperature, unless otherwise stated), and the approximate phase composition data, as quoted by Multotec Wear Linings (March 1998) for these materials are shown in Tables 4.2 and 4.3 respectively.

Table 4.2: Material properties of the Al_2O_3 materials obtained from Multotec.

PROPERTIES	UNITS	MP 92	MP 96	MP 99
Bulk density	g/cm^3	3.62	3.75	3.85
Porosity	%	Gas tight	Gas tight	Gas tight
Water absorption	%	0,0	0,0	0,0
Modulus of elasticity	GPa	295	330	340
Modulus of rupture	MPa	280	320	340
Fracture toughness	$MPam^{1/2}$	3,0	3,5	3,9
Vickers hardness	kg/mm^2 @ 5 kg load	1023	1277	1651
Abrasion resistance	cm^3/h	0,15	0,11	0,20
Thermal expansion	$10^{-6}/{}^0C$ at 400 ^0C	6,66	6,63	6,73
Thermal conductivity	W/(mK)	15	23	29
Thermal shock properties	-	Bad	Bad	Medium
Maximum temperature	^0C	1000	1000	1500
Sound velocity	m/s	9700	10220	10100

Table 4.3: Approximate phase composition of the alumina materials MP92, MP96, and MP99.

Phase	MP 92	MP 96	MP 99
Al_2O_3	92 %	96 %	99.7 %
SiO_2	3.6 %	1.8 %	-
CaO	2.6 %	1.3 %	-
MgO	1.8 %	0.9 %	0.5 %

4.2 Microstructural analysis

Two photos in different areas of a specimen of each material were taken in the scanning electron microscope (SEM). These were used to estimate the grain size of each material through the mean linear intercept method. Energy dispersive spectroscopy (EDS) was also conducted using the SEM to determine the phase composition of each material.

4.3 ESH universal testing machine

All the fracture toughness tests with *macronotch* specimens and the ISB tests were conducted using an ESH servo-hydraulic machine (figure 4.1). The machine comprises a hydraulic ram, which is mounted on the top platen, and controlled by a servo-valve with a feedback system. The ram can be controlled with respect to position (stroke control) or load (load control)[39].

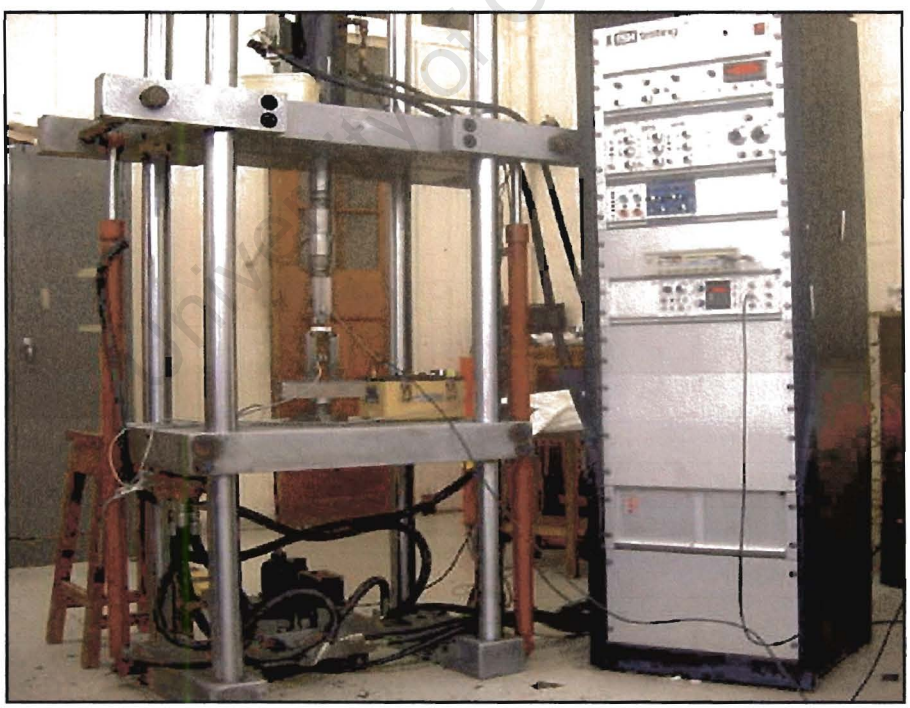

Figure 4.1: *Photograph of the ESH testing machine.*

The ESH had a maximum load capability of 50 kN, but a 10 kN load cell with ranges down to 2 kN was used for the present study (for all the tests except the DT tests,

since this load cell was damaged just before DT tests were done), since the fracture loads for the ceramic specimens would not exceed 10 kN, thus allowing for greater accuracy in measuring the peak fracture loads. Either the 2 kN or 10 kN load range was used depending on the expected fracture loads. A ramp generator that allowed the rate of change of position of the ram to be controlled was used for all the tests. A chart recorder linked to the ESH was used to plot the load-deflection, load-time, or load-stroke curves for the fracture toughness tests.

4.4 Component designs for testing

Components such as load spans and rollers were designed to fit the ESH machine for specific test/s where necessary. The SENB, CVNB, ISB, and DT tests all involve fracture testing in bending. The rollers were designed and manufactured to an 8 mm diameter in accordance with ASTM and British standards for fracture toughness testing in bending[21, 23].

For the SENB, CVNB, and ISB tests, an upper or inner load span S_2 of 20 mm separation was designed and manufactured. The bottom or outer load span S_1 (40 mm separation) consisted of rollers sitting on roller seats, which in turn were mounted on two metal columns. Figure 4.2 shows a photograph of the test set-up used for the SENB, CVNB, and ISB tests. For the DT testing, an upper or outer load span S_1 (40 mm) was designed and manufactured. The bottom load span S_2 (8 mm centre to centre separation) was from a previous project by Taylor[39], but needed slight modifications due to the different specimen sizes between the two projects.

Both the load spans designed employ the use of a needle roller bearing, the purpose of which, was to ensure that the rollers would always be in contact with the specimen surface during loading. The drawings for the load spans, rollers and other necessary components used during bend testing can be found in Appendix C.

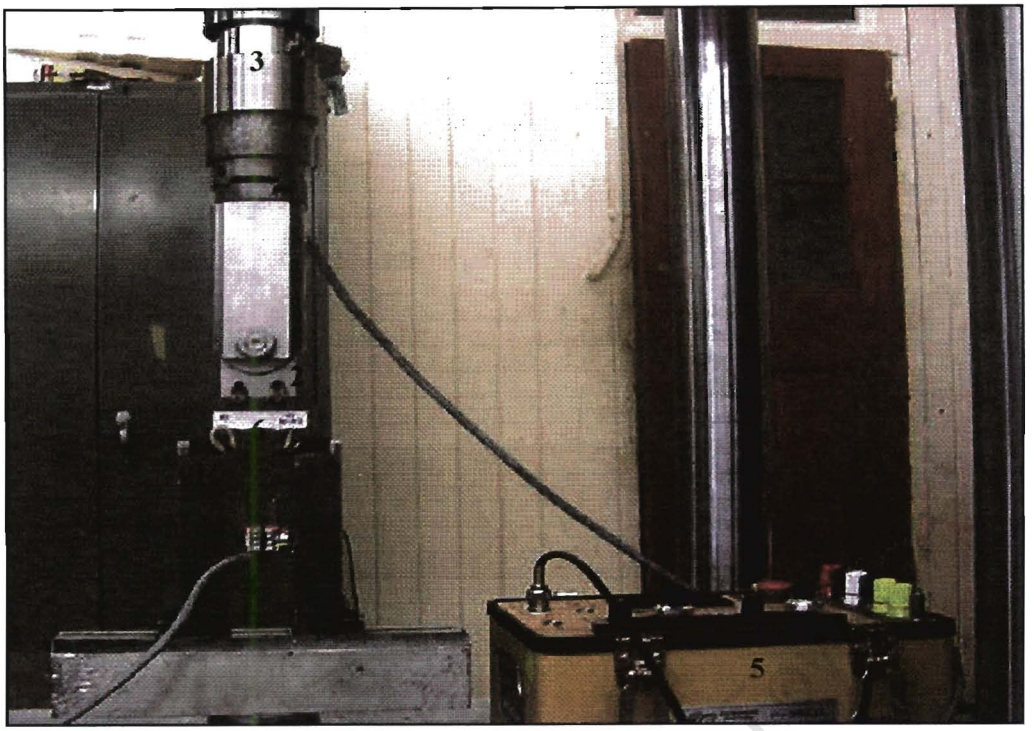

Figure 4.2: *Close-up photograph of test apparatus used for SENB, CVNB, and ISB tests – with components, 1. lower / outer load span with designed rollers and roller seats; 2. designed upper / inner load span; 3. 10 kN load cell; 4. clip gauge used to measure deflection/strain in the SENB and CVNB specimens; 5. strain gauge amplifier; and 6. test specimen.*

4.1 Machining of specimens for bend testing

The ISB, SENB-S, SEVNB, CVNB and DT fracture toughness test specimens all involve loading in 4-point bending. The test specimens have to be perfectly flat on all sides to satisfy theoretical and practical test considerations in ensuring a valid fracture toughness test. Bars of approximate dimensions 50 x 11 x 6 mm were supplied for the ISB, SENB-S, SEVNB, and CVNB tests; while tiles approximately 150 x 51 x 6 mm were received for the DT tests. The dimensions of the bars as well as the tiles were found to vary in addition to both the bars and tiles not being perfectly flat. Both had to be ground flat before any further preparation. Due to the varying sizes of the specimens, the final dimensions of the flat specimens also varied, as it would have taken too long to grind the alumina ceramic specimens of different sizes to a specific size, due to the high hardness of ceramics.

4.6 Fracture toughness testing of specimens with microflaws

4.6.1 IM tests

A 25 x 25 x 4 mm tile of each Al_2O_3 material was first cut into two halves and one half then mounted in a thermosetting resin. The mounted samples were ground flat using an automatic polishing machine. The samples were then polished using a 6 μm diamond lubricant for ~ 5 minutes, followed by further fine polishing with a 1 μm lubricant for ~ 3 – 4 minutes, and a diamond suspension for ~ 1 minute. After polishing, the samples were removed from the mounting resin and annealed in a furnace at $950 \pm 50\ ^0C$ for ~15 minutes, and furnace cooled, in an attempt to remove any compressive stresses induced during grinding and polishing.

All IM specimens were sputter coated prior to indentation to facilitate identification of cracks. A microhardness as well as a macrohardness tester was used to indent the specimens with a Vickers indenter. The maximum load on the microhardness tester was 1 kg (9.81 N) while the minimum load on the macrohardness tester was 20 kg (196.2 N). A load range of 10 – 300 N, as suggested by Sakai *et al.*[1] (Section 3.3.5.1) thus could not be used. Instead, at least 10 indents were made with both the 1 kg and 20 kg loads in each material. (A Knoop indenter was only available with the microhardness machine. Due to the maximum load only being 1 kg, CSF tests were not performed since the most commonly used loads for these tests were 2.5 and 5 kg)[95 - 97].

The indent diagonals and cracks induced by the Vickers indentations were measured in the SEM. K_{Ia} was calculated using the equations from Table 2, Section 3.3.5.1 by Anstis *et al.* (equation 2) and Liang *et al.* (equation 4).

4.6.2 ISB tests

After grinding flat, the test sides of the ISB bars (i.e. the 50 x 6 mm faces) were hand-polished using 3μm and 1μm diamond lubricants. Following polishing, the bars were annealed in a furnace at a temperature of $950 \pm 50\ ^0C$ for ~ 15 minutes and then

furnace cooled. This was done in an attempt to eliminate any grinding and polishing induced surface compressive stresses.

After annealing, a 20 kg load (or 196.2 N) Vickers indentation was approximately placed in the centre of the polished surface of each specimen. Ten to fifteen specimens of each material were tested in four-point bending at a constant ramp rate of 0.1 mm/min and test spans of 40 and 20 mm. All the bend tests were conducted on the ESH servo-hydraulic machine, with a 10 kN load cell, on the 10 kN load range. Plots of load vs. stroke (which is merely the displacement of the ram) were obtained with the chart recorder, and used to confirm linear elastic behaviour during loading. Fracture toughness K_{Ic} was estimated using equation 3.30, from Section 3.3.5.2. The specimens were examined under an optical microscope after the test to confirm that the fracture initiated at the Vickers indent. If it was found that the fracture did not initiate at the introduced Vickers indentation, the test was ignored with the data from the particular test excluded from the analysis.

4.7 Fracture toughness tests on specimens with macronotches

A 0.43 mm thick diamond saw blade was used to cut all the necessary notches for the respective fracture toughness tests on the specimens with *macronotches*.

4.7.1 SENB tests

Straight through notches were cut into all the SENB (both the SENB-S and SEVNB) specimens. Four specimens were notched at a time to a depth of 4.5 mm from the highest specimen, with the result of different notch depths in each specimen.

The SENB-S test merely involved fracturing these straight through notched specimens in 4-point bending. For the SEVNB tests, the straight through notches were sharpened with a razor blade and 15 μm diamond paste to increase the depth by at least 0.25 mm. After sharpening of the notches, the specimens were also fractured in 4-point bending.

The dimensions of each test piece were measured with vernier callipers, while the notch depths (and widths) were measured using an optical microscope at a magnification of 20x. All SENB tests were done with a constant ramp or loading rate of 0.1 mm/min, spans of 40 and 20 mm, and a 2 kN load range. A clip gauge was clipped onto the specimens via "knife-edges" that were glued onto the specimens to measure deflection. Load-deflection plots were obtained with the use of the chart recorder, and again used for confirmation of linear elastic behaviour during loading. The fracture loads were recorded, and used together with the dimensions and notch depths to calculate K_{Ic} from equations 3.3 and 3.4 in Section 3.2.1.

4.7.2 DT tests

After grinding flat, the DT specimens were notched at the centre of the 50 x 10 mm face (parallel to the 150 mm side), such that the thickness of the uncracked part of the specimen at the notch tip tapered from very thin to the full thickness, as shown in figure 4.3. The longer side of the notch was approximately 50 mm long, while the shorter portion was approximately 30 mm. This would facilitate the initiation of a sharp precrack in the specimen if the face of the specimen with the longest notch, corresponding to the full thickness, were placed on the compression side during testing as suggested by Tait *et al.*[60, 64]. Since the stress intensity K_I is inversely proportional to $t^{1/2}$ (equation 3.5), a reduction of the thickness by taper from full thickness to zero at the crack tip (on the tension side) results in very high stress intensities at first loading which facilitates the formation of a sharp crack at low loads. It is thus possible for the crack to initiate at loads well below those required to cause fracture of the full thickness[64].

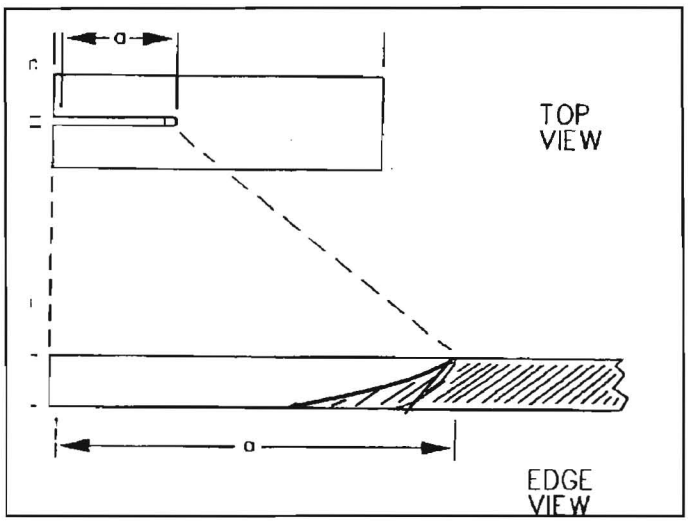

Figure 4.3: *Top view of DT specimen for fracture testing; including edge view of notch root detail [after ref. 64].*

The DT specimens were tested in 4-point loading at the front edge of the specimen using the apparatus shown in figure 4.4, with load spans of 40 and 8 mm. A 50 kN load cell (with a 10 kN load range) was used for the DT tests, since the 10 kN load cell was damaged during the set-up of the ESH machine for this test type.

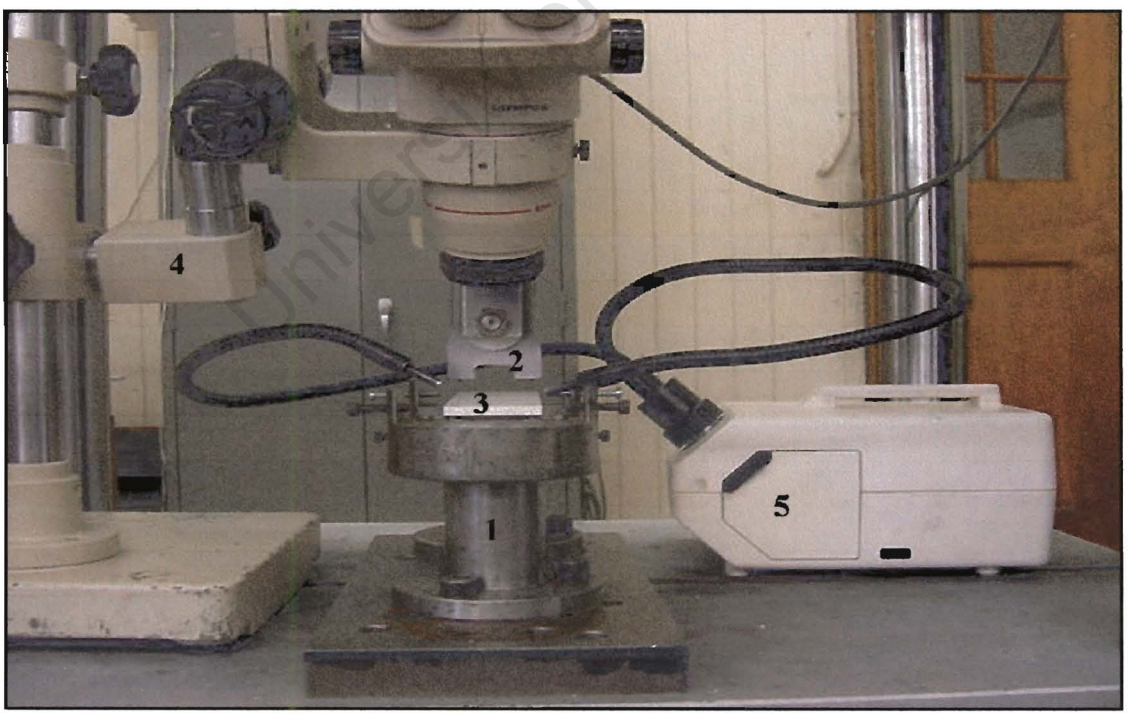

Figure 4.4: *Photograph of the DT testing apparatus, with components: (1) bottom load span used by Taylor[39]; (2) designed DT upper load span, and specimen (3) in the test fixture. The microscope (4) and light source (5) can be used to watch the crack growth.*

The dimensions and notch depths of each test piece were measured with vernier callipers. Load-time plots were captured with the use of the chart recorder, and used to read off the maximum and constant loads during the test. K_{Ic} is the right hand limit of the V-K_I curve. V-K_I curves, however, were not specifically generated during this project, since it would have involved varying the displacement rate, which would have consequently required very many specimens to obtain statistically representative values. Instead a constant displacement rate of 0.001 mm/second was used for all the tests. The fracture loads were recorded and used together with the dimensions and notch depths to estimate K_{Ic} from equations 3.14, 3.9 and 3.6 in Section 3.2.2. Equation 3.9 was used to analytically determine the derivative of the compliance. The compliance was not measured experimentally, since this would have required more specimens, and also since Kahraman *et al.* in any case stated that the difference between the experimental and theoretical values was less than 2 %[64, 65].

4.7.3 CVNB tests

Appendix D contains the drawing for the cutting of the chevron notch into the bend bars. Due to the different specimen sizes, the final dimensions of the CVNB specimens do not comply perfectly with this drawing, with the chevron slightly out of plane in some specimens. The dimensions of the chevron notch geometry of each specimen were therefore measured after the CVNB fracture toughness test on the fractured pieces using an optical microscope at a magnification of 20x. All the CVNB bars were fractured in 4-point bending at a loading rate of 0.1 mm/min, spans of 40 and 20 mm, and a 2 kN load range. The clip gauge and "knife-edges" were again used to measure deflection, and a load-deflection plot obtained for each test using the chart recorder to check for validity of the test, as described in Section 3.2.3. The peak loads were recorded and used with the specimen dimensions and chevron notch geometry to calculate K_{Ic} from equation 3.16 in Section 3.2.3.

4.8 Summary of Chapter 4

This chapter described how the experimental material was selected, and all the experimental techniques used in the project. The microstructural analysis was done with the aid of the SEM. The indentations were done on hardness testers, with crack lengths measured in the SEM. Components had to be designed for the testing of the specimens with the *macronotches* as well as the ISB specimens. Due to the long time it took to machine these specimens, they were only machined flat, resulting in varying specimen sizes. All the macronotch and ISB specimens were tested using the ESH machine. Chapter 5 contains the results, analysis, and discussion of all the experimental work presented in this chapter.

CHAPTER 5:

RESULTS, ANALYSIS and DISCUSSION

This chapter presents the results, analysis, and discussion of the experimental work undertaken in this project. The results for microstructural analysis, as well as for each fracture toughness test technique, are initially analysed and discussed in separate sections. All this is integrated in the analysis and discussion presented in Section 5.8, followed by a brief summary of this chapter.

5.1 Microstructural analysis

Grain size was determined with the aid of the SEM as described in Section 4.2. Table 5.1 lists the grain sizes of each material. Phase composition data for each material, which is the average result of two EDS scans from the SEM, is also included in Table 5.1

Table 5.1: Grain size and phase composition of each Al_2O_3 material.

Material	Grain Size	Phase Composition		
	microns	% Al_2O_3	% SiO_2	% CaO
MP 92	6.83	88.4	7.3	4.3
MP 96	6.55	94.1	3.7	2.2
MP 99	4.20	91.5	8.3	0.2

From Table 5.1 it appears that the grain size of the MP 92 and MP 96 materials were very similar, while the MP 99 material had a very much finer microstructure. The phase composition data show the Al_2O_3 contents to be lower than the so called "true" values of Table 4.3 provided by the supplier, and this was most probably due to the EDS scan being qualitative, but not quantitative. However, the EDS scans should give the correct trends between different materials, as done by Table 4.3, but this is

not the case in Table 5.1. This suggests that the so called MP 99 material might possibly in fact have a lower Al_2O_3 content than the MP 96 material, and a similar Al_2O_3 content to the MP 92 material. This could possibly be due to processing and fabrication errors in producing the material. Figure 5.1 shows the SEM micrographs used to determine the grain size of the MP 92, 96, and 99 materials respectively.

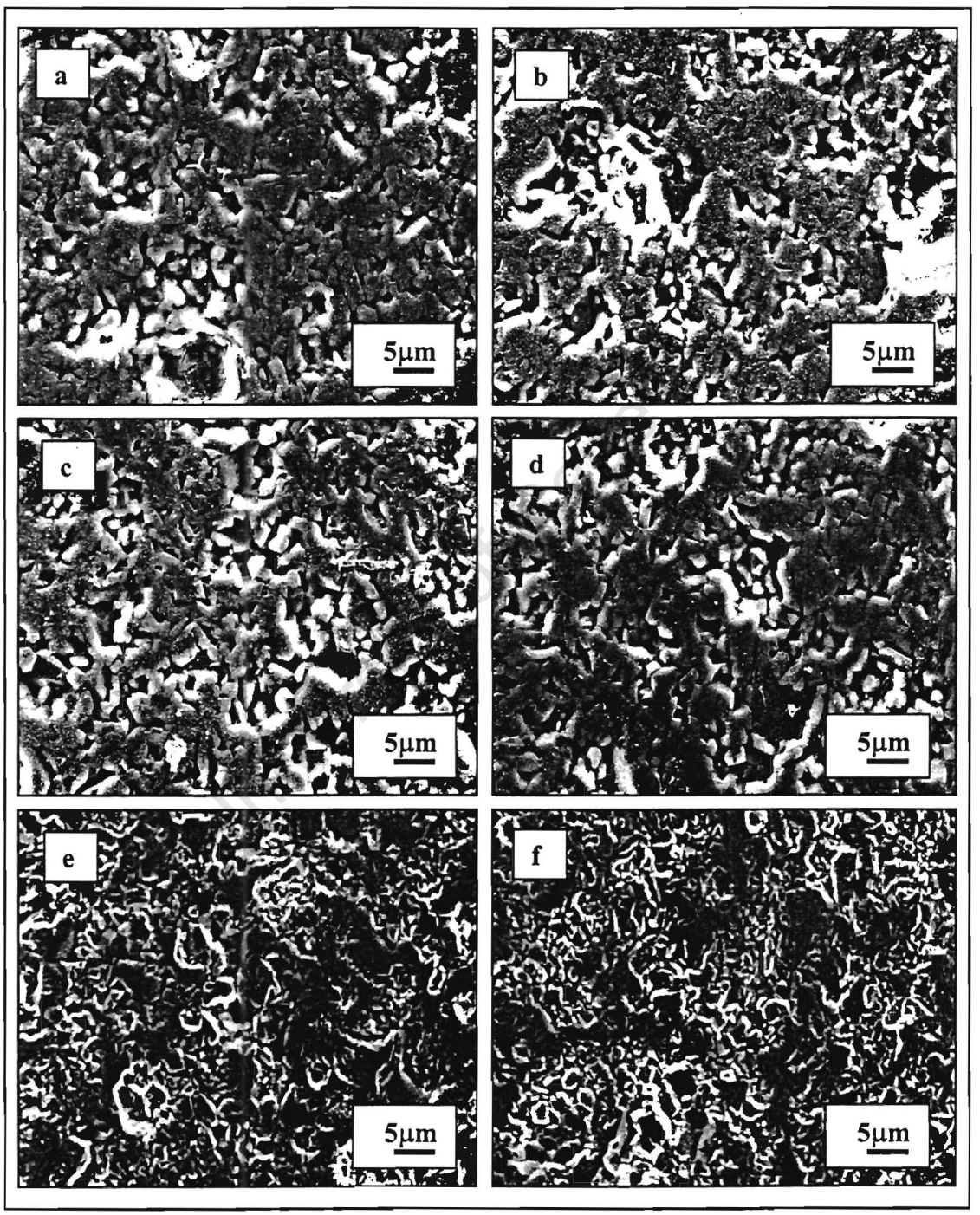

Figure 5.1: *SEM micrographs of the MP 92 (a, b); MP 96 (c, d); and MP 99 (e, f) alumina materials.*

The micrographs in figure 5.1 (a, b, c, d) suggest that the microstructure of the MP 96 material was finer than the MP 92 microstructure, and the figures calculated for grain size (shown in Table 5.1) using the mean linear intercept method could thus be misleading. Image analysis techniques (which were not available) should give more accurate values for grain size. The micrographs also show some porosity in *all* the materials. The porosity in each material was not quantified due to the lack of image analysis techniques.

5.2 Statistical analysis of data

All data is reported with the sample mean and the 95 % confidence intervals of the mean. The confidence intervals were calculated using the statistical *t*-distribution, and not the normal distribution, since the number of tests was always less than 30[29, 30]. Where necessary (as in the case of error bars overlapping), the statistical *F*- and *t*-tests were used to check for significant differences between different data sets[29, 109].

5.3 IM Test Results

Indents from the 1 kg load did not leave well-defined impressions in all the materials tested, as illustrated in figure 5.2. These indents were very difficult to see, even at magnifications of 4000x in the SEM. Cracking at the corners of the 1 kg indents did not always occur (figure 5.2 a). When cracking did occur, the cracks were very small and were difficult to distinguish from the microstructure (figure 5.2 b). It was hence very difficult to measure such cracks when they did occur, and errors in the short crack lengths would only lead to errors in estimating the fracture toughness of the material. This is similar to Sakai *et al's* findings on Palmqvist cracks in brittle materials (Section 3.3.5.1). As a result of these problems experienced with the 1 kg load indents, fracture toughness was not estimated for these indent-crack systems.

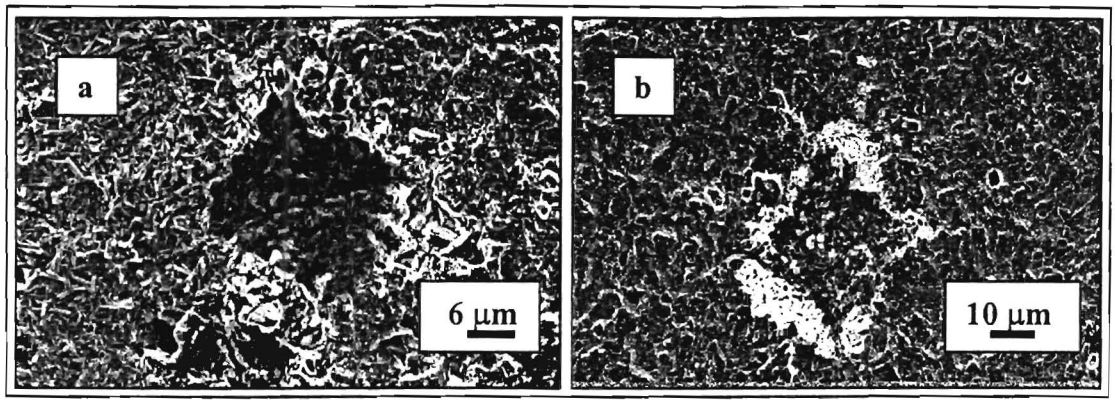

Figure 5.2: *SEM images of 1 kg load indents in (a) MP 92, and (b) MP 96.*

The 20 kg load indents were much better defined, with clear cracks emanating from the corners of the indent (figure 5.3). When there was severe multiple cracking, as in figure 5.3 a, the indent was ignored for measurements, since it would have resulted in an invalid fracture toughness (Section 3.3.5.1). An example of a good indent-crack system is shown in figure 5.3 b. Even in this "good" system there is some multiple cracking present as very short cracks not far off from the main cracks – these are indicated by the small black circles in figure 5.3 b. These indents could not be ignored since this was very common in most of the indents observed. The cracks thin off towards the end of their length making it difficult to distinguish the crack from the grain microstructure, thus introducing error into the crack length measurement, and consequently the indentation fracture toughness K_{Ia}.

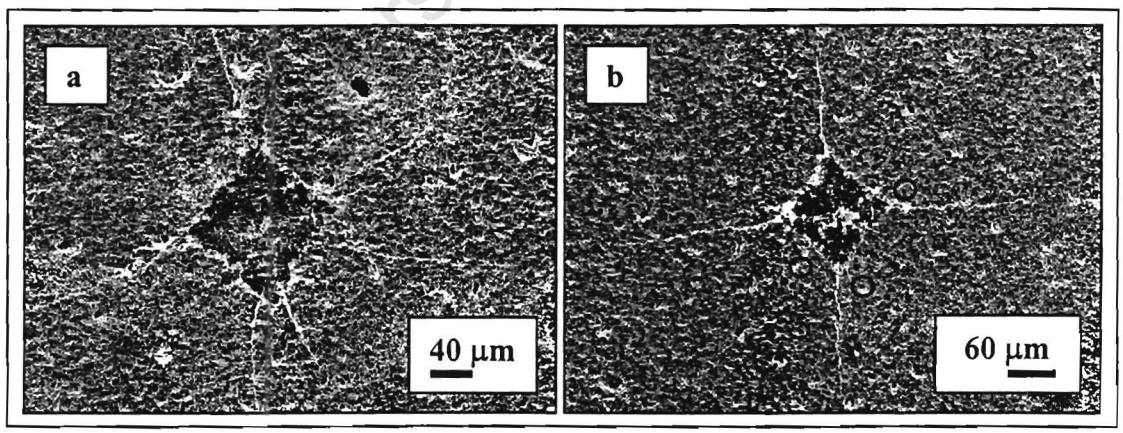

Figure 5.3: *SEM images of the 20 kg load indents in MP 96 – (a) severe multiple cracking, invalid test; (b) acceptable, valid test.*

Table 5.2 lists the *c/a* ratios and the 95 % confidence intervals for the indentation fracture toughness values calculated using the Anstis *et al.* and Liang *et al.* formulae from Section 3.3.5.1. The raw data is given in Appendix E. The specimens were not

broken after indentation testing to check whether the cracks were of Palmqvist or median-radial type. Instead the information from the literature was used to establish which crack system was present (Sections 3.3.3 and 3.3.5.1). From Table 5.2 it can be seen that the *c/a* ratio was greater than 2.5 for all the materials. The indentation load was 196.2 N, which was higher than the P_B load of 176 N reported by Liang *et al.* (Section 3.3.3). It can therefore be concluded that the cracks are of the median-radial type, which Sakai *et al.* stated to be the more applicable system for brittle materials.

Table 5.2: Indentation fracture toughness of the Al_2O_3 materials using the Anstis and Liang formulae.

Material	Number of tests	Average *c/a* Ratio	Anstis *et al.* K_{Ia}	Liang *et al.* K_{Ia}	Multotec quoted K_{Ic}
	n		**MPa.m$^{1/2}$**	**MPa.m$^{1/2}$**	**MPa.m$^{1/2}$**
MP 92	8	2.91	3.74 ± 0.42	3.96 ± 0.33	3.0
MP 96	6	2.75	4.27 ± 0.25	4.41 ± 0.20	3.5
MP 99	8	2.65	5.03 ± 0.54	5.29 ± 0.48	3.9

It can be seen from Table 5.2 that both formulae result in higher toughness values than the quoted Multotec toughness values. Both formulae, however give the same discrimination or ranking between materials. Figure 5.4 is a graph of the data from Table 5.2 plotted against the formula used to calculate K_{Ia}.

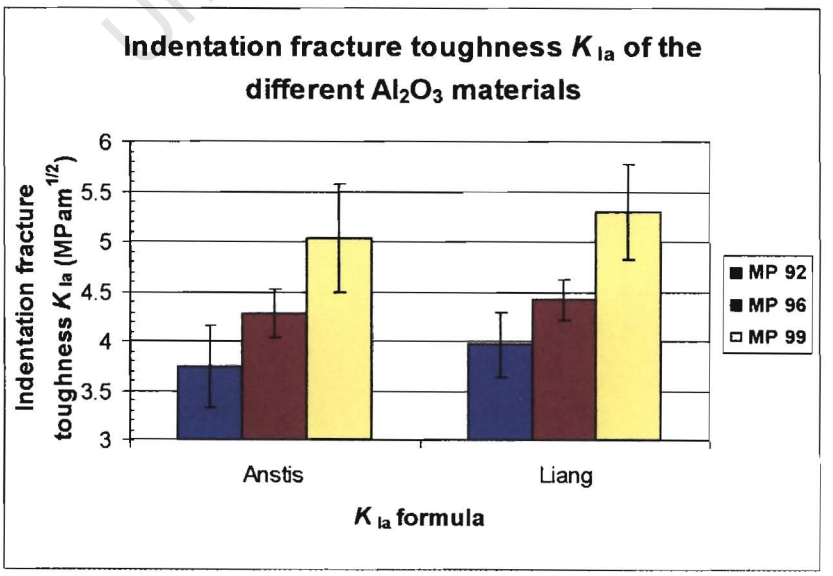

Figure 5.4: *Graph of K_{Ia} plotted against formula used to calculate K_{Ia}.*

Figure 5.4 is used to compare the K_{Ia} values for the different materials. Due to some overlap of the error bars for the different materials, the *F*- and *t*-tests were used to check for significant differences between the K_{Ia} values. These tests revealed that K_{Ia} of the MP 99 material is significantly higher than the MP 96 material, which in turn is significantly higher than the MP 92 material for both the Anstis *et al.* and Liang *et al.* formulae. The IM technique using these two different formulae therefore appears capable of distinguishing between different grades of Al_2O_3 material. The same data was re-plotted in figure 5.5 with the material grade name on the X-axis this time, to compare the differences, if any, between the two formulae.

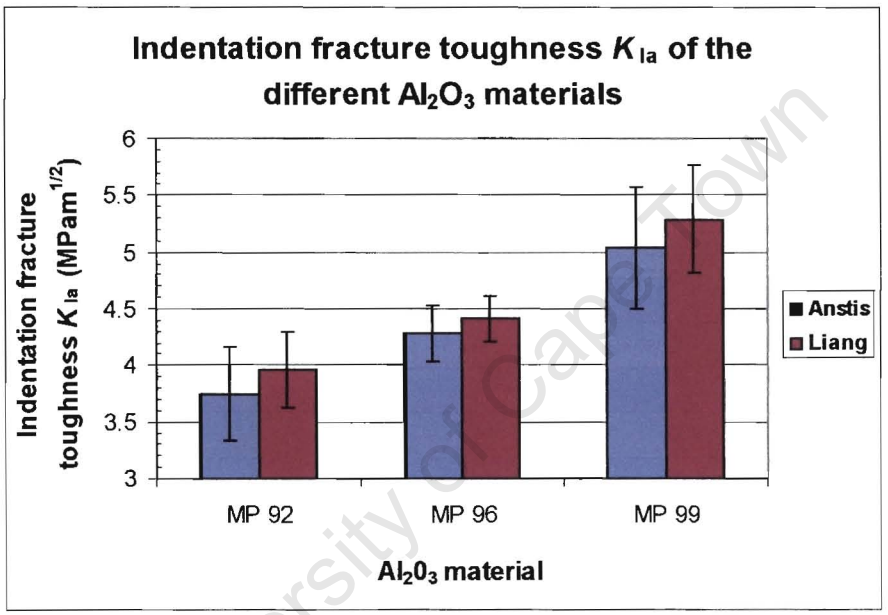

Figure 5.5: *Graph of K_{Ia} of the different grades of Al_2O_3 material for both formulae.*

It can be seen from figure 5.5 and Table 5.2 that the Anstis formula always gives lower average K_{Ia} values than the Liang formula, and is thus also closer to the "true" toughness, as quoted by the Multotec value. The upper and lower limits of the confidence intervals have similar deviations from the sample means for both formulae with the Liang formula giving slightly lower deviations, i.e. slightly smaller confidence intervals. The *F*- and *t*-tests were used again to check for significant differences between the results of the two formulae. These tests revealed no significant differences between the results of the two formulae for the all three alumina materials. These formulae are discussed further with respect to precision and discrimination in Section 5.8.

5.4 ISB Test Results

Due to the problems experienced with the 1 kg load indents in the IM tests (Section 5.3), only the 20 kg load indents were used for the ISB tests. Table 5.3 summarises the results of the ISB tests, which are plotted in figure 5.6. The raw data is given in Appendix F.

Table 5.3: Fracture toughness results of the ISB tests.

Material	Number of tests *n*	ISB K_{Ic} MPa.m$^{1/2}$	Multotec K_{Ic} MPa.m$^{1/2}$
MP 92	11	3.75 ± 0.09	3.0
MP 96	11	4.37 ± 0.07	3.5
MP 99	15	3.61 ± 0.05	3.9

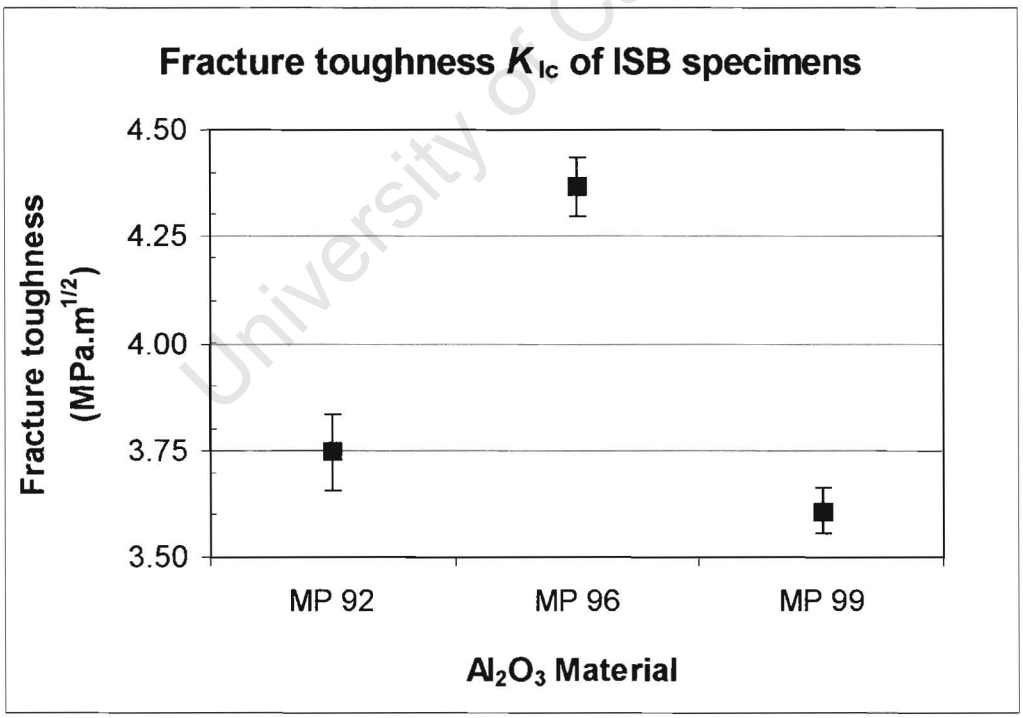

Figure 5.6: *Plot of the fracture toughness results using the ISB test.*

Table 5.3 indicates that the ISB fracture toughness was higher than the Multotec quoted values for the MP 92 and MP 96 materials, and lower for the MP 99 material. A possible reason for deviation from the Multotec values is the fact that the ISB test is

semi-empirical, only estimating K_{Ic}. The MP 99 material, which is supposed to be the toughest of the three materials, as quoted by Multotec, has a significantly lower toughness than the other two, while the MP 96 material is significantly tougher than the MP 92 material (figure 5.6). It is possible that the ISB test underestimates the toughness of the MP 99 material, thus leading to the incorrect ranking in toughness between these three materials. However, more tests were performed on the MP 99 material (15 compared to 11 for both the other materials), which showed the smallest scatter, as evident in figure 5.6. Taking the EDS phase composition data from Table 5.1 into account, it is also possible that the toughness of the MP 99 material was **in fact** lower than initially expected, due to the apparent lower Al_2O_3 content of the MP 99 material, which could be due to a poor quality batch of material.

5.5 SENB Test Results

Figure 5.7 shows typical examples of a SENB-S notched specimen (a), and a SEVNB specimen (b), which was merely a SENB-S specimen sharpened at the notch tip with a razor blade and diamond paste. These photographs clearly show the difference in the notch tip radii (which was defined as half the width of the notch slit in Section 3.1.2 iii) between the two specimens.

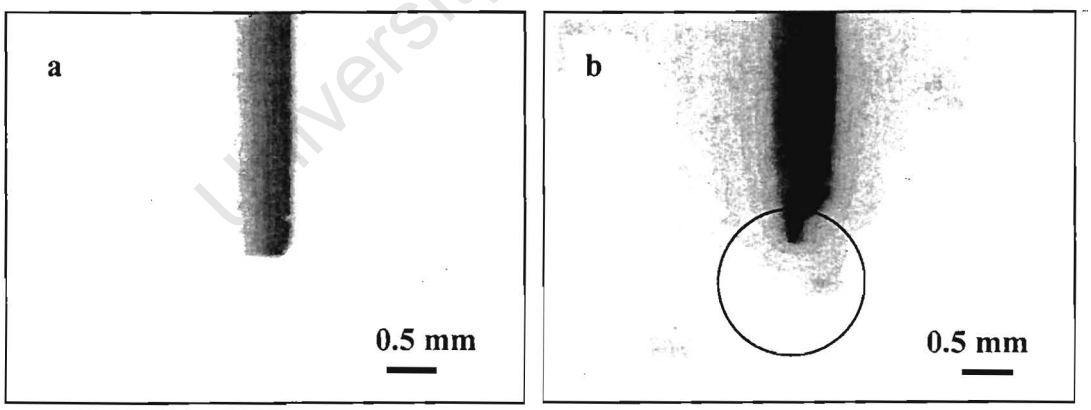

Figure 5.7: *Photographs (taken close to the notch tips) of (a) SENB-S specimen, and (b) SEVNB specimen.*

Photographs of typical fractured SENB-S specimens are shown in figure 5.8. In figure 5.8 (a) the specimen fractured from the left corner of the notch, while the fracture initiated from the right corner in (b) – the crack or fracture line is shown in the circles in the figures. The specimens were separated slightly, just before the

photographs were taken to emphasise the cracks, and therefore the notch widths also appear larger than they actually are. All SENB-S specimens fractured in this manner – i.e. nearer to one corner, and never from the centre since the stress concentration or intensity is always higher at corners or sharp edges.

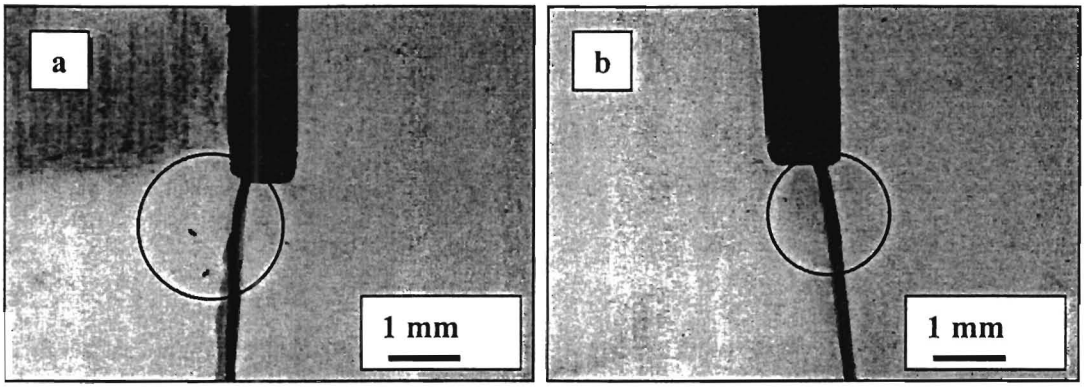

Figure 5.8: *Pictures of typical SENB-S fractures – (a) from left corner, (b) from right corner. The black circles show the cracks or the fracture line the specimen followed till fracture.*

Figure 5.9 shows photographs of typical fractured SEVNB specimens. Fracture initiated from the sharpened V-notch in all the SEVNB specimens, due to the smaller notch widths or tip radii resulting in higher stress intensities or concentrations at the sharpened tips. The resulting fracture was observed to be straight as in figure 5.9 (a), left as in (b), as well as right (not shown). This is again due to the smaller tip radii resulting in higher stress intensity factors, which could be anywhere within the notch tip diameter, as opposed to the SENB-S specimens where the stress intensity factors were always highest at, or close to one of the two sharp corners.

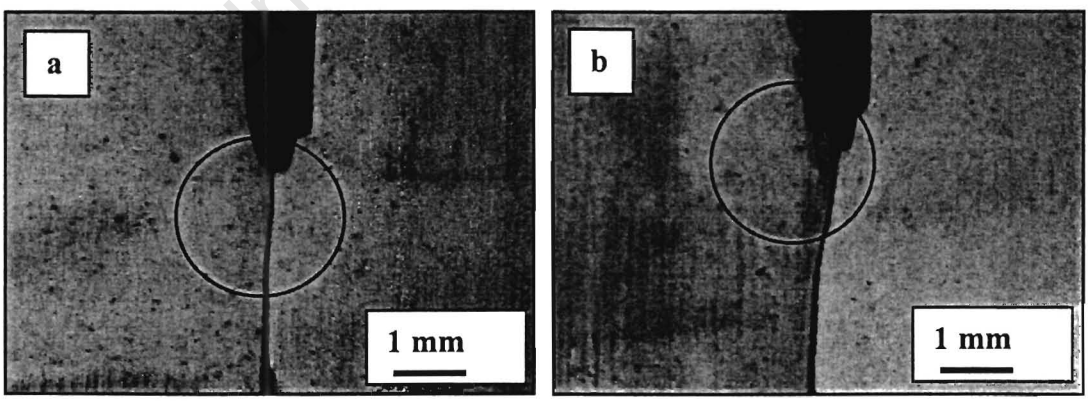

Figure 5.9: *Pictures of typical SEVNB fractures – (a) fractured with crack growing relatively straight down, (b) fractured from left side of sharpened notch tip with crack growing towards the left. The black circles show the cracks or the fracture line the specimen followed till fracture. Again, the broken pieces were slightly separated to enhance visualisation of the crack.*

The fracture toughness results for the SENB (i.e. SENB-S and SEVNB) tests are shown in Table 5.4 (symbols n, α, and ρ represent the number of tests, relative notch depth, and notch tip radius respectively). This data is plotted in figure 5.10 together with the Multotec quoted values, while the raw data can be found in Appendix G.

Table 5.4: Summary of SENB-S and SEVNB fracture toughness test results.

Material	SENB – S				SEVNB			
	n	α	ρ *mm*	K_{Ic} $MPa.m^{1/2}$	n	α	ρ *mm*	K_{Ic} $MPa.m^{1/2}$
MP 92	10	0.42	0.27	3.96 ± 0.13	10	0.45	0.15	3.15 ± 0.13
MP 96	12	0.42	0.25	4.90 ± 0.12	10	0.45	0.16	3.73 ± 0.07
MP 99	10	0.44	0.25	4.36 ± 0.25	10	0.45	0.19	3.74 ± 0.15

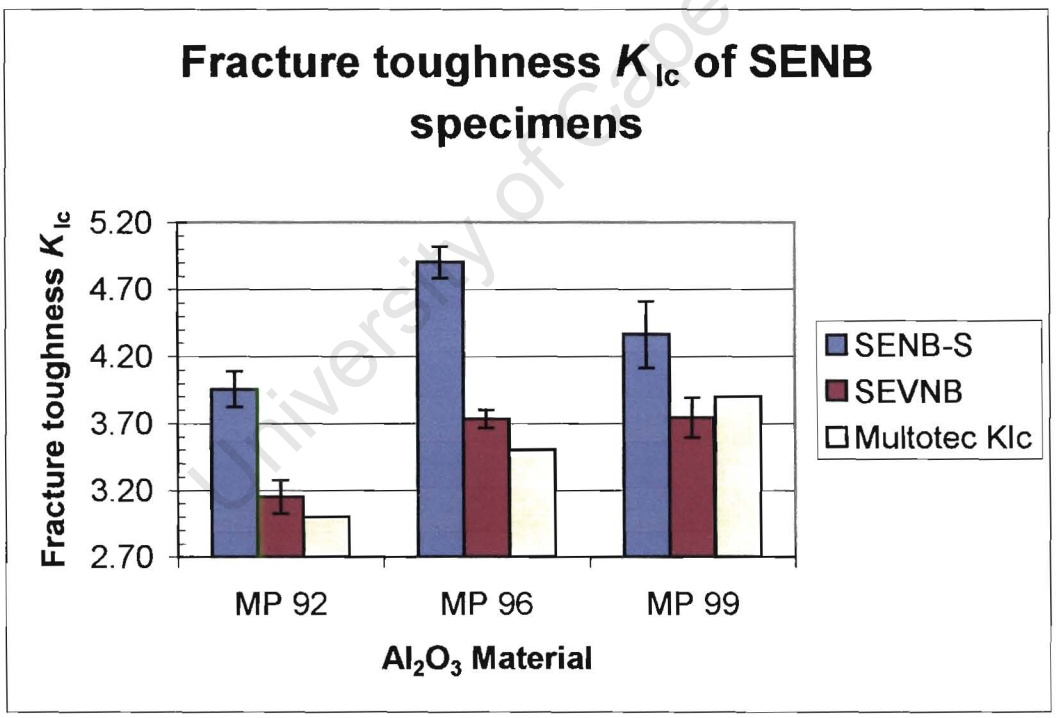

Figure 5.10: *Plot of fracture toughness values of each alumina material for both the SENB-S and SEVNB tests. The Multotec quoted values are also shown in the plot.*

The SENB-S values were significantly higher than the SEVNB results for all three materials, as expected, due to the smaller notch tip radii of the SEVNB specimens resulting in lower stress intensity factors to initiate and propagate fracture. The SENB-S results were also much higher than the Multotec quoted values. This is most

probably due to their larger notch tip radii, which results in larger stress intensity factors as discussed in Section 3.1.2 iii. This implies that the critical notch tip radius was smaller than 0.25 mm (which was the tip radius of the MP 96 and 99 materials – Table 5.4) for all the materials tested. However, the notch tip radii of the three materials tested in this study satisfied the criterion that notch widths be less than or equal to one tenth the specimen height (as recommended by ASTM E399 – 90, Section 3.2.1[21, 23]). This reinforces Sherman's work where he showed that a notch of 0.3 mm width (i.e. 0.15 mm tip radius) could cause a 30 % overestimate in K_{Ic} of ceramics[45].

The SEVNB results were closer to the Multotec quoted values, with the MP 92 and MP 96 values being higher, and the MP 99 lower, than the quoted value. From Table 5.4 it is seen that the lowest notch tip radius was 0.15 mm in the MP 92 material. The notch tip radius of the MP 99 was the highest since it was sharpened or "notched" last, with the result of the wearing cutting edge of the razor blade leading to blade bluntness and consequently the larger tip radius. However the 0.15 mm tip radius may yet still be too large as shown by Sherman (see above), implying further that the critical notch tip radius for all three materials was lower than 0.15 mm.

This may explain why the SEVNB test was apparently also overestimating K_{Ic} of the MP 92 and MP 96 materials. The MP 96 and 99 materials were both significantly tougher than the MP 92 material, but no significant difference was found between the MP 96 and 99 materials. Based on the Multotec values, the test appeared to be underestimating K_{Ic} of the MP 99 material (similar to the ISB test), thus resulting in the incorrect ranking between the materials. However, when considering the notch tip radii again (Table 5.4), the larger notch tip radius of the MP 99 compared to the other two materials, and the abovementioned suggestion that the critical notch tip radius was smaller than 0.15 mm for all three materials, it would appear that the test could only have been overestimating K_{Ic} of the MP 99 material. This means that the true fracture toughness of the MP 99 material would be even lower than the value given for the SEVNB test. It therefore seems possible that the MP 99 material did in fact have a lower toughness since both the ISB and SEVNB tests are showing this. The lower toughness could be due to processing and fabrication errors resulting in a poor quality material.

5.6 DT Test Results

It proved extremely difficult to grow a crack straight through the specimen during double torsion testing. Careful alignment of the specimen, as mentioned by previous researchers, is difficult but nonetheless critical to steering the crack straight through the specimen[39, 60]. The specimens were very carefully aligned centrally in the test fixture with a vernier to ensure that the moment arms were equal on both sides of the crack, and thus attempt to prevent cracks from growing skew. Any slight misalignment (which is very possible since the *hand aligned* specimen was not clamped tightly in place, and the dimensions involved in alignment were very small) could result in skew cracks.

In addition to alignment, loading the specimen with the shorter side of the notch in tension did not work as expected and discussed in Section 4.7.2. The first few specimens were tested with the shorter notch on the tension side, for which every specimen did not result in the crack growing straight through to the other end. These specimens did not even crack along the full taper (which was not expected – Section 4.7.2), with the resultant crack not reaching the tip of the longer side of the notch. Instead catastrophic fracture occurred towards the sides of the specimen within the first third or just upon entering the second third of the specimen (figure 5.11). An attempt to explain this behaviour is made after presenting figure 5.17. Since the DT test is a constant K test method, and constant K is only achieved around the middle third region, all data from such tests may be questionable (in terms of DT analysis) and were thus invalid.

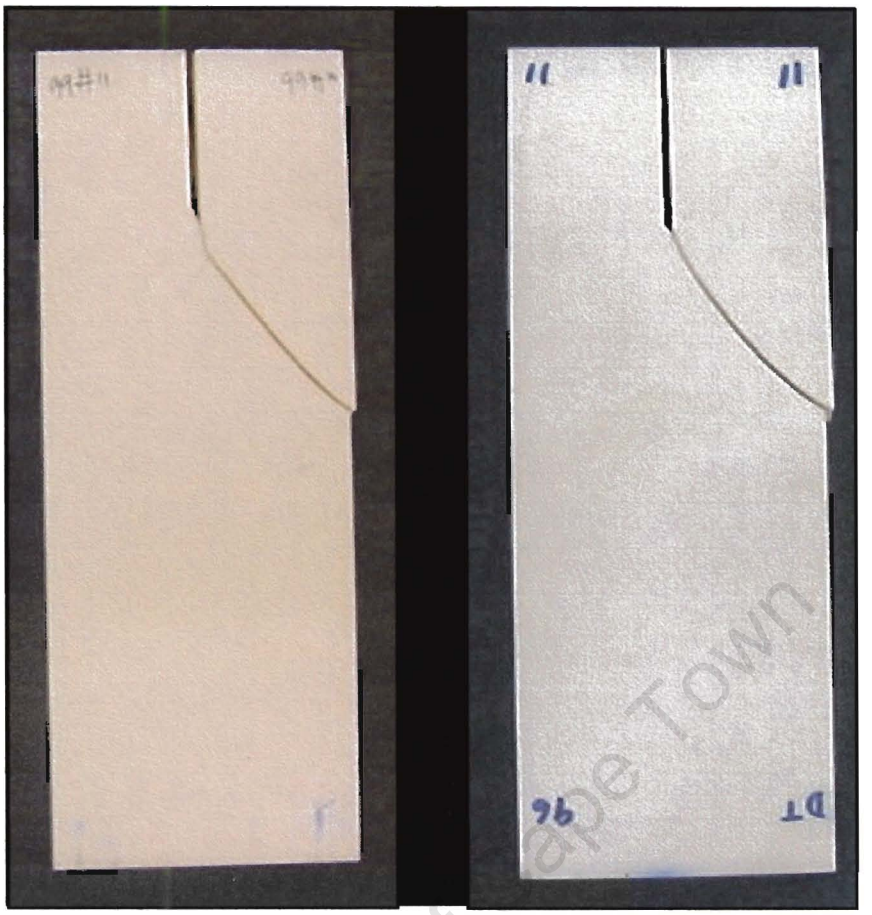

Figure 5.11: *Pictures of typical fractured specimens tested with the shorter notch depth in tension.*

Due to the limited number of specimens, and catastrophic fracture always resulting from the specimens with the shorter notches in tension, it was decided to attempt the test with the longer side of the notch in tension. These tests appeared better from the start with the crack at least growing into the last third of the specimen. It was therefore decided to continue the test with the longer notch in tension to eliminate the wasting of specimens.

The resultant fractures from testing the DT specimen with the longer notch in tension could be grouped into three types, shown in figures 5.12 and 5.13, as opposed to the one type for testing with the shorter notch in tension, shown in figure 5.11:

i. *Crack growing straight through the specimen.* This is the "perfect" or ideal case and was more common than ii but not as common as iii. Typical examples of these are shown in figure 5.12 and figure 5.13 (c) & (f). In figure

5.13 (c) and (f), the cracks deviate slightly to the left and right respectively, while the cracks appear to grow straighter in figure 5.12.

ii. *Crack growing towards the left side of the specimen.* This was the least common type and typical examples of these are shown in figure 5.13 (a) & (b). The specimen shown in figure 5.13 (a) was in fact the only specimen of all that were tested to exit the left side without reaching the other end of the specimen.

iii. *Crack growing towards the right side of the specimen.* This was the most common type and typical examples of these are shown in figure 5.13 (c) & (d).

Figure 5.12: *Pictures of two of the best resultant fractures from the DT test with the longer notch in tension.*

Figure 5.13: *Pictures of typical types of resulting fracture from the DT test with the longer notch in tension. The pictures on the top show the crack deviating to the left of the specimen while those on the bottom show deviation to the right. (c) and (f) deviate slightly to the left and right respectively, but are still very good examples of straight cracks, which are not easily achieved in practice.*

It was observed that the probability of the crack growing straight through the specimen was higher when the crack initiated at the left corner of the notch. All cracks that initiated at the left corner either grew straight, or deviated either to the left or right, but at least grew far into the last third of the specimen length (figures 5.12 & 5.13 d & e). Cracks that initiated at the right corner only exited through the right side of the specimen, sometimes not even growing through to the middle third of the specimen (figures 5.11 & 5.13). This bias towards the right side of the specimen suggests that there might be a slightly higher torque being applied to the right torsion bar, which could be due to the system, since alignment is set in a consistent manner (same operator using the same judgement the entire time). This means that there is a probability that the load points (both top and bottom) were not perfectly symmetrical. It must be mentioned, though, that these were in fact checked before starting any of the DT tests but the actual misalignment is most probably too small or sensitive to be detected by a vernier. An accurate alignment system such as an XY stage and a good clamping device should make the task of alignment and consequently straight crack growth easier.

Even though straight crack growth was achieved, not all the specimens displayed this, as evident from figures 5.11, 5.13 (a), (b), (d), (e). If the data from only the straight crack specimens were used, there would have been too few data points resulting in large scatter bands or confidence intervals. Many of the specimens with fractures that went out the sides still showed approximately straight cracks in the middle third region of the specimen, which is the major region of interest in DT testing. Data from these specimens could therefore also be used, and more data would certainly improve the scatter or confidence intervals. However, a limit had to be set, so that cracks that deviated too much from the centre were not included in the analysis. The distance, b, of the crack or fracture from the remote edge of the specimen (illustrated in figure 5.14) was measured for all the specimens, and set to 0 (zero) mm for those that cracked straight through. For validity of data, and thus to be included in the analysis, the crack should at least enter the last third region of the specimen, i.e. $b < 50$ mm. Furthermore a limit of $b < 30$ mm was set to avoid very skew cracks from entering the analysis.

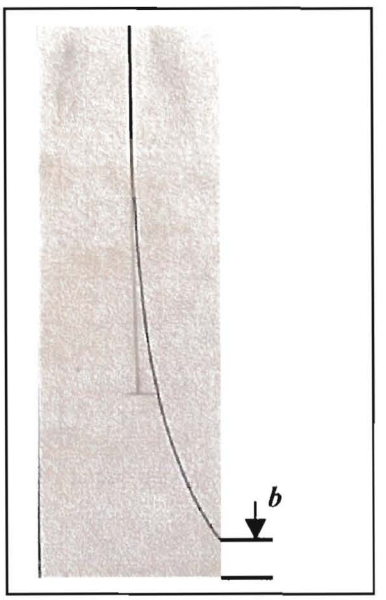

Figure 5.14: *Definition of edge distance b to crack exit.*

Typical load-time curves for testing with the short notch in tension and the long notch in tension are shown in figures 5.15 and 5.16 respectively.

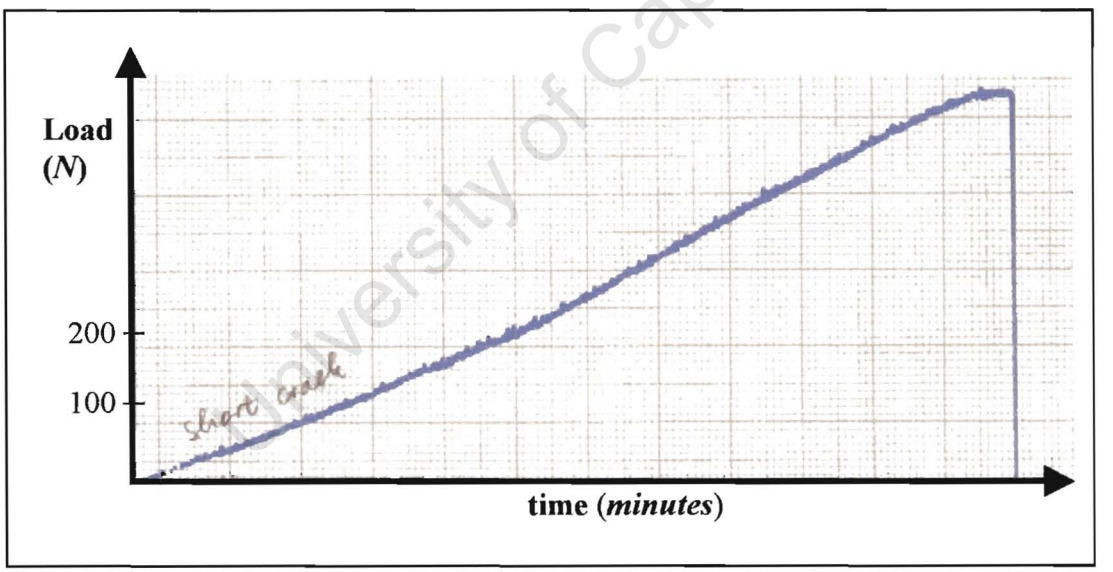

Figure 5.15: *Representative load-time curve obtained when loading the DT specimen with the short notch in tension. The time was not measured absolutely, but was of the order of minutes (under 10 minutes).*

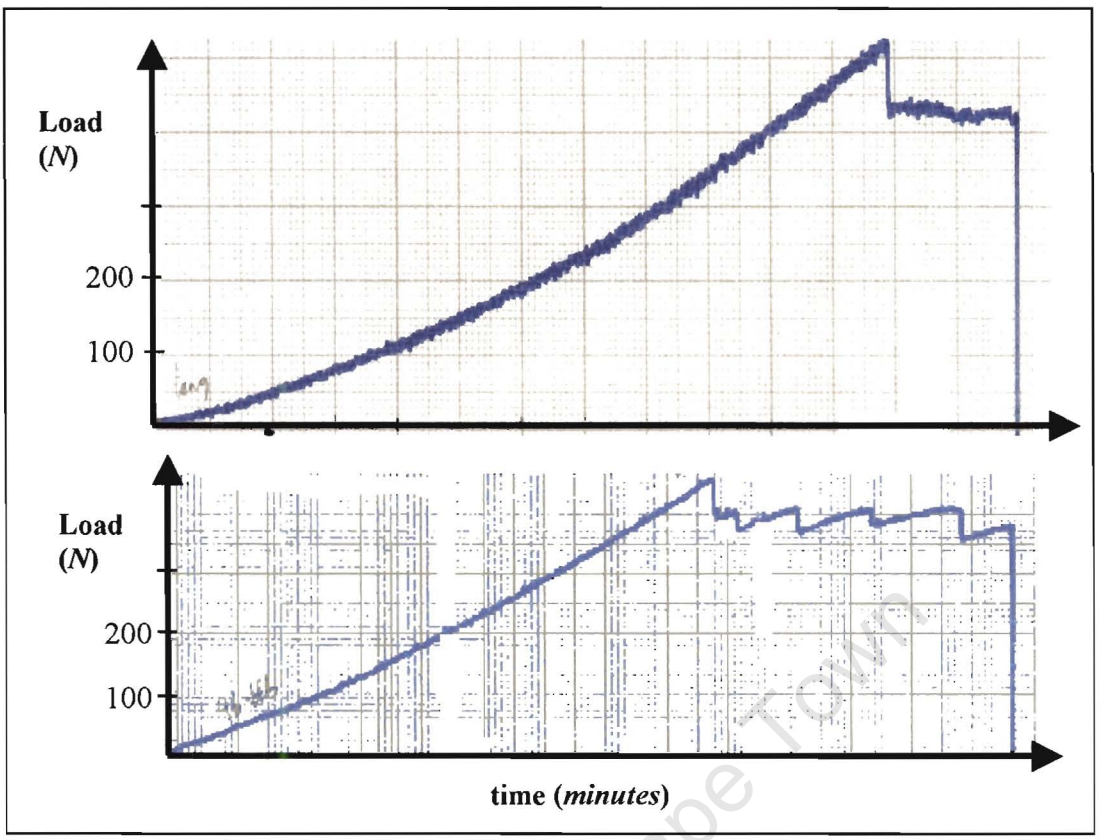

Figure 5.16: *Typical load-time curves obtained when loading the DT specimen with the long notch in tension. Again the time was not measured absolutely, but was of the order of minutes (under 10 minutes).*

The reason for the difference in the curves of figures 5.15 and 5.16 lies in the difference in crack initiation between the two testing configurations:

1. *Short notch in tension (figure 5.15)*

   A sharp precrack is initiated at very low loads as discussed earlier in Section 4.7.2. The load continues to increase steadily until it reaches a *constant maximum* value (in the constant K_I region), with the crack continuing to grow subcritically during all this after growing very far into the specimen, after which, it becomes unstable due to edge effects. However in the present study, the cracks resulting from testing the shorter notches in tension did not grow very far into the specimen, but rather exited through the sides of the specimens as already stated.

2. *Long notch in tension (figure 5.16)*

There were two distinct types of load-time curves for this testing configuration as shown in figure 5.16 (a) & (b). Figure 5.16 (a) shows a well defined approximately constant load while (b) shows a sawtooth pattern due to the crack growing incrementally. The sawtooth heights were fairly consistent and not very large (~40 N) in comparison with the maximum loads (~500 – 600 N), and therefore a constant load could be assumed over the region, thus assuming (a) & (b) to be equivalent load-time plots (figure 5.16).

The load increases steadily until it reaches a *maximum* value, at which a sharp crack is initiated from the blunt long notch. After crack initiation, the load drops, and maintains an approximately constant value (in the constant K_I region), during which crack propagation continues subcritically until the crack has grown a long distance and edge effects of the specimen result in catastrophic fracture. If the notch were very sharp, then the maximum and constant loads would be identical, since a blunt notch requires a higher apparent critical stress intensity to cause fracture (figure 3.1).

Figure 5.17 shows a graph of maximum load, P_{max}, versus edge distance b, as defined in figure 5.14, for all the DT tests. Figure 5.17 can be used to explain why the specimens tested with the shorter notches in tension result in catastrophic fracture towards the side of the specimens. It must be remembered that it was initially decided to test the specimens in this configuration to allow for easy development of a precrack, as discussed in Section 4.7.2. Due to high stress intensities as a result of the reduced thickness, a precrack did in fact initiate, as can be seen at the notch tips of the specimens in figure 5.11. The resulting crack, however, did not grow along the full taper length, which was unexpected. The precrack requires increasing load to grow stably, since the crack area is increasing and the stress intensity is decreasing, both due to increasing thickness. Subcritical crack propagation continues with increasing load, until the maximum load is reached. After reaching the maximum load, it does not take long for catastrophic fracture to occur, which can be seen from the very small time at the maximum constant load on the load-time curve of figure 5.15.

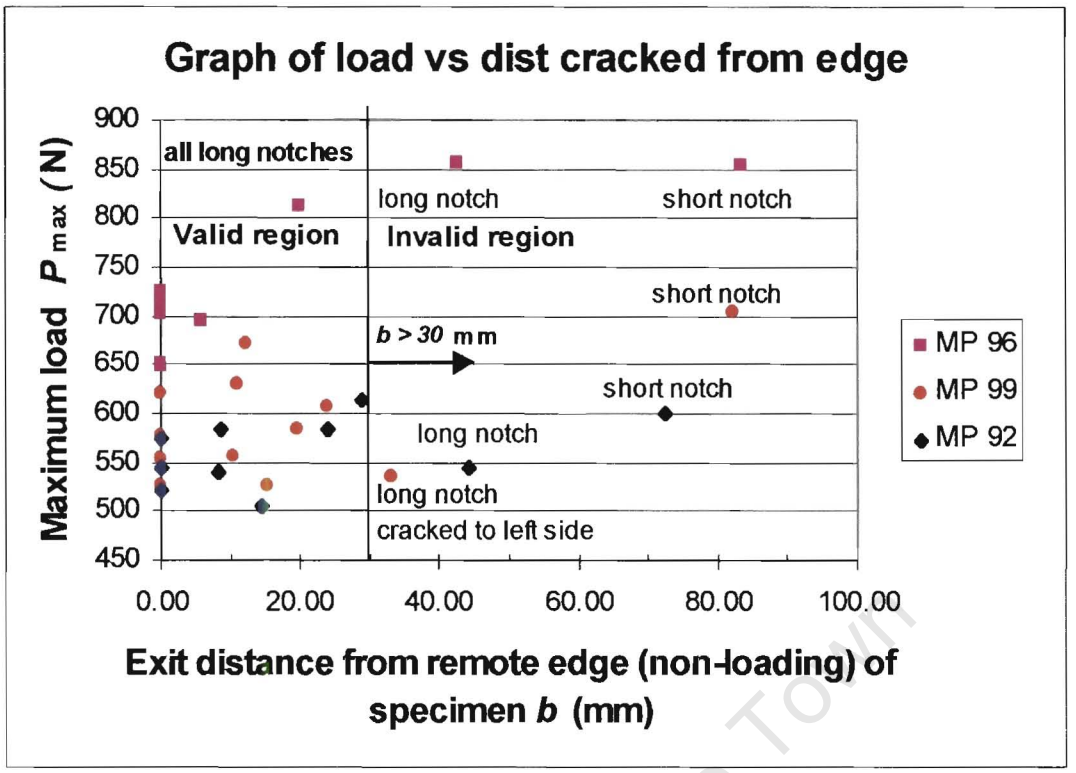

Figure 5.17: *Graph of maximum load versus the distance cracked from the remote edge of the specimen.*

From an inspection of figure 5.17, it can be seen that the loads for the specimens with the short notches are actually higher than the average loads of the specimens with the long notches for all three materials. The loads for the specimens with the long notches are the loads at which the crack is initiated from the blunt notch. These loads thereafter drop to a constant value, which results in the constant K_I region. This implies that the load has increased above the particular constant maximum load in the constant K_I region. It appears that the specimen with the short notch requires more energy just to precrack fully along the taper than that required for the specimen with the long notch to fracture fully. So it can be deduced that the load increases beyond this particular value until it reaches a maximum that results in a critical stress intensity (which is higher than in the constant K_I region since the thickness is still smaller than the full thickness), which in turn leads to an unstable crack and consequent catastrophic fracture. All of this suggests that the taper length was too long resulting in very high stress intensities well before the full length was cracked. Unfortunately, the taper length was not considered before notching. The taper length was approximately 20 mm long (since long notch = ~ 50mm, and short notch = ~ 30 mm), and was a result of the cutting blade radius. Making the taper length smaller would

result in the full thickness being cracked at much lower loads than have been experienced in this study, and thus reducing the energy needed to propagate the crack along the full thickness. Once a precrack has developed along the full thickness, the load will continue to increase until it reaches a constant maximum value in the constant K_I region.

For DT testing, fracture toughness K_{Ic} is defined as the right hand limit of the V-K_I curve. However since V-K_I curves were not specifically generated in this project, K_{Ic} was estimated using the maximum loads (since the crack was actually initiated at these loads for the specimens with the longer notches in tension, which are in fact the only valid data) and equation 3.14. Since this is only an estimate of K_{Ic}, the symbol $K_{Ic,\,est.}$ will be used, and their values are likely to be a lower bound K_{Ic} value, probably less than the "true" toughness. The DT test results are presented in Table 5.5 and shown graphically in figure 5.18. The raw data is given in Appendix H.

Table 5.5: Estimated fracture toughness $K_{Ic,\,est.}$ values from the DT tests.

Material	**No. of valid tests** n	**DT** $K_{Ic,\,est.}$ **MPam$^{1/2}$**	**Multotec** K_{Ic} **MPam$^{1/2}$**
MP 92	8	2.63 ± 0.13	3.0
MP 96	8	3.51 ± 0.15	3.5
MP 99	10	3.07 ± 0.07	3.9

With the exception of the MP 96 material, $K_{Ic,\,est.}$ did not agree well with the Multotec quoted values of K_{Ic}, as indicated in Table 5.5. This is probably due to the DT test only giving an estimate of fracture toughness. The agreement in values for the MP 96 material, however, might be suggesting that the Multotec value may, in fact, be inaccurate. From figure 5.18, it is noticed that $K_{Ic,\,est.}$ of MP 96 was significantly higher than that of MP 99, which in turn was significantly higher than that of MP 92. This trend is consistent with the findings of the SENB tests. *It therefore appears that the MP 99 material was less tough than the MP 96 material.*

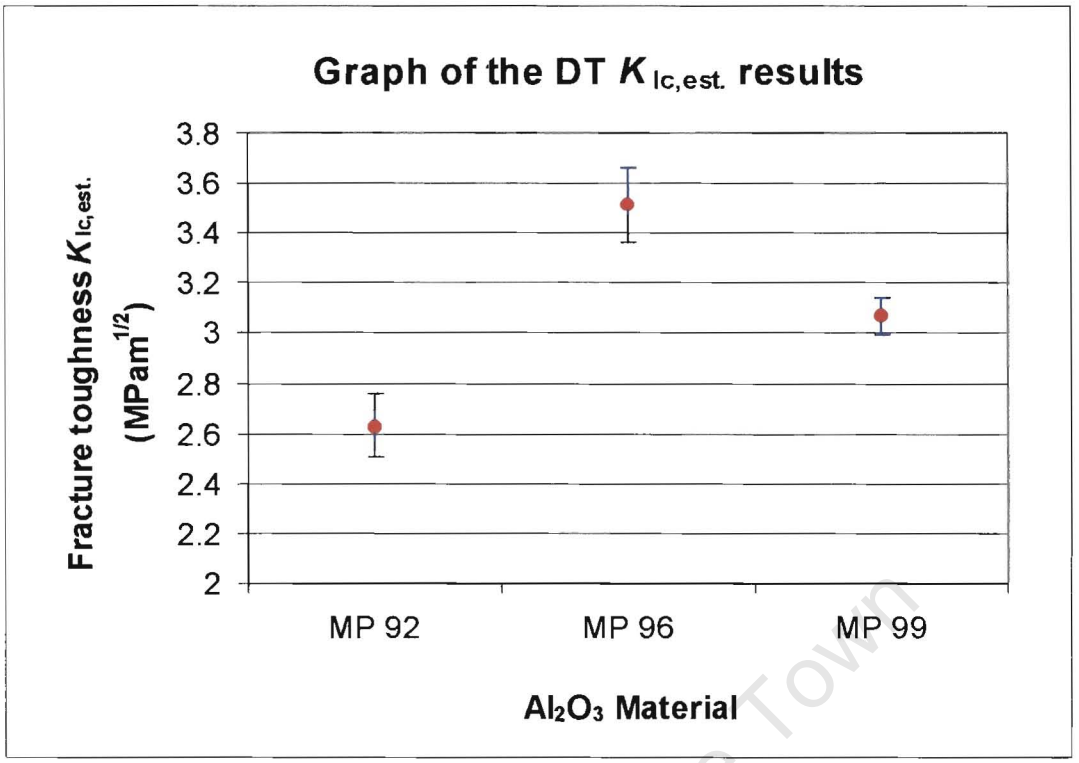

Figure 5.18: *Plot of the estimated fracture toughness results using the DT test.*

5.7 CVNB Test Results

The load-deflection plots are necessary to ensure the validity of the CVNB tests (Section 3.2.3). Examples of typical load-deflection plots obtained for the CVNB tests in this project are shown in figure 5.19. These plots were not ideal (when compared to figure 3.7 in Section 3.2.3), since the deflection scale needed to be larger (or more sensitive) to indicate stable crack growth. This was due to the chart recorder that was used not being sensitive enough to record smaller displacements – it was used at the highest level of sensitivity.

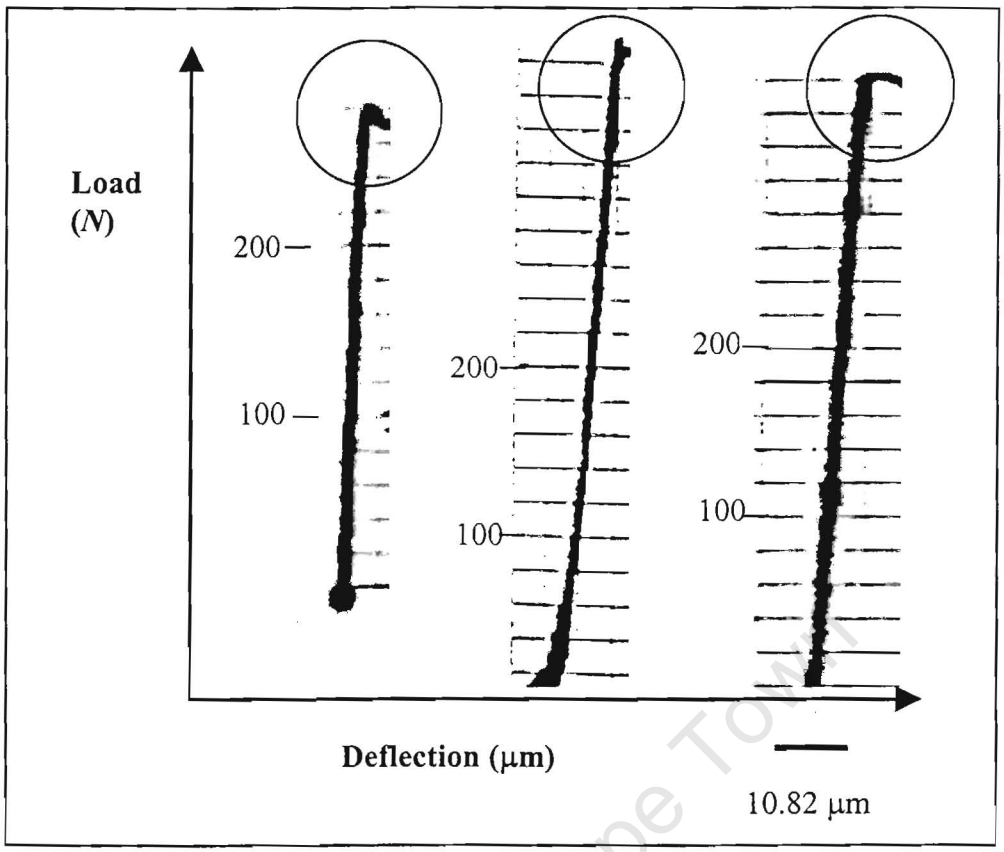

Figure 5.19: *Typical load displacement plots for the CVNB specimens.*

The plots did show some sort of non-linear behaviour (as indicated by the black circles in figure 5.19) just before fracture, which could suggest stable crack growth. However there was no certainty of stable crack growth, due to the plots not being sensitive enough in the deflection axis. The stored strain energy of the testing machine compliance system would also contribute to this. A much stiffer machine system would be needed to overcome this difficulty. The CVNB test is only valid for stable crack growth. As a result of this, there is uncertainty in the validity of the CVNB data obtained in this project. The results are presented next with the assumption that stable crack growth did occur, and that the tests are therefore valid, even though there is limited proof of this. The uncertain results of the CVNB fracture toughness tests are summarised in Table 5.6, with the data also plotted in figure 5.20. The raw data is contained in Appendix I.

Table 5.6: Summary of CVNB test results.

Material	Number of tests n	Average α_0	CVNB K_{Ic} $MPa.m^{1/2}$	Multotec K_{Ic} $MPa.m^{1/2}$
MP 92	5	0.16	3.14 ± 0.66	3.0
MP 96	8	0.10	3.95 ± 0.35	3.5
MP 99	11	0.12	3.71 ± 0.14	3.9

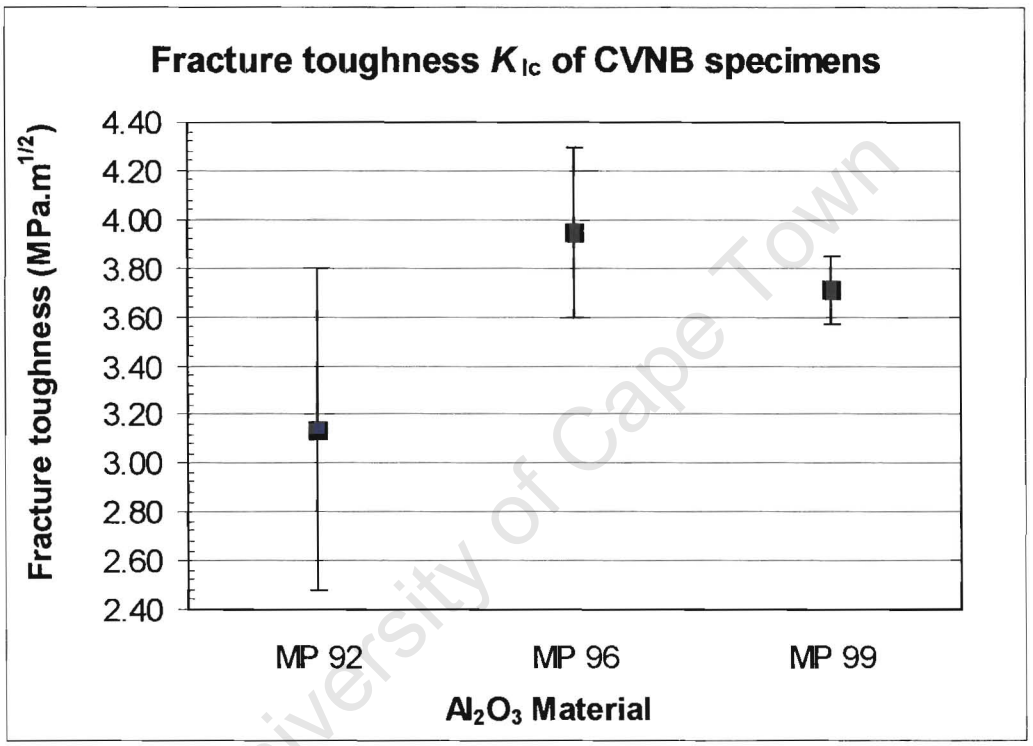

Figure 5.20: *Graph of the CVNB test results.*

There were no statistically significant differences in the results of the three materials, thus making it impossible to distinguish between K_{Ic} of the three materials. This is most probably due to the large scatter or error bands of the MP 92 and MP 96 materials, which in turn is probably a consequence of too few tests being performed on them (Table 5.6). The MP 92 material had the largest scatter and the fewest number of tests, since most of the MP 92 specimens broke during machining, as the MP 92 material was the first of the three materials to be chevron notched. The average K_{Ic} values did not match well with the Multotec quoted values, as evident in Table 5.6.

Looking at average K_{Ic} values only, it can be seen that the MP 96 and 99 materials had higher average K_{Ic} than the MP 92 material, but the MP 99 was lower than the MP 96 material again. This can again suggest that the toughness of the MP 99 material was being underestimated, or lend further support to the idea that the MP 99 material was in fact a lower toughness poorer quality material.

5.8 Comparison of results obtained from the different test techniques

5.8.1 Precision (repeatability) and resolution (discrimination) of results

The relative standard deviation of a complete particular test is defined as the ratio of the error band (or confidence interval) to the sample mean value. It is mathematically expressed as:

$$\%stds. = \left[\frac{s \cdot t}{\sqrt{n} \cdot \bar{x}}\right] \cdot 100$$

where

%stds is the defined relative standard deviation,

s is standard deviation of the sample measurements,

t is the t-value at 95 % confidence interval from t-distribution tables[29, 109],

n is the number of tests, or measurements in the sample, and

$\bar{x}$ is the average value of the sample measurements.

This relative standard deviation gives an indication of the *spread* or *scatter* of the results from the sample average. The *precision*, which is an indication of the *repeatability* of the average result, is therefore defined as the difference of the relative standard deviation from 100 %, i.e.

$$Precision = 100 - \%stds.$$

$$= 100 \cdot \left[1 - \left(\frac{s \cdot t}{\sqrt{n} \cdot \bar{x}}\right)\right]$$

Table 5.7 contains the calculated precision values for each combination of test technique, and test material together with the number of tests performed for each combination.

Table 5.7: Precision values and number of tests for each test technique performed on each material.

K_{Ic} *Test Techniques*	*MP 92*		*MP 96*		*MP 99*	
	No. of tests (n)	*Precision (%)*	*No. of tests (n)*	*Precision (%)*	*No. of tests (n)*	*Precision (%)*
IM Anstis	8	88.9	6	94.2	8	89.3
IM Liang	8	91.6	6	95.4	8	90.3
ISB	11	97.7	11	98.4	15	98.5
SENB-S	10	96.7	12	97.6	10	94.3
SEVNB	10	96.0	10	98.2	10	96.0
DT	8	95.2	8	95.7	10	97.6
CVNB	5	79.0	8	91.1	11	96.2

The calculated precision values from Table 5.1 are also plotted in figure 5.21 for graphical comparison.

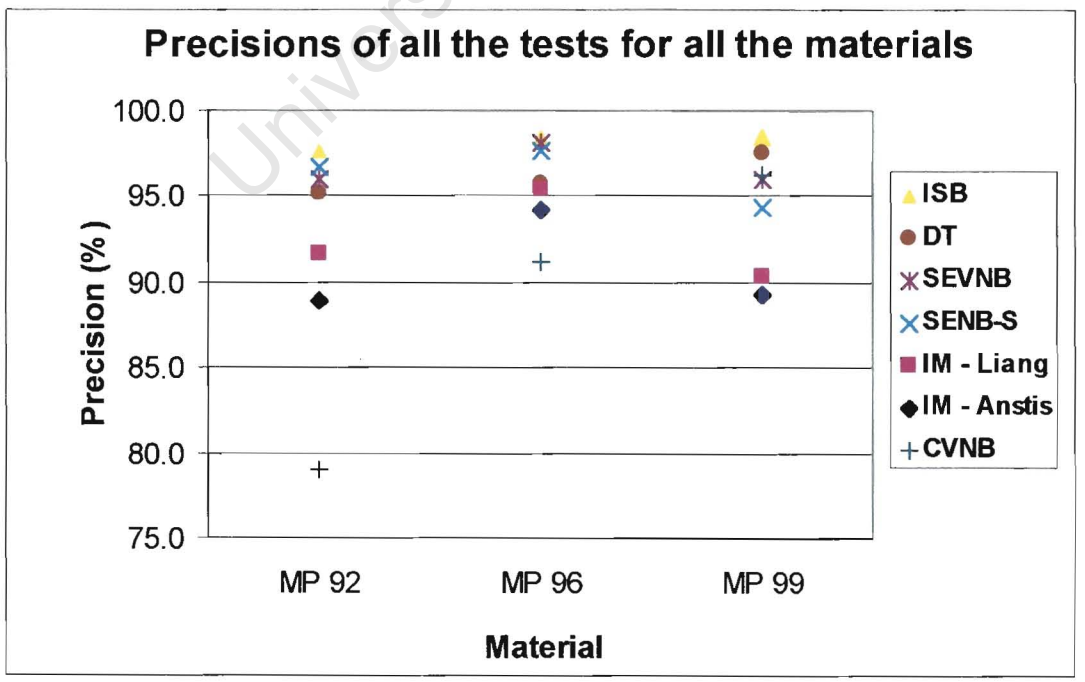

Figure 5.21: *Precision values for each test technique applied to the three different alumina materials.*

The precision of the ISB, SEVNB, and DT test techniques are consistenly higher than 95 % for all three materials, while the other techniques are not consistently above 95 % precision. The IM technique gives lower precision (88 – 95 %), which may be due to errors in measurement of the indentation induced *micron* cracks. The CVNB technique shows the lowest precision for the MP 92 and MP 96 materials. This is most probably due to fewer tests (Table 5.7) being performed on these materials, since the precision is higher (96.2 %) for the MP 99 material, where more tests (11 compared to 8 for MP 96, and 5 for MP 92) were done. Another possibility for the low precision of the CVNB test in the MP 92 material could be the machining quality of the chevron. The MP 92 material was the first to be chevron notched, with the machining quality not as good as the other two materials, where the machining got progressively better with the experience gained from machining the MP 92 material.

It can also be noticed from Table 5.7 that the precision of the MP 99 and MP 96 materials are generally higher than that of the MP 92 material. This suggests that the precision improves with material purity, since these materials have higher Al_2O_3 contents than the MP 92 material.

The *resolution*, or ability to *discriminate* between two different sets of results, is logically a function of the precision – the better the precision, the better the resolution capability. Resolution should not be taken for granted, since a lack of resolution in a test only leads to a meaningless test.

5.8.2 Discussion of all test results

All the test results have been discussed separately prior to this section, which will attempt to integrate discussion on all the results. Figure 5.22 shows the results (the average values, and their 95 % confidence intervals) of all the fracture toughness tests carried out on all three alumina materials, together with the Multotec quoted values for K_{Ic}. The test technique used to measure K_{Ic} for the Multotec value, as well as the scatter or confidence interval of this value was unknown to the author. This made it difficult to make direct comparisons between the results of this project and the Multotec value.

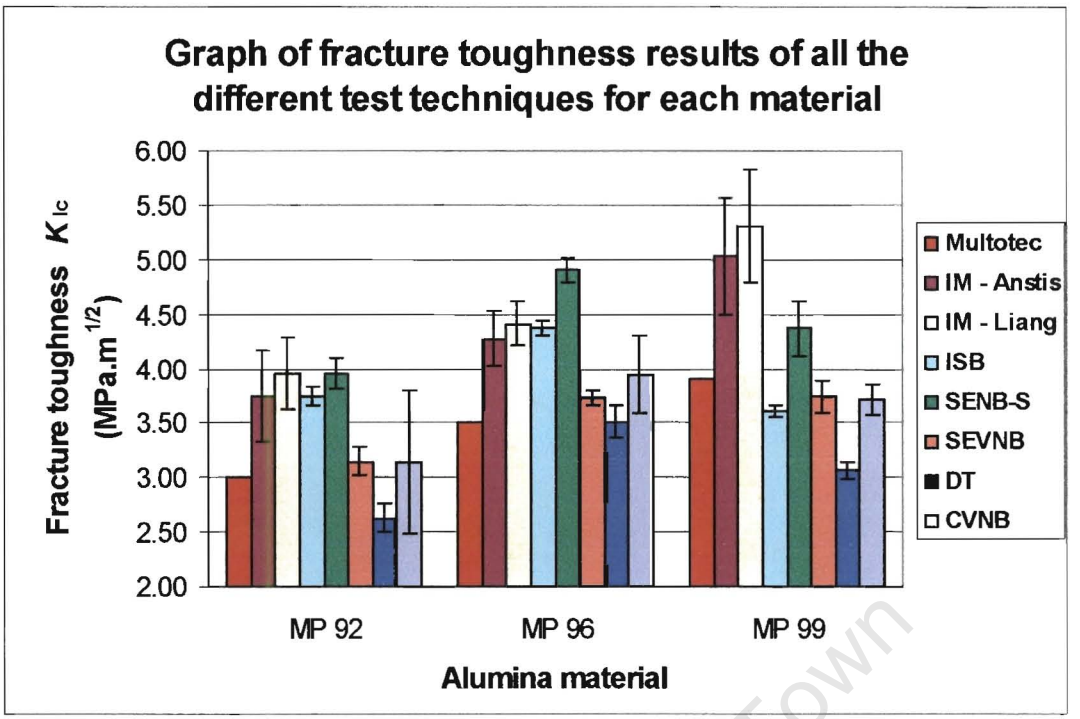

Figure 5.22: *Plot of all the fracture toughness results produced in this project. The 95 % confidence intervals of the means are included together with the quoted values by the manufacturers, Multotec Wear Linings Ltd.*

The IM results for estimating K_{Ic} appear to be significantly higher than the K_{Ic} value quoted by Multotec for all three materials. This is due to the semi-empirical IM technique overestimating K_{Ic}, as described in the literature, and might further suggest that the method used to measure the Multotec value was not the indentation microfracture method. In addition, the indentation fracture toughness K_{Ia} of the MP 99 material was significantly higher than that of the MP 96 material, which in turn was higher than that of the MP 92 material. The EDS scan results (shown in Table 5.1) suggest that the alumina content of the MP 99 material (91.5 %) was lower than the MP 96 material (94.1 %), which was supposed to have the lower content. This implies that the trend of increasing K_{Ia} from the MP 92 to the MP 96 to the MP 99 material is not directly attributable to the alumina content of the material. Figure 5.23, which is a plot of the fracture toughness results as a function of the alumina content confirms this. Table 5.1 also suggests that the grain size decreased from the MP 92 material to the MP 96 material to the MP 99 material, which had a significantly lower grain size than the other two materials. The IM results therefore appear to be influenced more by grain size than the alumina content. This could be

due to the smaller grain size, resulting in more grain boundaries, which probably arrest the indentation induced local microcracks.

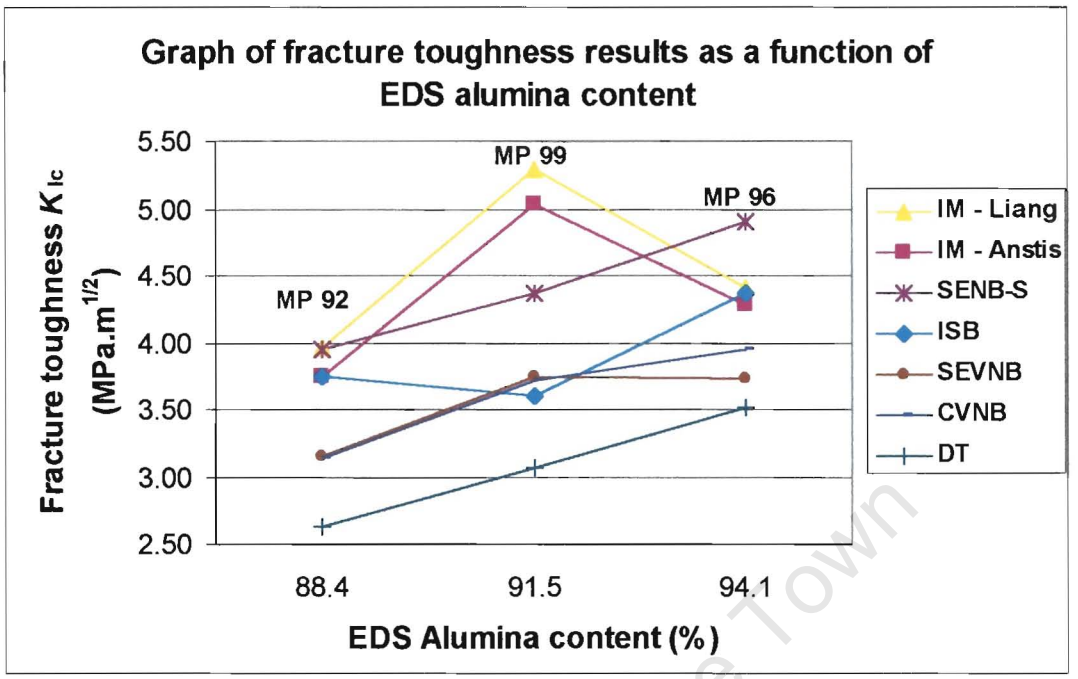

Figure 5.23: *Plot of average fracture toughness as a function of EDS alumina content. The confidence intervals were not included in this plot to avoid confusion, since they would have overlapped, and it would not be possible to distinguish between the error bars of the different test techniques.*

The results for the ISB, SENB-S, SEVNB, DT, and CVNB tests (figure 5.22) for the MP 99 material were either significantly lower, or not significantly different from the results of the same tests for the MP 96 material, which was quoted by Multotec to be less tough than the MP 99 material. Although the IM test gave K_{Ia} of the MP 99 material to be higher than the MP 96 material, it is still only a semi-empirical technique that is not strictly measuring fracture toughness, and has been subject to huge debate in the literature.

The bend tests mentioned above, excluding the ISB test, are conventional fracture toughness tests used to measure K_{Ic} (or estimate it, as in the case of the DT test). With the exception of the SEVNB test, these conventional tests appear to give the same trend of increasing K_{Ic} with increasing EDS alumina content between the three different alumina materials (figure 5.23). The reason for the similarity of K_{Ic} for the MP 96 and MP 99 materials is the difference in the notch tip radii between the test

materials. The larger notch tip radius of the MP 99, which was caused by the wearing of the cutting edge of the razor blade material, has resulted in an overestimate of K_{Ic} for this material. If the notch tip radius were smaller (which it would have been, had it not been for the cutting edge of the blade being worn off), K_{Ic} would also be smaller than is currently the case, and the trend between the materials would be the same as that of the other methods.

The consistency of ranking between the conventional fracture toughness tests, as shown by the trend in figure 5.23, confirms that the fracture toughness of the MP 99 material was ***in fact*** lower than that expected, and that the SENB, DT, and CVNB tests were thus not underestimating K_{Ic} for this material. This can be attributed to the lower alumina content of the MP 99 material (Table 5.1 and figure 5.23). Taking the IM results into consideration, it can be further inferred that the lower alumina content only becomes significant in "bulk" tests, or tests that involve high strain energies. Using indentation microfracture could thus be misleading to determining the true fracture toughness of a material to be used in a structural component that would experience large and distributed loads.

The ISB test did not follow the same ranking of either the IM test or the conventional fracture toughness tests, and appeared to be giving incorrect ranking between the MP 92 and MP 99 materials. The test also appears to be sensitive to the grain size, since it correctly distinguishes between the MP 92 and MP 96 materials, which had similar grain sizes, but appears to be underestimating K_{Ic} of the MP 99 material, which had a much smaller grain size than the other two materials. This suggests that the ISB test could "work" for materials with similar grain size. This test involves both *microfracture* (in indenting the specimen) and *macrofracture* (in loading the indented specimen in bending). The microfracture has been shown to be controlled by grain size in the IM tests, and the macrofracture by Al_2O_3 content in the conventional *macronotch* tests. The ISB test would involve an interaction of these phenomena, which is not understood by the author. Since both the *microflaw* test techniques result in incorrect ranking, they should be treated with caution.

The CVNB tests gave the worst precision, and consequently discrimination between materials was not possible with this test, but this may well be due to too few tests

being done, and it is possible that the precision and discrimination of this test could be improved with more testing. SENB-S tests result in overestimates in K_{Ic} due to the large notch tip radius created by the saw cut. The tests with the best precision have already been established in Section 5.8.1 – viz. the ISB, SEVNB, and DT tests. The ISB test is a semi-empirical test, while the DT test only gave a lower bound estimate of K_{Ic}, since V-K_I curves were not generated during this project. The SEVNB test appears to give more accurate K_{Ic} values than any of the other tests, and combined with its excellent precision, and discrimination, as well as ease of machining would make it the best K_{Ic} measuring technique found in this project.

5.8.3 Summary of each test technique

- **IM tests**

  - Although no extensive machining is required, specimen preparation (grinding and polishing), and crack measurements can be time consuming;
  - Crack lengths are very difficult to measure, introducing further error into the estimation of K_{Ic};
  - No significant differences between the Anstis *et al.* and Liang *et al.* formulae to determine K_{Ia}; although the Liang *et al.* formula gives a slightly higher precision;
  - Is semi-empirical, only leading to an estimate of K_{Ic}, which appears to be influenced by the grain size of the material, and not the alumina content;
  - Test results do not follow the same trend as the results of the conventional fracture toughness tests;
  - Appears to be measuring *a very localised microstructural fracture parameter*, that may not entirely be relevant for structural applications;
  - The author therefore suggests that this technique only be used with extreme caution.

- **ISB tests**

  - Specimen preparation can be time consuming;
  - No crack length measurements required;
  - Also a semi-empirical technique estimating K_{Ic}, but has better precision than all the other tests;
  - Results follow different trend to both the IM and the conventional fracture toughness test results;
  - Appears a promising technique (excellent precision), if the reasons for the incorrect ranking could be established;
  - This technique should also be treated with caution due to the problems discussed.

- **SENB-S tests**

  - Relatively simple specimen preparation and testing;
  - Overestimates K_{Ic} due to large notch tip radii;
  - Notch widths must be the same for direct comparisons;
  - Very good precision and discrimination;
  - Good technique for ranking different materials.

- **SEVNB tests**

  - Relatively simple specimen preparation and testing;
  - More accurate K_{Ic} due to smaller notch tip radii;
  - Notch tip radii of different materials should be equal for direct comparison purposes;
  - Excellent precision and discrimination, as well as accuracy;
  - Was found to be the best "all-round" technique used in the project.

- **DT tests**

  - Relatively simple specimen preparation;
  - Testing can be difficult due to difficulties in alignment and length of notch taper;
  - Only estimates a lower bound K_{Ic} due to lack of complete V-K_I curves;
  - Excellent precision and discrimination;
  - Can be used to rank different materials.

- **CVNB tests**

  - Difficult specimen preparation due to different specimen sizes;
  - Due to very small deflections, a very sensitive measuring device is needed;
  - In this project there appears to be poor precision and discrimination, but this may be due to too few tests, and it is possible that this technique has great potential, but for the high machining time and costs;
  - At present cannot rank the different materials in this project due to the huge scatter.

5.9 Summary of Chapter 5

This chapter presented the analysis and discussion for the results of the experimental techniques used in the project. The MP 99 material does indeed appear to have a lower Al_2O_3 content than expected, and consequently lower K_{Ic}. The IM and ISB tests do not give the same ranking as the other test methods, and appear to be more sensitive to the grain size of the material, than the material phase composition. These *microflaw* test techniques also show opposite trends to each other, the reason/s for which is unknown. The high strain energy tests appear to be more sensitive than the IM tests to the phase composition. Of all the tests used in this project, the SEVNB

seems the best to use in terms of suitability (ease of preparation and testing), precision, discrimination, and accuracy.

Chapter 6 contains the conclusions drawn from this project, with recommendations for future work also included.

CHAPTER 6:

CONCLUSIONS and RECOMMENDATIONS

6.1 Conclusions

- This thesis has undertaken a detailed review of the literature, and some specific experimental testing, in an attempt to determine the best technique/s of fracture toughness testing for brittle ceramics, particularly with a view to obtaining optimum precision and discrimination.

- Fracture toughness test techniques are divided into two broad categories, viz. specimens with *macronotches*, and specimens with indentation induced *microflaws*. Selected test techniques from both these categories (*macronotches* – SENB, DT, CVNB tests; *microflaws* – IM, ISB tests) were applied to three alumina materials with varying alumina contents.

- The macronotch test techniques, which are conventional fracture toughness tests, give consistent trends between the three materials. In addition to the microflaw test techniques not matching the trends of the macronotch test techniques, the tests within this microflaw category, viz. the IM and ISB tests, follow different trends. The macronotch test techniques therefore appear to be better than the indentation techniques.

- Indentation induced microcrack test techniques are semi-empirical, only estimating K_{Ic}. The IM and ISB tests give opposite trends to each other, with both resulting in the incorrect ranking between the materials. The ISB test has much better precision and discrimination than the IM test (the ISB precision was in fact the best for all the techniques in this project), and could have potential if more understanding is developed. The IM test appears to be measuring a very localised microstructural fracture parameter, which does not correspond well for macro loads, which are likely to be experienced by a

structural component in an industrial application. It is therefore suggested that indentation techniques be avoided.

- Of the specimens with macronotches, the SEVNB test appears to be the best in terms of accuracy, precision, and discrimination. The SENB-S specimen tends to overestimate K_{Ic} due to the larger notch tip radii, but still gives reasonable precision and discrimination. Discrimination was not possible for the CVNB tests due to low precision, but this may well be as a result of too few tests, a consequence of the difficult machining involved resulting in specimens getting damaged. The DT test has very good precision and discrimination, and also gives reasonable estimates of K_{Ic}, but is difficult to perform in terms of specimen, and load span alignment.

- It appears that the MP 99 material supplied for this particular project was a lower quality material, not containing the high Al_2O_3 content that was expected of such grade. K_{Ic} values measured for this material in this project were consequently lower than expected. Of the other two materials, the MP 96 was significantly tougher than the MP 92 material for all the test techniques used except the CVNB test, which showed poor precision, and discrimination.

- The best fracture toughness testing technique, found in this project for testing three different alumina materials was the SEVNB test. This test displayed the best combination of the following important factors: *suitability* (relatively easy to prepare), *precision* (excellent) and *discrimination*, as well as *accuracy*.

6.2 Recommendations for future work

- An automated mechanism could be set up for cutting the sharpened V notch in the SEVNB specimens. Examples of these are given in the literature.

- More CVNB tests could be done to improve the precision and discrimination, and then recheck how the data compare with the other tests. Also a more

sensitive range needs to be used for measuring the displacement in the load-displacement plot, which is necessary to check for stable crack growth.

- The ISB tests could be done over the load range suggested by Sakai *et al.* to see if there is an improvement in accuracy, since the test already shows excellent precision and discrimination. More work regarding the effect of grain size needs to be done before this technique could be used with confidence in estimating K_{Ic}.

- Another batch of MP 99 material, prepared to the correct specifications, could be obtained, and these materials tested, and compared with the results of this study.

- With regards to DEBID materials, the best technique to use to determine K_{Ic} would also appear to be the SEVNB test, which has shown excellent precision, discrimination, as well as being the most accurate test of those used in this project. All indentation techniques should be avoided for DEBID materials, since these materials contain compressive stresses, which is not permissible for indentation testing, in addition to the controversies surrounding these techniques.

REFERENCES

1 Sakai, M., and Bradt, R. C., International Materials Reviews, **38**, No. 2, 53 – 78, (1993).

2 Munz, D., and Fett, T., "Ceramics – Mechanical properties, Failure behaviour, Materials selection", Springer, Berlin, New York, London, etc., (1998).

3 Ewalds, H. L., and Wanhill, R. J. H., "Fracture Mechanics", Edward Arnold Publishers Ltd., London, (1984).

4 Liang, K. M., Orange, G., and Fantozzi, G., Journal of Materials Science, **25**, 207 – 214, (1990).

5 Naidu, T., "A literature review on the toughening and strengthening mechanisms in brittle materials", Mechanical Engineering Project, University of Cape Town, Department of Mechanical Engineering, (2000).

6 Xia, K., and Langdon, T. G., Journal of Materials Science, **29**, 5219 – 5231, (1994).

7 Green, D. J., Journal of Materials Science, **19**, 2165 – 2171, (1984).

8 Honeyman-Colvin, P., and Lange, F. F., Journal of the American Ceramic Society, **79**, No. 7, 1810 – 1814, (1996).

9 Zhengren, H., Cho, S., Jiang, D., and Tan, S., Journal of Materials Science, **34**, 2023 – 2027, (1999).

10 Wiederhorn, S. M., Annual Review of Materials Science, **14**, 373 – 403, (1984).

11 Heuer, A. H., and Hobbs, L. W., "Advances in Ceramics, Vol. 3, Science and Technology of Zirconia", The American Ceramic Society, Inc., Columbus, Ohio, (1981).

12 Wang, J., and Stevens, R., Journal of Materials Science, **24**, 3421 – 3440, (1989).

13 Lange, F. F., Journal of Materials Science, **17**, 247 – 254, (1982).

14 Lange, F. F., Journal of Materials Science, **17**, 254 - 262, (1982).

15 Wang, J., and Stevens, R., Journal of Materials Science, **23**, 804 - 808, (1988).

16 Heuer, A. H., Lange, F. F., Swain, M. V., and Evans, A. G., Journal of the American Ceramic Society, "Transformation Toughening: An overview", **69**, No. 7, i – iv, (1986).

17 Shi, J. L., Li, B. S., and Yen, T. S., Journal of Materials Science, **28**, 4019 – 4022, (1993).

18 Swain, M. V., Journal of Hard Materials, **2**, No. 1-2, 139 – 154, (1991).

19 Mitchell, T., Jr., De Jonghe, L. C., MoberlyChan, W. J., and Ritchie, R. O., Journal of the American Ceramic Society, **78**, No. 1, 97 – 103, (1995).

20 Quinn, G. D., Gettings, R., and Xu, K., Ceramic Engineering and Science Proceedings, **20**, No. 3, 513 – 523, (1999).

21 ASTM E 399 – 90, "Standard Test Method for Plane-Strain Fracture Toughness of Metallic Materials", ASTM, (1990).

22 Y. Murakami *et al.* (eds.): "Stress intensity factors handbook", Vols. 1 & 2, Oxford, Pergamon, (1987).

23 BS 7448: "Part1. Method for determination of K_{Ic}, critical CTOD and critical J values of metallic materials", BSI, (1991).

24 ASTM E 1304 – 89, "Standard Test Method for Plane-Strain (Chevron Notch) Fracture Toughness of Metallic Materials, ASTM, (1989).

25 ASTM B 771 - 87, "Standard Test Method for Short Rod Fracture Toughness of Cemented Carbides", ASTM, (1987).

26 Nose, T., and Fujii, T., Journal of the American Ceramic Society, **71**, No. 5, 328 – 333, (1988).

27 Grendahl, S., Bert, R., Cho, K., and Bar-On, I., Journal of the American Ceramic Society, **83**, No. 10, 2625 – 2627, (2000).

28 Mukhopadhyay, A. K., Datta, S. K., and Chakraborty, D., Ceramics International, **25**, 447 – 454, (1999).

29 Jayatilaka, A. De S., "Fracture of Engineering Brittle Materials", Applied Science Publishers Ltd., London, (1979).

30 Primas, R. J., and Gstrein, R., "ESIS TC 6 Round Robin on Fracture Toughness", Fatigue and Fracture of Engineering Materials and Structures Ltd., **20**, No. 4, 513 – 532, (1997).

31 Shemilt, J. E., Williams, H. M., Edirisinghe, M. J., Evans, J. R. G., and Ralph, B., Scripta Materialia, **36**, No. 8, 929 – 934, (1997).

32 Selcuk, A., and Atkinson, A., Journal of the American Ceramic Society, **83**, No. 8, 2029 – 2035, (2000).

33 Choi, S. R., and Salem, J. A., Journal of the American Ceramic Society, **77**, No. 4, 1042 – 1046, (1994).

34 Personal experience from De Beers Diamond Research Laboratory (1999).

35 Lawn, B. R., and Wilshaw, T. R., "Fracture of Brittle Solids", Cambridge University Press, (1975).

36 Pavelchek, E. K., and Doremus, R. H., Journal of Materials Science, **9**, 1803 – 1808, (1974).

37 Knott, J. F., "Fundamentals of Fracture Mechanics", Butterworth and Co. Publishers, London, (1973).

38 Kanninen, M. F., and Popelar, C. H., "Advanced Fracture Mechanics", Oxford Engineering Science Series, **15**, Oxford University Press, (1985).

39 Taylor, P. C., "Fatigue and Fracture of Cement Mortars Containing Fly ash", PhD thesis, University of Cape Town, (1995).

40 Middlemiss, S., "A study of the Fracture Toughness of Some Witwatersrand Quartzites", MSc Thesis, University of Cape Town, (1991).

41 Wachtman, J. B., "Mechanical Properties of Ceramics", John Wiley & Sons, Inc., New York, (1996).

42 Gilbert, C. J., Cao, J. J., De Jonghe, L. C., and Ritchie, R. O., Journal of the American Ceramic Society, **80**, No. 9, 2253 – 2261, (1997).

43 Kovar, D., Bennison, S. J., and Readley, M. J., Acta Materialia, **48**, 565 – 578, (2000).

44 Warren, R., and Johanneson, B., Powder Metallurgy, **27**, No. 1, 25 – 29, (1984).

45 Sherman, D., Journal of the American Ceramic Society, **80**, No. 7, 1904 – 1906, (1997).

46 Scherrer, S. S., Denry, I. L., and Wiskott, H. W. A., Dental Materials, **14**, 246 – 255, (1998).

47 Kokabi, V. C., Shobu, K., and Watatanabe, T., Journal of the European Ceramic Society, **17**, 885 – 890, (1997).

48 Deng, J., and Ai, X., Materials Research Bulletin, **33**, No. 4, 575 – 582, (1998).

49 Hiramatsu, K., Okada, A., and Usami, H., Ceramic Engineering and Science Proceedings, **19**, 335 – 340, (1998).

50 Kübler, J., Ceramic Engineering and Science Proceedings, **18**, No. 4B, 155 – 162, (1997).

51 Damani, R., Gstrein, R., and Danzer, R., Journal of the European Ceramic Society, **16**, 695 – 702, (1996).

52 Torres, Y., Casellas, D., Anglada, M., and Lanes, L., International Journal of Refractory Metals and Hard Materials, **19**, 27 – 34, (2001).

53 Damani, R. J., Schuster, C., and Danzer, R., Journal of the European Ceramic Society, **17**, 1685 – 1689, (1997).

54 Lin, J. S., and Miyamoto, Y., Acta Materialia, **48**, 767 – 775, (2000).

55 Hansson, T., Ramamurty, U., Bull, C., and Warren, R., Materials Science and Engineering A209, 137 – 148, (1996).

56 Gogotsi, G. A., Zavada, V. P., and Swain, M. V., Journal of the European Ceramic Society, **16**, 545 – 551, (1996).

57 Petersson, M. K. H. and Bergman, B., British Ceramic Proceedings, No. 39, pp. 15-23, (1987).

58 She, J., Inoue, T., and Ueno, K., Ceramics International, **26**, 801 – 805, (2000).

59 Inoue, T., and Ueno, K., Ceramics International, **24**, 565 – 569, (1998).

60 Tait, R. B., Fry, P. R., and Garrett, G. G., Experimental Mechanics, 14 – 22, March 1987.

61 Pletka, B. J., Fuller, E. R. Jr., and Koepke, B. G., ASTM STP 678, 19 – 37, (1979).

62 Fuller, E. R. Jr., ASTM STP 678, 3 – 18, (1979).

63 Chevalier, J., Saadaoui, M., Olagnon, C., and Fantozzi, G., Ceramics International, **22**, 171 – 177, (1996).

64 Kahraman, R., Mandell, J. F., and Deibert, M. C., Journal of the American Ceramic Society, **80**, No. 7, 1812 – 1820, (1997).

65 Kahraman, R., and Mandell, J. F., Journal of Composite Materials, **31**, No. 20, 2038 – 2051, (1997).

66 Saadaoui, M., Reynaud, P., Fantozzi, G., Peronnet, F., and Caspar, J. P., Ceramics International, **26**, 435 – 439, (2000).

67 Wereszczak, A. A., Ferber, M. K., and Parvizi-Majidi, A., Journal of Composite Materials, **31**, No. 19, 1905 – 1920, (1997).

68 Govila, R. K., Journal of the American Ceramic Society, **63**, No. 5 – 6, 319 – 326, (1980).

69 Wecharatana, M., and Shah, S. P., Cement and Concrete Research, **10**, 833 – 844, (1980).

70 Munz, D. G., Shannon, J. L., Jr., and Bubsey, R. T., International Journal of Fracture, **16**, R137 – R141, (1980).

71 Munz, D., Bubsey, R. T., and Shannon, J, L., Jr, Journal of the American Ceramic Society, **63**, No. 5 – 6, 300 – 305, (1980).

72 Ünal, Ö, and Okumus, S. C., Journal of Materials Science Letters, **19**, 939 – 941, (2000).

73 Sarrafi-Nour, G. R., and Coyle, T. W., Journal of the American Ceramic Society, **82**, No. 9, 2474 – 2480, (1999).

74 Barker, L. M., Engineering Fracture Mechanics, **9**, 361 – 369, (1977).

75 Barker, L. M., ASTM STP 678, 73 – 82, (1979).

76 Barker, L. M., Journal of Testing and Evaluation, **17**, No. 4, 218 – 223, (1989).

77 Barker, L. M., and Baratta, F. I., Journal of Testing and Evaluation, **8**, No. 3, 97 – 102, (1980).

78 Barker, L. M., Fracture Mechanics of Ceramics, edited by R. C. Bradt, D. P. H. Hasselman, F. F. Lange, **3**, 483 – 494, (1978).

79 Biner, S. B., Barnby, J. T., Elwell, D. W. J., International Journal of Fracture, **26**, 3 – 16, (1984).

80 Shannon, J. L., Jr, Bubsey, R. T., Pierce, W. S., and Munz, D. G., International Journal of Fracture, **19**, R55 – R58, (1982).

81 Barker, L. M., International Journal of Fracture, **19**, R3 – R7, (1982).

82 Bubsey, R. T., Munz, D., Pierce, W. S., and Shannon, J. L. Jr., International Journal of Fracture, **18**, No. 2, (1982).

83 Barker, L. M., Engineering Fracture Mechanics, **17**, No. 4, 289 – 312, (1983).

84 Sacks, N., "The Fracture Toughness of Ultrafine WC-Co Alloys", MSc thesis, University of Cape Town, (1999).

85 Armstrong, S. R., Keller, J. C., and Boyer, D. B., Dental Materials, **17**, 201 – 210, (2001).

86 Lewis, G., Nyman, J., and Trieu, H. H., Biomaterials, **19**, 961 – 967, (1998).

87 Lee, D., Journal of Materials Science, **30**, 4617 – 4622, (1995).

88 Armstrong, S. R., Boyer, D. B., Keller, J. C., and Park, J. B., Dental Materials, **17**, 201 – 210, (2001).

89 Evans, A. G., ASTM STP 678, 112 – 135, (1979).

90 Spiegler, R., Schmauder, S., and Sigl, L. S., Journal of Hard Materials, **1**, No. 3, (1990).

91 Marshall, D. B., Journal of the American Ceramic Society, **66**, No. 2, 127 – 131, (1983).

92 Anstis, G. R., Chantikul, P., Lawn, B. R., and Marshall, D. B., Journal of the American Ceramic Society, **64**, No. 9, 533 – 538, (1981).

93 Dietz, M., and Tietz, H. –D., Journal of Materials Science, **25**, 3731 – 3738, (1990).

94 Petrovic, J. J., and Mendiratta, ASTM STP 678, 83 – 102, (1979).

95 Quinn, G. D., Gettings, R. J., and Kübler, J. J., Ceramic Engineering and Science Proceedings, 15, 846 – 854, (1994).

96 Tracy, C. A., and Quinn, G. D., Ceramic Engineering and Science Proceedings, 15, 837 –845, (1994).

97 Scherrer, S. S., Denry, I. L., Wiskott, H. W. A., and Belser, U. C., Dental Materials, **17**, 367 – 371, (2001).

98 Marion, R. H., ASTM STP 678, 103 – 111, (1979).

99 Guillou, M. –O., Henshall, J. L., Hooper, R. M., and Carter, G. M., Journal of Hard Materials, **3**, Nos. 3 – 4, 421 – 434, (1992).

100 Gorman, C. M., McDevitt, W. E., and Hill, R. G., Dental Materials, **16**, 389 – 395, (2000).

101 Biswas, K., Rixecker, G., Wiedmann, I., Schweizer, M., Upadhyaya, G. S., and Aldinger, F., Materials Chemistry and Physics, **67**, 180 – 191, (2001).

102 Liu, Q., Gao, L., Yan, D. S., and Thompson, D. P., Materials Science and Engineering, A269, 1 – 7, (1999).

103 Celli, A., Tucci, A., and Esposito, L., Journal of the European Ceramic Society, **19**, 441 – 449, (1999).

104 Thiel, S., and Schnapp, J. D., Journal of Non-Crystalline Solids, **242**, 189 – 194, (1998).

105 Chantikul, P., Anstis, G. R., Lawn, B. R., and Marshall, D. B., Journal of the American Ceramic Society, **64**, No. 9, 539 – 543, (1981).

106 Scherrer, S. S., Kelly, J. R., Quinn, G. D., and Xu, K., Dental Materials, **15**, 342 – 348, (1999).

107 Zhu, Q., and Shobu, K., Journal of Materials Science Letters, **19**, 1529 – 1531, (2000).

108 Kaya, C., Kaya, F., Trusty, P. A., Boccaccini, A. R., and Marsoglu, M., Ceramics International, **25**, 359 – 366, (1999).

109 Underhill, L., and Bradfield, D., "Introstat 5.0", Juta and Co. Ltd., Creda Press, Epping, (1994).

APPENDICES

APPENDIX A – *Summary of previous investigators' experimental parameters*
APPENDIX B – *Newman and Raju's stress intensity factor for a surface crack*
APPENDIX C – *Drawings for bend test components*
APPENDIX D – *Drawings for CVN specimen geometries*
APPENDIX E – *Raw data for IM tests*
APPENDIX F – *Raw data for ISB tests*
APPENDIX G – *Raw data for SENB tests*
APPENDIX H – *Raw data for DT tests*
APPENDIX I – *Raw data for CVNB tests*

APPENDIX A

- Summary of previous investigators' experimental parameters

SENB data

Ref. No.	Author	Date Year	3 / 4 point bending?	Cross-head speed	DIMENSIONS AND SPANS					RATIOS				No. of tests	MATERIALS TESTED
					L	*W*	*B*	S_1	S_2	*a/W*	*B/W*	*L/W*	S_1/W		
				mm/min OR *$MPam^{1/2}/s$	mm	mm	mm	mm	mm						
21	ASTM E399 – 90	1990	3	0.55 - 2.75 *	4.2W	W	W/2	4W	0	0.45 - 0.55	0.5	4.2	4	>=3	Standard for metallic materials
23	BS 7448	1991	3	0.5 - 3 *	4.6W	W	W/2	4W	0	0.45 - 0.55	0.5	4.6	4	>=3	Standard for metallic materials
57	Petersson et al	1987	4	0.1	-	9.5	7	40	20	0.5	0.74	-	4.21	-	Al_2O_3-ZrO_2 materials
33	Choi & Salem	1994	4	0.2	-	4.0	3	18	10		0.75	-	4.5	9	in situ toughened Si3N4
51	Damani et al	1996	4 pt SENB - S	12 - 15	45	4.0	3	-	-	0.5	0.75	11.3	-	-	Al_2O_3, ZrO_2, MgPSZ, HPSN, SSiC
56	Gogotsi et al	1996	3	-	25	4.8	2.8	20	0	0.5	0.58	5.21	4.17	-	9 mol % Ce-TZP materials
55	Hansson et al	1996	4	0.02 - 0.2 *	25	5.0	2.5	20	10	0.34	0.5	5	4	-	Si_3N_4 materials
59	Inoue & Ueno	1996	3	0.498	20	4.0	3	16	0	-	0.75	5	4	4	SiTiCO fibre/ SiAlON composite
31	Shemilt et al	1996	4	1	65	9.0	6	40	20	~0.3	0.67	7.22	4.44	-	doped ceria ceramics
53	Damani et al	1997	4 pt SENB - S	-	45	4.0	3	-	-	0.5	0.75	11.3	-	-	Al_2O_3, ZrO_2, MgPSZ, HPSN, SSiC
47	Kokabi et al	1997	3	-	-	2.5	4	10	0	-	1.6	-	4	-	metal borides
50	Kubler	1997	4 - SEVNB	-	45	4.0	3	40	20	~0.25	0.75	11.3	10	5	ceramic materials
50	Kubler	1997	4 - SEVNB	-	25	2.5	2	20	10	~0.25	0.8	10	8	5	ceramic materials
48	Deng & Ai	1998	4	0.1	40	5.0	5	24	12	-	1	8	4.8	4 - 6	TiB_2-SiCw composites

49	Hiramatsu et al	1998	3 - stabilisers	-	30	4.0	3	16	0	0.63	0.75	7.5	4	-	sintered silicon nitride
2	Munz & Fett	1998	4	-	-	4.0	3	40	20	0.5	0.75	-	10	-	
46	Scherrer et al	1998	4 pt SEVNB	0.25	25	3.0	2	20	10	0.3	0.67	8.33	6.67	5	Dental materials
54	Lin & Miyamoto	1999	ASTM E399	0.5	25	8.0	3.5	-	-	-	0.44	3.13	-	-	graded Al_2O_3/TiC/Ni materials
28	Mukhopadhyay et al	1999	4	-	45	4.5	3.5	40	20	-	0.78	10	8.89	4 - 6	Al_2O_3, SSN, SSiC
52	Torres et al	1999	4/SENB&SEVNB	-	45	10	5	40	20	0.3	0.5	4.5	4	3	WC - Co hardmetals
27	Grendahl et al	2000	4-brg ind. Precrk	0.5	50	4.0	3	40	20	~0.25	0.75	12.5	10	3 - 10	aluminum nitride
27	Grendahl et al	2000	3-brg ind. Precrk	0.5	50	4.0	3	16	0	~0.25	0.75	12.5	4	3 - 10	aluminum nitride
58	She et al	2000	4	0.1	40	4.0	3	30	10	0.38	0.75	10	7.5	3 - 4	multilayer Al_2O_3/SiC ceramics

Double torsion (DT) data

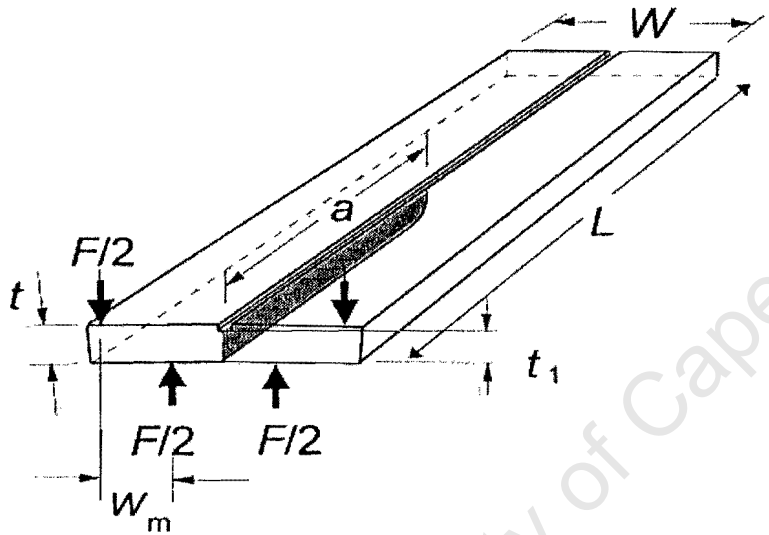

Ref. No.	Reference	Date Year	3 / 4 pnt	Cross-head speed	DIMENSIONS					GROOVED		a_0	Pre-crack	RATIOS			MATERIALS TESTED
					L	*W*	W_m	*t*	t_1	Single	Double			*L / W*	*t / W*	t_1 / W	
				mm/min	mm	mm	mm	mm	mm			mm	mm				
61	Tait & Garrett	1985	4		180	60		8	4.6	*	no	-	-	3	0.133	0.077	Mortar
64	Chevalier et al	1996	3	-	40	20	8.5	2	0	no	no	10	13	2	0.100	-	3Y-TZP
65-6	Kahraman et al	1997	4	89 N/min	65.4	21.8	-	3	0	no	no	-	>12.5	3	0.138	-	glass-ceramic matrix comp's
67	Saadaoui et al	2000	3	0.1	300	180		10	0	no	no	100	10 - 20	1.67	0.056	-	plaster
32	Selcuk & Atkinson	2000	4	0.2 - 9	50	25	9	0.15	0	no	no	-	-	2	0.006	-	yttria stabilised zirconia

CVNB data

Ref. No.	Reference	Date year	3 / 4 point	Cross-head speed	DIMENSIONS AND SPANS					RATIOS					No. of tests	MATERIALS TESTED
					L	*W*	*B*	S_1	S_2	a_0/W	a_1/W	*B/W*	*L/W*	S_1/W		
				mm/min OR *MPam$^{1/2}$/s	mm	mm	mm	mm	mm							
57	Petersson et al	1987	4	0.1	-	9.5	7	40	20	0.11	0.7	0.74	-	4.211	-	Al_2O_3 materials
33	Choi & Salem	1994	4	0.1	-	4	3	30	10	0.35	1	0.75	-	7.5	5	toughened Si_3N_4's
68	Wereszczak et al	1997	4	-	50	5 or 6.9	3 or 3.9	40	20	-	1	~0.6	~10	8	-	SiC whisker reinf Al_2O_3
28	Mukhopadhyay et al	1999	4	0.015-0.15	45	4.5	3.5	-	-	0.2	1	0.78	10	-	4 - 6	Al_2O_3, SiC, SSN, Si_3N_4
74	Sarraffi-Nour et al	1999	4	0.05	45	5	4	40	20	0.32	1	0.8	9	8	-	SiC-Al_2O_3 composite
73	Unal & Okumus	2000	4	0.12	25	4	3	20	10	0.375	1	0.75	6.25	5	-	plasma sprayed Mo_5Si_3-MoB-$MoSi_2$ alloy

CVSR data

Ref. No.	Reference	Rod / Bar R / B	Date Year	DIMENSIONS			RATIOS					Angle 2θ	No. of tests	MATERIALS TESTED
				W	*B*	*2H*	a_0 / *W*	a_1 / *W*	*W/B*	*2H/B*	*t/B*			
				mm	mm	mm	α_0	α_1				degrees		
24	ASTM E1304 -89	R & B	1989	1.45B	B	B	0.481B	-	1.45	0.481	<=0.03B	54.6	>=3	Standard for metallic materials
25	ASTM B771 -87	R & B	1992	19.05	12.7	11.05	0.3333	-	1.5	0.8701	<=0.03B	58	>=3	Standard for cemented carbides
75	L. M. Barker	R	1979	1.5B	B	-	0.531	-	1.5	0.87	0.030	55.2	5 - 6	Al_2O_3, fused quartz
87	Dong-Joo Lee	B	1995	19.05	12.7	11	0.3543	1	1.5	0.8661	0.031	55.2	-	Si_3N_4 matls; Al_2O_3-20%SiC w
85	Armstrong et al	B	1998	5.8	4	4	0.331	1	1.45	1	-	54.6	10	Dentin - resin composite
86	Lewis et al	R	1998	19.05	12.7	-	0.3538	-	1.5	-	0.030	55.2	6	Acrylic bone cement

Indentation microfracture (IM) data

Ref. No.	Reference	Date Year	No. of tests	Indent Load	Indent time	K_{Ia} Equation	Materials tested
				N	s or min		
57	Petersson et al	1987	-	-	-	Lawn/Anstis	Al_2O_3 matls
4	Liang et al	1990	-	1 - 500	-	New eqn - Liang	Zirconia toughened Al_2O_3
90	Spiegler et al	1990	>=3	300-2500	-	few equations	WC-Co alloys
99	Guillou et al	1992	-	9.8 - 883	-	20 equations	SiC, ZrO2, Si_3N_4
33	Choi & Salem	1994	5/load	49 - 294	20 s	Anstis	toughened Si_3N_4
47	Kokabi et al	1997	-	196	-	-	TiB_2 materials
31	Schemilt et al	1997	10	1.9 - 4.9	-	Anstis	doped ceria ceramics
46	Scherrer et al	1998	10	9.8 & 19.6	-	Anstis	dental materials
104	Thiel et al	1998	-	2	10 s	Evans + Charles	glass-ceramic
103	Celli et al	1999	-	98.1	-	Anstis	Si_3N_4-SiCwhiskers
102	Liu et al	1999	-	98	10 min	-	SiC nanoparticles
28	Mukhopadhyay et al	1999	4 - 6	-	-	Anstis	Al_2O_3, SiC, SSN
52	Torres et al	1999	10	196 - 980	-	-	WC-Co hardmetals
100	Gorman et al	2000	-	2.94	15s	Anstis	dental materials
32	Selcuk & Atkinson	2000	-	0.98 - 4.9	15s	few equations	ytrria stabilised zirconia
101	Biswas et al	2001	12	50	-	Anstis	SiC ceramics
97	Scherrer	2001	10	19.6	-	Anstis	dental materials

ISB data

Ref. No.	Reference	Date Year	Loading 3 / 4 point	Cross-head speed	Indent load P	DIMENSIONS AND SPANS					RATIOS			No. of tests	MATERIALS TESTED
						L	W	B	S_1	S_2	B/W	L/W	$S1/W$		
				mm/min	N	mm	mm	mm	mm	mm					
57	Petersson et al	1987	4	0.1	-	-	8.1	7	25	15	0.86	-	3.086	-	Al_2O_3-ZrO_2's
33	Choi & Salem	1994	4	0.2	49 - 294	25	3	4	18	10	1.33	8.33	6	3	toughened Si_3N_4's
46	Scherrer et al	1998	3	0.1	9.8 or 19.6	25	4.5	2	21	0	0.44	5.56	4.667	10	Dental materials
108	Kaya et al	1999	4	0.5	294	-	-	-	35	25	-	-	-	-	Al_2O_3/Y-TZP nano-ceramics
106	Scherrer et al	1999	3	0.1	9.8 or 19.6	25	4.5	2	21	0	0.44	5.56	4.667	9	Dental materials
58	She et al	2000	3	0.5	3 - 500	40	4	3	30	0	0.75	10	7.5	3	Al_2O_3/SiC ceramics
107	Zhu & Shobu	2000	3	0.07	98	12	3	1.5	8	0	0.5	4	2.667	-	SiC composite
97	Scherrer et al	2001	3	0.1	19.6	25	4.5	2	21	0	0.44	5.56	4.667	10	dental glass

APPENDIX B

Newman and Raju's stress intensity factor for a surface crack

Newman and Raju used the following polynomials to calculate the stress intensity factor for a semi-elliptical surface crack in bending **[Scherrer *et al.* – ref. 97]**:

$$M = \left[1.13 - 0.09\left(\frac{a}{c}\right)\right] + \left[\frac{0.89}{0.2 + (a/c)} - 0.54\right]\left(\frac{a}{d}\right)^2 + \left[0.5 - \frac{1}{0.65 + (a/c)} + 14\left(1 - \left(\frac{a}{c}\right)\right)^{24}\right]\left(\frac{a}{d}\right)^4,$$

$$H_2 = 1 - \left(1.22 + 0.12\left(\frac{a}{c}\right)\right)\left(\frac{a}{d}\right) + \left[0.55 - 1.05\left(\frac{a}{c}\right)^{0.75} + 0.47\left(\frac{a}{c}\right)^{1.5}\right]\left(\frac{a}{d}\right)^2,$$

$$H_1 = 1 - \left(0.34 + 0.11\left(\frac{a}{c}\right)\right)\left(\frac{a}{d}\right),$$

$$\sqrt{Q} = \sqrt{1 + 1.464\left(\frac{a}{c}\right)^{1.65}},$$

$$S = \left[1.1 + 0.35\left(\frac{a}{d}\right)^2\right]\sqrt{\left(\frac{a}{c}\right)},$$

$$Y_{depth} = \frac{M}{\sqrt{Q}} H_2 \sqrt{\pi},$$

$$Y_{surface} = S\frac{M}{\sqrt{Q}} H_1 \sqrt{\pi},$$

$$K_{Ic} = Y_{\max}\sigma_f \sqrt{a} \qquad (\text{MPam}^{1/2})$$

APPENDIX C

Drawings for bend test components:-

1. Upper / outer load span for ISB, SENB, and CVNB tests
2. Lower / outer load span for DT tests
3. Rollers and roller seats for ISB, SENB, and CVNB tests
4. Shaft and sleeve to attach load spans to ESH components

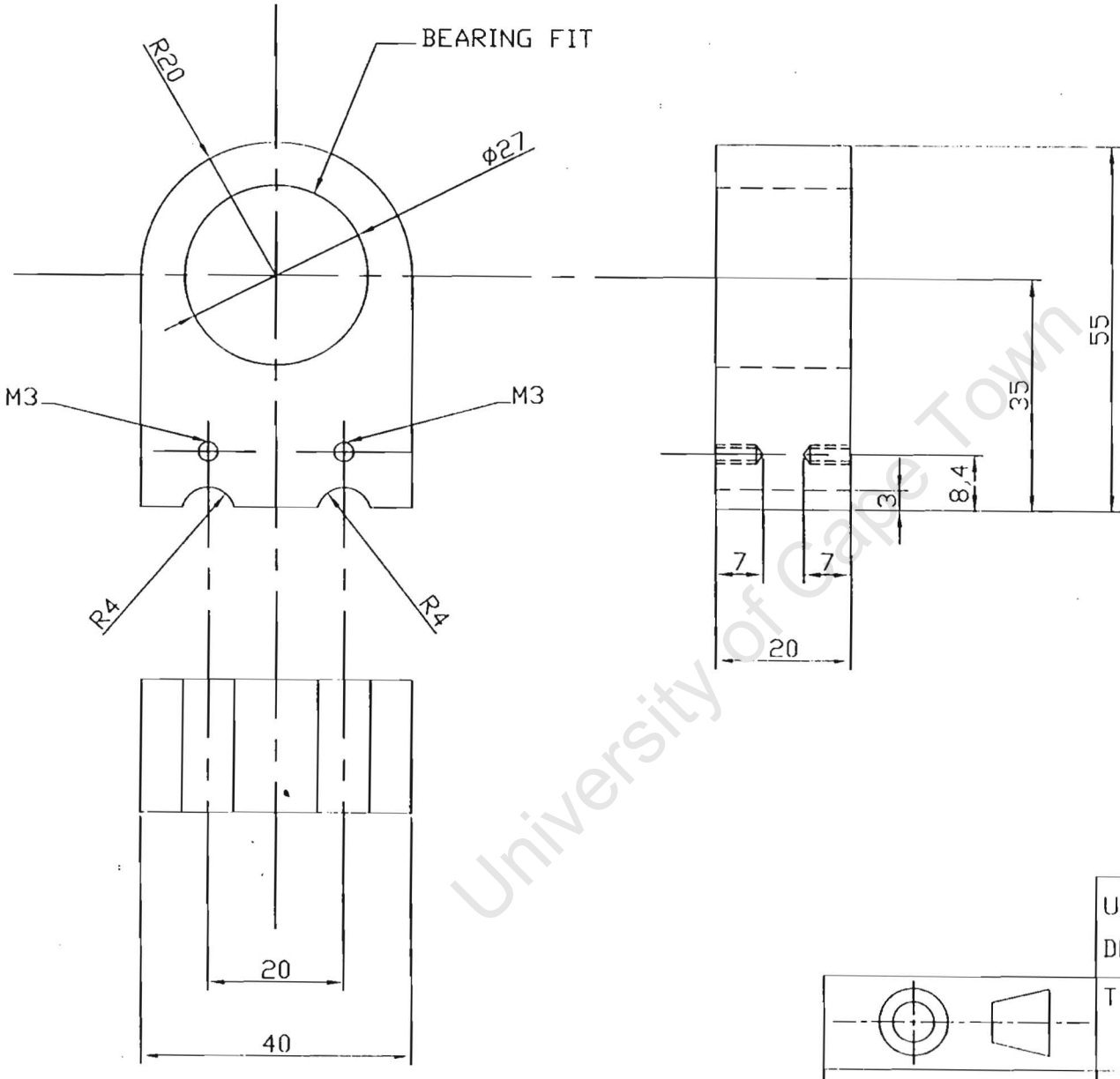

NOTES :

1. SKF BEARING NKI 15/20 TO BE FITTED IN 27 mm DIAMETER HOLE
2. 2 HOLES TO BE THREADED ON EACH SIDE TO BE M3 AND 7 mm DEEP.
3. TO BE MANUFACTURED FROM 431 STAINLESS STEEL MATERIAL
4. REMOVE ALL BURRS AND SHARP EDGES

UNIVERSITY OF CAPE TOWN
DEPARTMENT OF MECHANICAL ENGINEERING

TITLE
4 POINT BENDING UPPER / INNER SPAN

ALL DIMENSIONS IN MILLIMETRES
TOLERANCES 0.1 mm

SCALE	DATE	SHEET 1 OF 1
1:1	29/08/01	
DRAWN BY T. NAIDU		DRAWING NUMBER

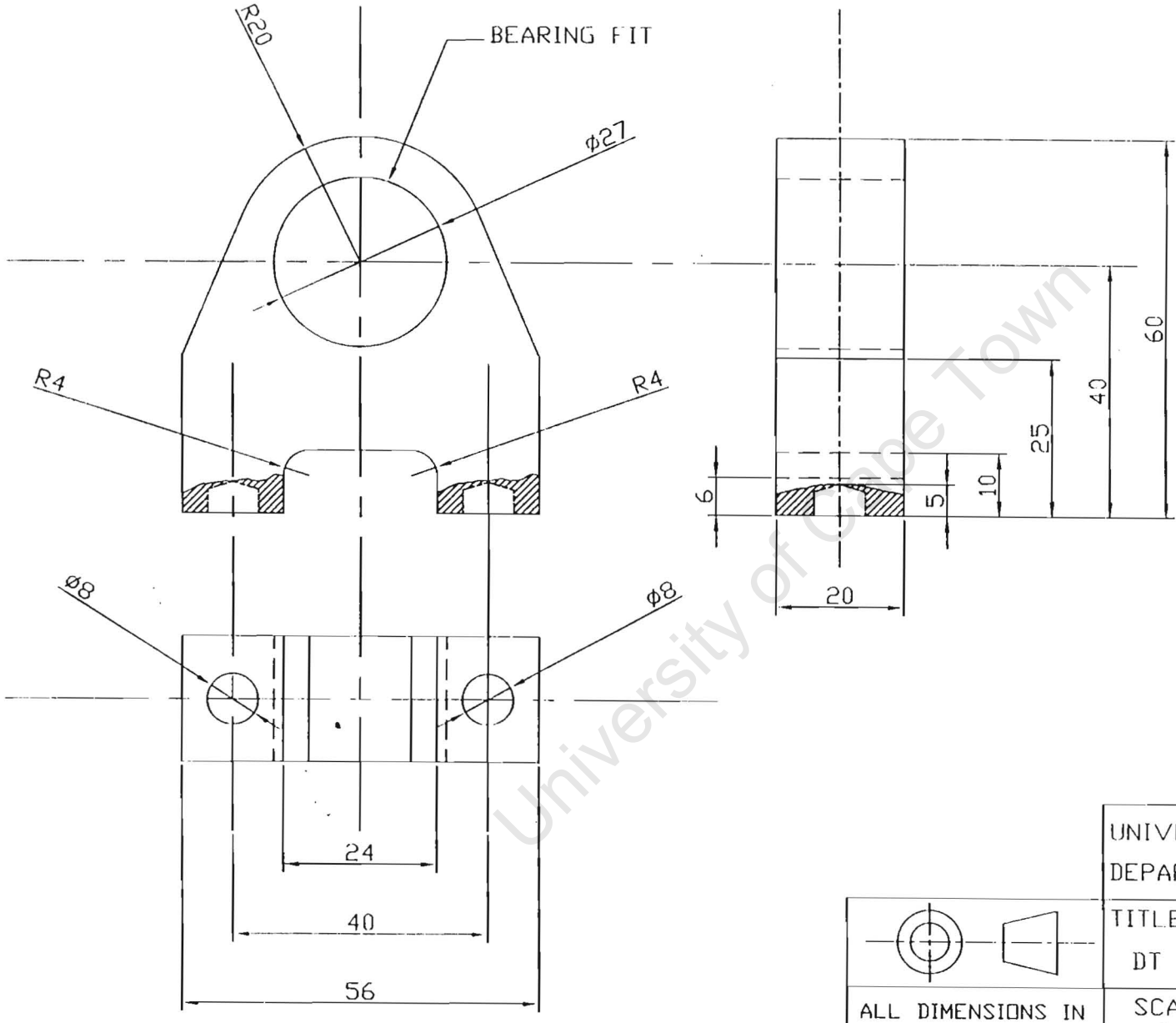

NOTES :

1. SKF BEARING NKI 15/20 TO BE FITTED IN 27 mm DIAMETER HOLE
2. 2 x 8mm DIAMETER HOLES TO BE DRILLED IN UNDER SURFACE 5mm DEEP
3. TO BE MANUFACTURED FROM 431 STAINLESS STEEL MATERIAL
4. REMOVE ALL BURRS AND SHARP EDGES

	UNIVERSITY OF CAPE TOWN DEPARTMENT OF MECHANICAL ENGINEERING		
	TITLE DT UPPER / OUTER LOADING SPAN		
ALL DIMENSIONS IN MILLIMETRES TOLERANCES 0.1 mm	SCALE 1:1	DATE 29/08/01	SHEET 1 OF 1
	DRAWN BY T. NAIDU		DRAWING NUMBER

1. ROLLER SEAT :

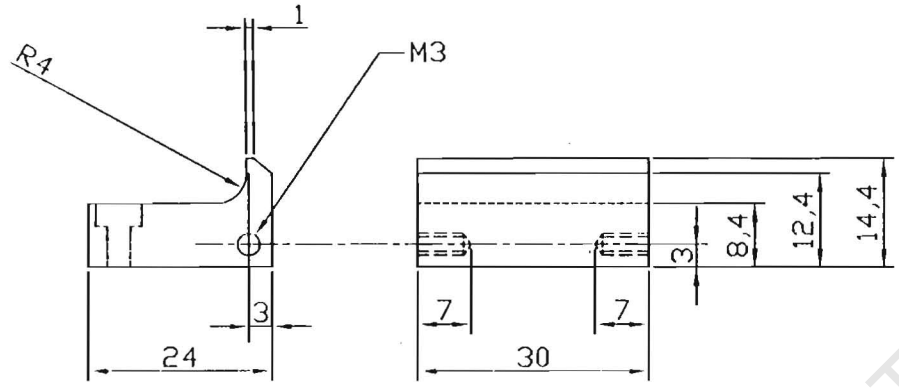

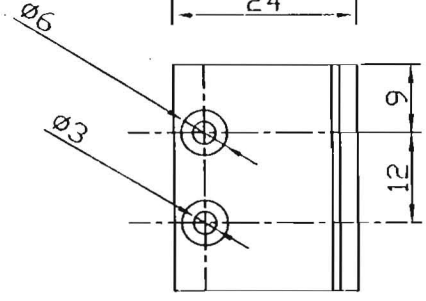

3. ROLLER NO. 2 :

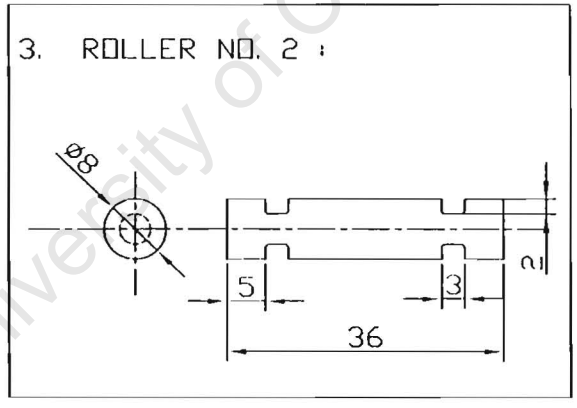

2. ROLLER NO. 1 :

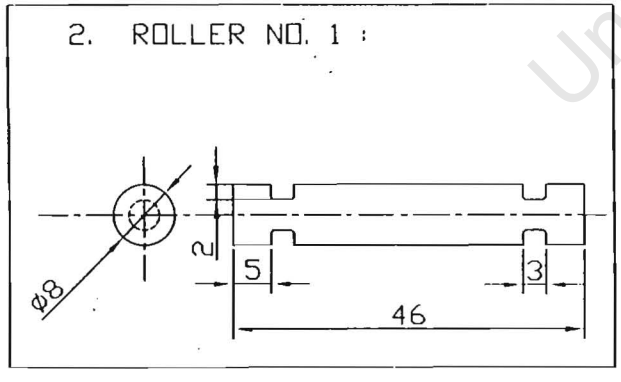

NOTES :

1. M3 HOLE TO BE THREADED 7 mm DEEP ON BOTH SIDES OF ROLLER SEATS
2. 6 mm HOLES TO BE DRILLED FROM TOP OF ROLLER SEATS 3 mm DEEP
3. 3 mm HOLES TO BE DRILLED THROUGH THE ENTIRE TOP THICKNESS
4. REMOVE ALL BURRS AND SHARP EDGES
5. ROLLER SEATS TO BE HARDENED AFTER MACHINING

PART NO.	DESCRIPTION	MATERIAL	NO. OFF
3.	ROLLER NO. 2	EJECTOR PINS	2
2.	ROLLER NO. 1	EJECTOR PINS	2
1.	ROLLER SEATS	GAUGE PLATE	2

UNIVERSITY OF CAPE TOWN
DEPARTMENT OF MECHANICAL ENGINEERING

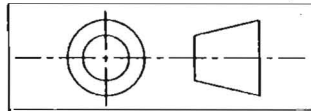

ALL DIMENSIONS IN MILLIMETRES
TOLERANCES 0.1 mm

TITLE
ROLLER SEATS and ROLLERS

SCALE	DATE	SHEET
1:1	29/08/01	1 OF 1

DRAWN BY
T. NAIDU

DRAWING NUMBER

1. SHAFT:

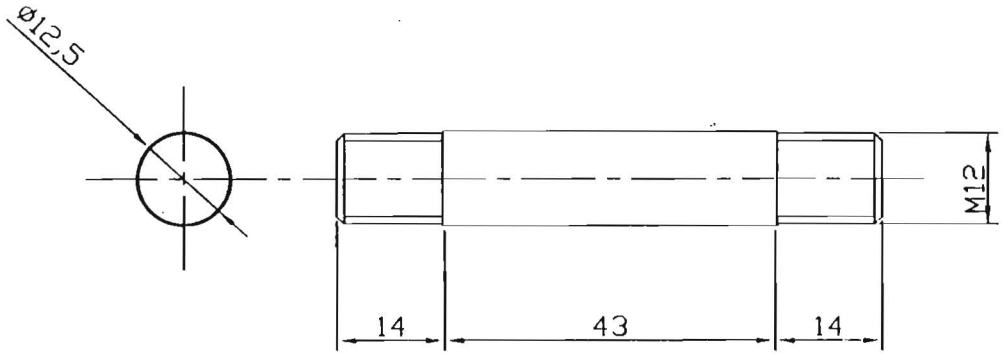

2. SLEEVE:

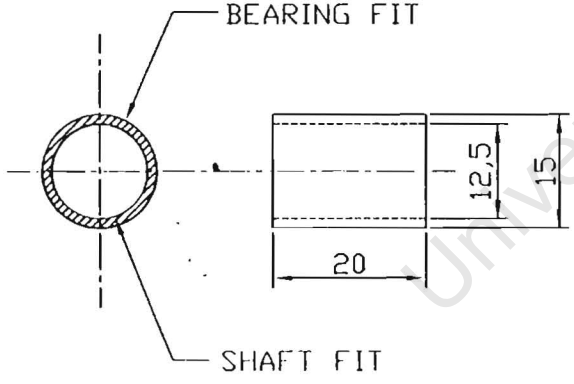

NOTES :

1. SLEEVE TO FIT ONTO INNER RING OF SKF BEARING NKI 15/20 WITH INNER DIAMETER 15 mm

2. SHAFT TO FIT INTO SLEEVE, WHICH MUST FIRST BE FITTED INTO BEARING

3. SHAFT TO BE THREADED M12 14 mm FROM BOTH ENDS

4. REMOVE ALL BURRS AND SHARP EDGES

PART NO.	DESCRIPTION	MATERIAL	NO. OFF
2.	SLEEVE	BRASS	2
1.	SHAFT	431 ST STEEL	2

UNIVERSITY OF CAPE TOWN
DEPARTMENT OF MECHANICAL ENGINEERING

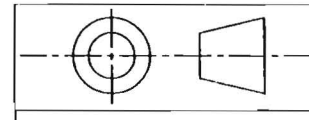

TITLE
SHAFT and SLEEVE

ALL DIMENSIONS IN MILLIMETRES TOLERANCES ????	SCALE 1:1	DATE 29/08/01	SHEET 1 OF 1
	DRAWN BY T. NAIDU		DRAWING NUMBER

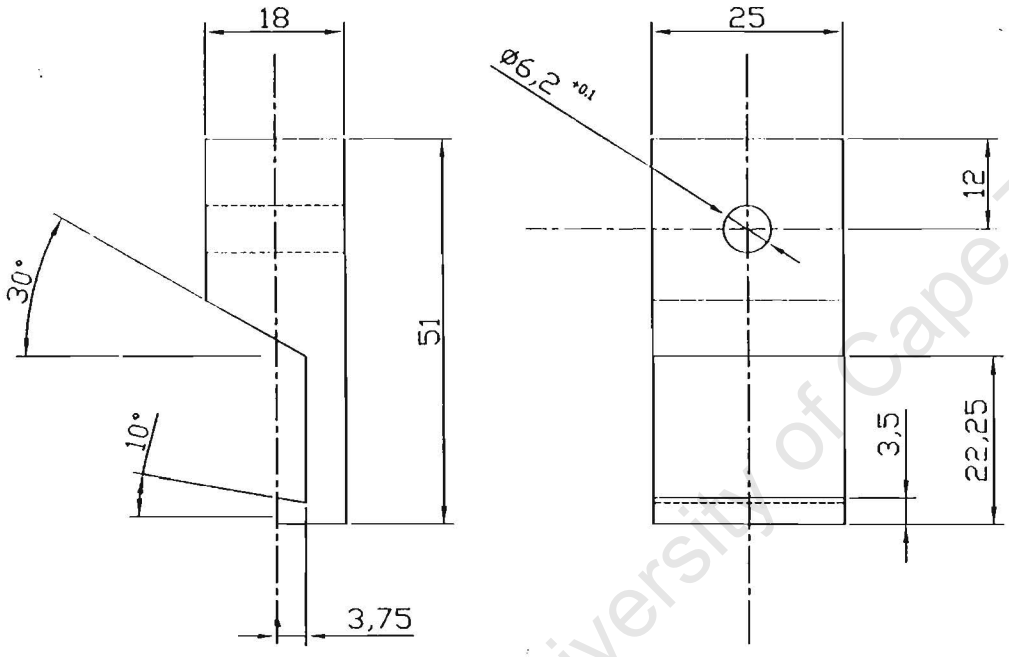

NOTES :

1. TO BE MANUFACTURED FROM 431 STAINLESS STEEL
2. REMOVE ALL BURRS AND SHARP EDGES
3. TO BE HARDENED AFTER MACHINING
4. QUANTITY = 2 OFF

	UNIVERSITY OF CAPE TOWN DEPARTMENT OF MECHANICAL ENGINEERING
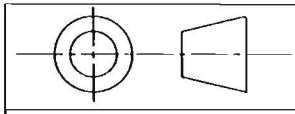	TITLE CHEVRON SHORT ROD LOADING GRIPS
ALL DIMENSIONS IN MILLIMETRES TOLERANCES 0.1 mm	SCALE / DATE 29/08/01 / SHEET 1 OF 1 DRAWN BY T. NAIDU / DRAWING NUMBER

APPENDIX D

Drawings for CVN specimen geometries

5. **CVNB specimen geometry**
6. **CVSR specimen geometry**

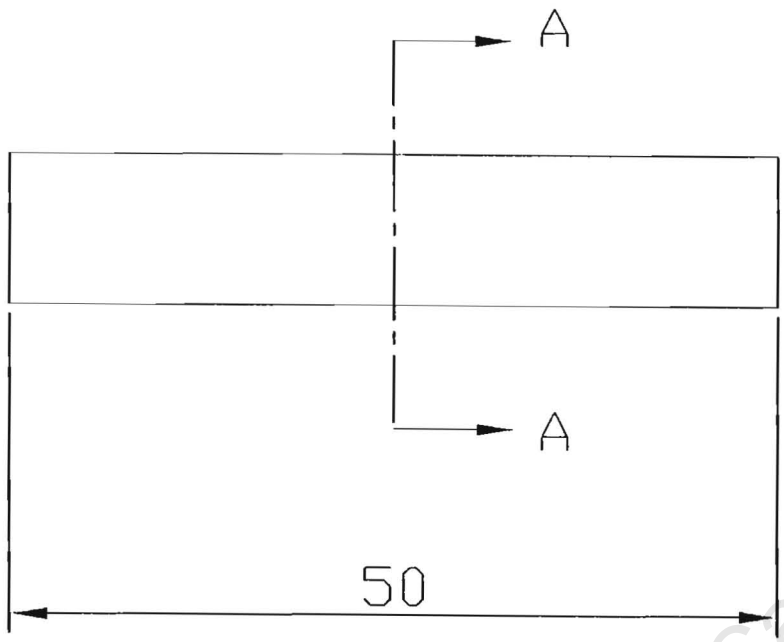

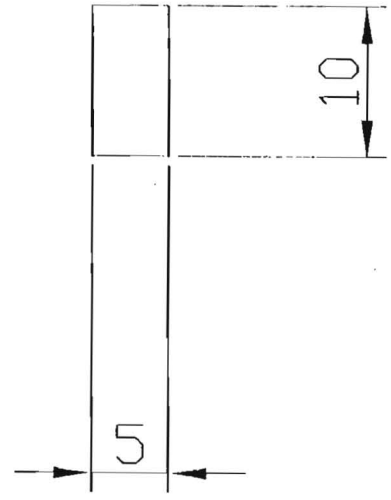

SECTION A-A

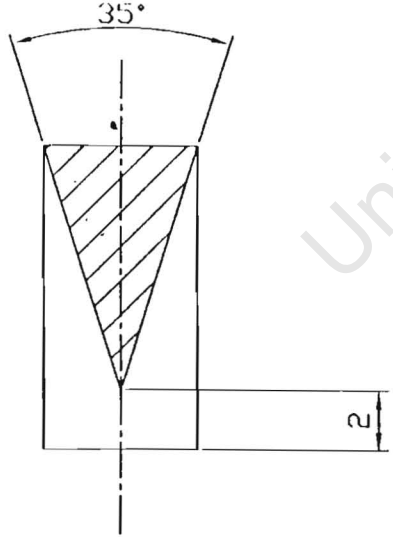

	UNIVERSITY OF CAPE TOWN DEPARTMENT OF MECHANICAL ENGINEERING		
	TITLE CHEVRON BEND BAR GEOMETRY		
ALL DIMENSIONS IN MILLIMETRES TOLERANCES 0.1 mm	SCALE	DATE 02/09/01	SHEET 1 OF 1
	DRAWN BY T. NAIDU		DRAWING NUMBER

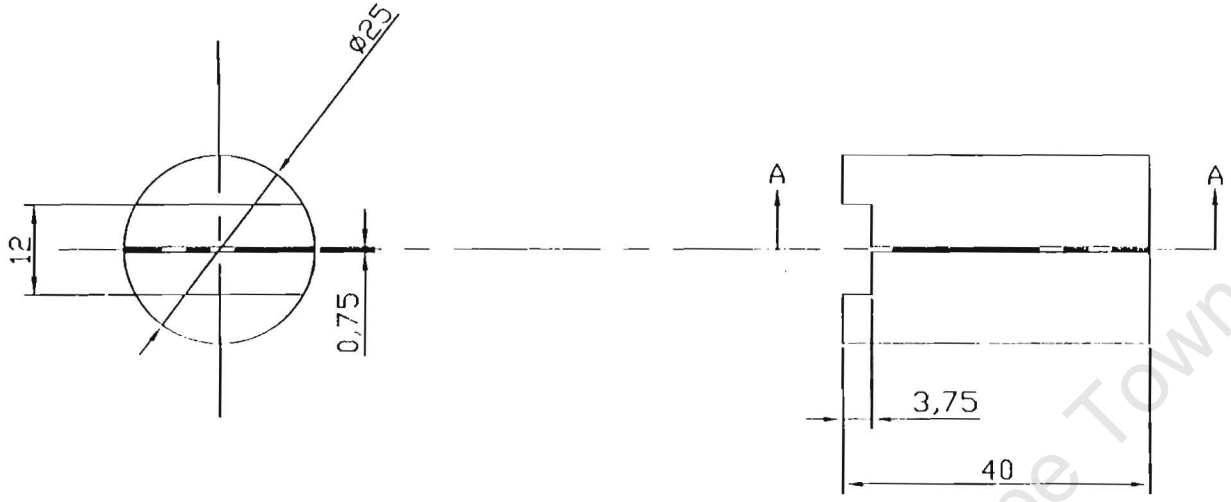

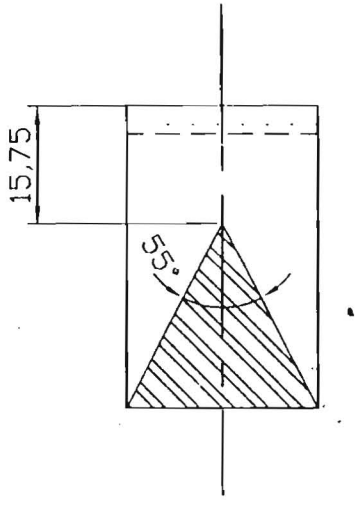

SECTION A-A

NOTES:

1. MATERIAL = ALUMINA CERAMIC; QUANTITY = 10 OF EACH ALUMINA TYPE

2. 0.43 mm DIAMOND BLADE TO BE USED TO MACHINE CHEVRON NOTCH

	UNIVERSITY OF CAPE TOWN DEPARTMENT OF MECHANICAL ENGINEERING		
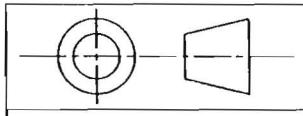	TITLE CHEVRON SHORT ROD GEOMETRY		
ALL DIMENSIONS IN MILLIMETRES TOLERANCES 0.1 mm	SCALE 1:1	DATE 29/08/01	SHEET 1 OF 1
	DRAWN BY T. NAIDU		DRAWING NUMBER

APPENDIX E

Raw data for IM tests

Indentation Microfracture (IM) Tests

Material	**MP 92**			
Indent load	196.2	***P***	N	
Young's mod	295	***E***	GPa	Multotec datasheet
Poissson's	0.21	**ν**	Matweb website	
Liang *f(ν)*	13.30178	**f(ν)**		

Indent no.	**Diagonal lengths**		**Avg. Diag.**	**Vickers**	**Crack lengths**				**Avg. crack**	**c/a**	**Anstis K_{Ia}**	**Liang K_{Ia}**
	$2a_1$	**$2a_2$**	**$2a$**	**Hardness**	**c_1**	**c_2**	**c_3**	**c_4**	**c**	**ratio**		
	microns	microns	microns	GPa	microns	microns	microns	microns	microns		MPam$^{1/2}$	MPam$^{1/2}$
1	179.69	182.64	181.165	11.08546	280.315	261.27	222.205	256.32	255.0275	2.815417	3.827131	3.999831
2	172.64	173.84	173.24	12.12289	249.24	221.86	287.7	272.62	257.855	2.976853	3.599684	3.864668
3	180.93	183.53	182.23	10.95627	249.965	294.725	242.485	216.365	250.885	2.753498	3.945366	4.090905
4	176.88	178.66	177.77	11.51292	289.32	269.34	225.86	209.58	248.525	2.796029	3.903758	4.086712
5	181.14	183.01	182.075	10.97493	254.06	243.805	254.85	205.795	239.6275	2.632185	4.223037	4.32315
6	171.1	175.55	173.325	12.111	240.43	194.165	274.68	200.875	227.5375	2.625559	4.344715	4.488602
7	170.53	172.92	171.725	12.33773	328.785	226.24	273.505	261.25	272.445	3.173038	3.285449	3.613916
8	172.59	170.88	171.735	12.3363	313.095	277.57	331.415	282.99	301.2675	3.508516	2.825595	3.235235
									avg	**2.91**	**3.74**	**3.96**
									std dev	**0.30**	**0.50**	**0.40**

Material	**MP 96**		
Indent load	196.2 ***P***	N	
Young's mod	330 ***E***	GPa	Multotec datasheet
Poissson's	0.21 **ν**	Matweb website	
Liang ***f(ν)***	13.30178 **f(ν)**		

Indent no.	**Diagonal lengths**		**Avg. Diag.**	**Vickers**	**Crack lengths**				**Avg. crack**	**c/a**	**Anstis K_{Ia}**	**Liang K_{Ia}**
	$2a_1$	**$2a_2$**	**$2a$**	**hardness**	**c_1**	**c_2**	**c_3**	**c_4**	**c**	**ratio**		
	microns	microns	microns	GPa	microns	microns	microns	microns	microns		MPam$^{1/2}$	MPam$^{1/2}$
1	181.76	171.85	176.805	11.63894	214.12	231.885	189.81	334.195	242.5025	2.743163	4.260354	4.389838
2	173.62	166.79	170.205	12.55908	229.42	228.155	235.87	261.315	238.69	2.804735	4.199973	4.389939
3	175.82	177.64	176.73	11.64882	219.68	201.03	240.13	251.58	228.105	2.581395	4.668029	4.728386
4	171.03	176.51	173.77	12.04905	237.315	216.225	253.485	247.685	238.6775	2.747051	4.288279	4.435802
5	172.48	178.54	175.51	11.81133	252.66	248.61	242.93	274.23	254.6075	2.901345	3.931159	4.127568
6	180.97	184.16	182.565	10.9161	229.825	235.88	258.015	260.09	245.9525	2.69441	4.306913	4.386412
									avg	**2.75**	**4.28**	**4.41**
									std dev	**0.11**	**0.24**	**0.19**

Material	**MP 99**			
Indent load	196.2	***P***	N	
Young's mod	340	***E***	GPa	Multotec datasheet
Poissson's	0.21	**ν**	Matweb website	
Liang *f(ν)*	13.30178	**f(ν)**		

Indent no.	**Diagonal lengths**		**Avg. Diag.**	**Vickers**	**Crack lengths**				**Avg. crack**	**c/a**	**Anstis K_{Ia}**	**Liang K_{Ia}**
	$2a_1$	**$2a_2$**	**$2a$**	**Hardness**	**c_1**	**c_2**	**c_3**	**c_4**	**c**	**ratio**		
	microns	microns	microns	GPa	microns	microns	microns	microns	microns		MPam$^{1/2}$	MPam$^{1/2}$
1	150.95	139.88	145.415	17.20616	165.655	112.11	214.925	167.16	164.9625	2.268851	6.339271	6.4507
2	145.99	156.45	151.22	15.9105	208.605	203.715	221.815	200.825	208.74	2.760746	4.631362	4.918333
3	142.4	143.59	142.995	17.79347	222.73	-	218.7	180.945	207.45833	2.901617	4.420104	4.820798
4	142	142.43	142.215	17.98919	226.98	206.955	179.22	148.145	190.325	2.676581	5.002759	5.329967
5	146.44	148.07	147.255	16.77886	198.56	171.325	211.54	142.915	181.085	2.459475	5.581543	5.77344
6	152.8	154.47	153.635	15.41424	179.21	217.295	222.34	199.075	204.48	2.661893	4.85313	5.083343
7	151.12	155.9	153.51	15.43935	186.88	240.67	209.72	228.22	216.3725	2.819002	4.454937	4.746815
8	152.64	149.48	151.06	15.94423	244.05	181.39	179.61	189.93	198.745	2.631339	4.979814	5.216801
									avg	**2.65**	**5.03**	**5.29**
									std dev	**0.20**	**0.65**	**0.57**

APPENDIX F

Raw data for ISB tests

Indentation strength in bending (ISB) data

Material	**MP 92**			
Outer span	40	S_1	mm	
Inner span	20	S_2	mm	
Stiffness	295	E	GPa	Multotec datasheet
Hardness	10.04	H	GPa	5kg load, Multotec datasheet
Indent load	196.2	P	N	

	Dimensions		Max load	Max stress	
Specimen	B	W	P_{max}	σ_f	K_{Ic}
	mm	**mm**	**kN**	**MPa**	**MPa.m$^{1/2}$**
1	5.76	10.82	2.522	112.20	3.67
2	5.68	10.88	2.471	110.25	3.63
3	5.6	10.8	2.685	123.32	3.94
4	5.56	10.68	2.45	115.90	3.76
5	5.66	10.72	2.493	114.98	3.74
6	5.68	10.7	2.331	107.53	3.56
7	5.58	10.82	2.633	120.92	3.89
8	5.5	10.8	2.467	115.37	3.75
9	5.78	10.7	2.646	119.95	3.86
10	5.68	10.8	2.629	119.05	3.84
11	5.8	10.68	2.382	108.02	3.57
Averages	5.66	10.76	2.519	115.23	**3.75**
Std. Dev.	0.10	0.07	0.115	5.30	**0.13**

Material	**MP 96**			
Stiffness	330	E	GPa	Multotec datasheet
Hardness	12.53	H	GPa	5kg load, Multotec datasheet
Indent load	196.2	P	N	

	Dimensions		Max load	Max stress	
Specimen	B	W	P_{max}	σ_f	K_{Ic}
	mm	**mm**	**kN**	**MPa**	**MPa.m$^{1/2}$**
1	6.2	10.48	3.277	144.37	4.38
2	5.92	10.7	3.326	147.22	4.44
3	6.08	10.48	3.283	147.49	4.45
4	6.12	10.7	3.392	145.23	4.40
5	6.08	10.6	3.151	138.37	4.24
6	5.98	10.7	3.153	138.16	4.24
7	6.04	10.8	3.184	135.58	4.18
8	6.08	10.68	3.389	146.60	4.43
9	6.08	10.68	3.411	147.56	4.45
10	6.2	10.6	3.355	144.48	4.38
11	6.08	10.62	3.388	148.22	4.46
Averages	6.08	10.64	3.301	143.94	**4.37**
Std. Dev.	0.08	0.10	0.099	4.45	**0.10**

Material	**MP 99**			
Stiffness	340	*E*	GPa	Multotec datasheet
Hardness	16.20	*H*	GPa	5kg load, Multotec datasheet
Indent load	196.2	*P*	N	

	Dimensions		Max load	Max stress	
Specimen	***B***	***W***	P_{max}	σ_f	K_{Ic}
	mm	**mm**	**kN**	**MPa**	**MPa.m$^{1/2}$**
1	5.33	9.72	1.954	116.40887	3.620547
2	5.49	10.03	2.023	109.88614	3.467303
3	5.33	9.73	1.92	114.14834	3.567688
4	5.46	9.97	2.094	115.74839	3.605129
5	5.46	10	2.057	113.02198	3.541252
6	5.47	9.98	2.101	115.69082	3.603784
7	5.34	9.74	1.973	116.83936	3.630584
8	5.46	9.97	2.097	115.91422	3.609002
9	5.48	10.02	2.18	118.86712	3.677739
10	5.35	10.03	2.012	112.14853	3.520706
11	5.37	9.96	2.116	119.16369	3.684619
12	5.14	10.15	2.154	122.03144	3.750925
13	5.33	10.16	2.295	125.13803	3.822316
14	5.35	10.08	2.008	110.81795	3.489331
15	5.73	10.03	2.165	112.67373	3.533065
Averages	5.41	9.97	2.077	115.90	**3.61**
Std. Dev.	0.13	0.14	0.099	4.15	**0.10**

APPENDIX G

Raw data for SENB tests

Single Edge Notched Bend Bar (SENB) data

Outer span	40	S_1	mm
Inner span	20	S_2	mm
	3.141593	*pi*	
	2.718282	*e*	

Material MP 92
Test SENB - S

Specimen	Dimensions B mm	W mm	Notch depth a mm	α	Tip width 2ρ mm	T_M	P_{max} kN	K_{Ic} MPa.m$^{1/2}$
1	5.66	10.76	4.58	0.43	0.525	1.007929	0.528	3.781363
2	5.64	10.86	4.70	0.43	0.575	0.999381	0.5502	3.979757
3	5.78	10.8	4.53	0.42	-	1.015039	0.597	4.09569
4	5.6	10.66	4.50	0.42	0.5	1.011406	broke during setup	
5	5.64	10.84	4.65	0.43	0.5	1.003652	0.5504	3.95166
6	5.58	10.84	4.63	0.43	0.5	1.006256	0.6002	4.328833
7	5.8	10.8	4.53	0.42	0.7	1.015039	0.5872	4.014566
8	5.7	10.8	4.65	0.43	0.5	1.001867	0.5474	3.927022
9	5.94	10.8	4.50	0.42	0.525	1.017721	0.5948	3.946553
10	5.78	10.82	4.60	0.43	0.5	1.007982	0.5214	3.625743
11	5.7	10.76	4.58	0.43	0.5	1.007929	0.5492	3.905589
Averages	5.71	10.79	4.58	0.42	**0.53**	1.008564	0.563	**3.96**
Std. Devs.	0.11	0.05	0.07	0.01	**0.06**	0.005793	0.030	**0.18**

Material MP 96
Test SENB - S

Specimen	Dimensions B mm	W mm	Notch depth a mm	α	Tip width 2ρ mm	T_M	P_{max} kN	K_{Ic} MPa.m$^{1/2}$
1	6.02	10.76	4.55	0.42	0.5	1.010578	0.7358	4.923981
2	6.15	10.87	4.55	0.42	0.5	1.015499	0.7328	4.674405
3	5.94	10.67	4.33	0.41	0.5	1.031077	0.7336	4.812253
4	6.06	10.86	4.53	0.42	0.5	1.017721	0.7684	4.956089
5	6.08	10.38	4.35	0.42	0.5	1.01493	0.7004	4.849199
6	5.86	10.7	4.58	0.43	0.5	1.005227	0.692	4.857785
7	5.99	10.9	4.75	0.44	0.5	0.996052	0.7402	5.054129
8	6.08	10.67	4.58	0.43	0.5	1.003871	0.7104	4.842295
9	5.93	10.65	4.48	0.42	0.5	1.013647	0.7392	5.063859
10	6.07	10.43	4.05	0.39	0.55	1.051918	0.7586	4.822603
11	6.05	10.89	4.60	0.42	0.5	1.0111	0.7106	4.64167
12	6.11	10.57	4.50	0.43	0.5	1.007307	0.7816	5.333498
Averages	6.03	10.70	4.49	0.42	**0.50**	1.01491	0.734	**4.90**
Std. Devs.	0.08	0.17	0.18	0.01	**0.01**	0.01447	0.027	**0.19**

Material MP 99
Test SENB - S

Specimen	Dimensions B mm	W mm	Notch depth a mm	α	Tip width 2ρ mm	T_M	P_{max} kN	K_{Ic} MPa.m$^{1/2}$
1	5.5	9.75	4.15	0.425641	0.475	1.007412	0.5024	4.297885
2	5.26	9.74	4.375	0.449179	0.5	0.981498	0.5316	5.075335
3	5.5	9.74	4.2	0.431211	0.5	1.001133	0.4734	4.116793
4	5.25	9.71	4.2	0.432544	0.5	0.999645	0.495	4.546744
5	5.26	9.75	4.35	0.446154	0.5	broke during test setup		
6	5.5	9.76	4.325	0.443135	0.5	0.987998	0.4468	4.000339
7	5.26	9.72	4.225	0.434671	0.5	0.99728	0.4492	4.135432
8	5.47	9.97	4.45	0.446339	0.5	0.984539	0.4492	3.951213
9	5.25	9.72	4.2	0.432099	0.5	broke during test setup		
10	5.45	9.97	4.5	0.451354	0.5	0.979183	0.5262	4.709959
11	5.5	9.75	4.1	0.420513	0.5	1.013273	0.5224	4.408645
12	5.5	9.69	4.225	0.436017	0.5	0.99579	0.4956	4.399709
Averages	5.39	9.77	4.28	0.44	**0.50**	0.994775	0.489	**4.36**
Std. Devs.	0.12	0.09	0.12	0.01	**0.01**	0.01	0.033	**0.35**

Material MP 92
Test SEVNB

Specimen	Dimensions B mm	W mm	Notch depth a mm	α	Tip width 2ρ mm	T_M	P_{max} kN	K_{Ic} MPa.m$^{1/2}$
1	6	10.76	4.95	0.460037	0.25	0.970077	0.44	3.268596
2	5.82	10.8	Invalid test => calibration / plot problems					
3	5.66	10.88	4.93	0.45	0.25	0.977794	0.4228	3.20814
4	5.56	10.74	4.90	0.46	0.25	0.974035	0.3904	3.105328
5	5.82	10.83	4.88	0.45	0.25	0.980475	0.4402	3.248143
6	5.6	10.88	4.93	0.45	0.3	0.977794	0.3842	2.946484
7	5.76	10.67	4.61	0.43	0.3	0.999931	0.4284	3.11146
8	5.68	10.85	4.88	0.45	0.3	0.981359	0.4288	3.225679
9	5.8	10.85	4.91	0.45	0.35	0.977689	0.379	2.8188
10	5.75	10.84	4.93	0.45	0.35	0.976032	0.4578	3.454218
11	5.8	10.8	4.85	0.45	0.35	0.981609	0.4196	3.110648
Averages	5.75	10.81	4.88	0.45	**0.30**	0.97968	0.419	**3.15**
Std. Devs.	0.12	0.06	0.10	0.01	**0.04**	0.007929	0.026	**0.18**

Material MP 96
Test SEVNB

Specimen	Dimensions B mm	W mm	Notch depth a mm	α	Tip width 2ρ mm	T_M	P_{max} kN	K_{Ic} MPa.m$^{1/2}$
1	6.06	10.8	5.03	0.47	0.35	0.964683	0.50958	3.782455
2	6.01	10.63	4.55	0.43	0.3	1.004703	0.53352	3.692487
3	5.97	10.77	4.88	0.45	0.375	0.977815	0.49932	3.647003
4	6.12	10.53	4.63	0.44	0.3	0.992264	0.527535	3.747661
5	6.09	10.44	4.73	0.45	0.3	0.977878	0.50844	3.813771
6	6.01	10.81	5.08	0.47	0.3	0.960419	0.497325	3.761431
7	5.94	10.57	4.80	0.45	0.35	0.976264	0.4674	3.54332
8	6.08	10.64	4.85	0.46	0.3	0.974466	0.52326	3.85553
9	6.07	10.55	4.66	0.44	0.35	0.989293	0.53181	3.826492
10	5.92	10.53	4.79	0.45	0.3	0.975698	0.479085	3.670425
Averages	6.03	10.63	4.80	0.45	**0.32**	0.979348	0.508	**3.73**
Std. Devs.	0.07	0.13	0.17	0.01	**0.03**	0.013052	0.022	**0.10**

Material MP 99
Test SEVNB

Specimen	Dimensions B mm	W mm	Notch depth a mm	α	Tip width 2ρ mm	T_M	P_{max} kN	K_{Ic} MPa.m$^{1/2}$
1	5.65	9.96	4.45	0.446787	0.275	0.984058	0.422	3.603535
2	5.64	10.06	4.8	0.477137	0.275	0.952753	0.3656	3.35484
3	5.14	10.14	4.6625	0.459813	0.275	broke during test setup		
4	5.67	9.94	4.475	0.450201	0.325	0.980408	0.4146	3.571843
5	5.53	9.95	4.45	0.447236	0.35	0.983576	0.442	3.86679
6	5.64	9.95	4.3	0.432161	0.35	1.000072	0.441	3.631299
7	5.36	9.98	4.6375	0.464679	0.4	0.965295	0.4102	3.868763
8	5.56	10.03	4.275	0.426221	0.425	1.006753	0.459	3.728479
9	5.65	10.06	4.45	0.442346	0.4	0.988855	0.4544	3.776422
10	5.73	10.15	4.525	0.445813	0.5	broke during test setup		
11	5.36	9.98	4.375	0.438377	0.45	0.993191	0.4646	4.075009
12	5.36	9.98	4.8	0.480962	0.5	0.948987	0.4006	3.958114
Averages	5.52	10.02	4.52	0.45	**0.38**	0.980395	0.427	**3.74**
Std. Devs.	0.18	0.07	0.18	0.02	**0.08**	0.019204	0.031	**0.21**

APPENDIX H

Raw data for DT tests

Double torsion (DT) test data

	2.718282	e	
	3.141593	π	
Displ. rate	0.000001	$\delta y/\delta t$	m/s

Material	**MP 92**		
Outer span	40	S_1	mm
Inner span	8	S_2	mm
Moment arm	16	W_m	mm
Poiss. Ratio	0.21	ν	
Shear Mod.	121.9008	μ	GPa

Specimen number	Dimensions t	W	Corr. fact ζ	eqn 3.9 Theoretical $B = dC/da$	Notch a_0	dist from edge, b	Loads from plots P_{max}	P_{const}	@P_{const} $K_I(P_{const})$	$\delta a/\delta t$	@P_{max} G_{Ic} (P_{max})	K_{Ic}
-	mm	mm	-	N^{-1}	mm	mm	N	N	$MPa.m^{1/2}$	$mm.s^{-1}$	$J.m^{-2}$	$MPa.m^{1/2}$
1	5.43	48.52	0.86	9.44E-07	51.74	44.20	545	365	invalid	invalid	invalid	invalid
2	5.48	48.59	0.86	9.18E-07	50.90	14.54	505	436	2.22	2.497	21.37105	2.510869
3	5.56	48.62	0.86	8.81E-07	51.18	8.14	540	450	2.22	2.523	23.09896	2.610401
4	5.86	48.56	0.85	7.60E-07	51.24	0.00	575	465	2.08	2.828	21.45091	2.515556
5	5.92	48.62	0.85	7.38E-07	50.40	8.70	585	495	2.17	2.738	21.32506	2.508165
6	5.12	48.53	0.87	1.12E-06	31.40	72.46	600	600	invalid	invalid	invalid	invalid
7	5.57	48.56	0.86	8.78E-07	50.78	24.00	585	475	2.34	2.399	26.96208	2.82025
8	5.71	48.62	0.85	8.17E-07	50.18	28.72	614	538	2.53	2.275	26.96956	2.820642
9	5.75	48.61	0.85	8.01E-07	50.50	0.00	545	485	2.25	2.573	20.69365	2.470754
10	5.29	48.57	0.86	1.02E-06	50.96	0.00	522	450	2.45	2.188	26.15791	2.777874
Averages	5.57	48.58	0.86				**562**	**476**	**2.28**	**2.50**	**23.50**	**2.63**
Std. Devs.	0.25	0.04	0.01				**35**	**62**	**0.15**	**0.22**	**2.74**	**0.15**

Material **MP 96**
Poiss. Ratio 0.21 ν
Shear Mod. 136.3636 μ GPa

Specimen number	Dimensions t	W	Corr. fact ζ	eqn 3.9 Theoretical $B = dC/da$	Notch a_0	dist from edge, b	Loads from plots P_{max}	P_{const}	@P_{const} $K_I(P_{const})$	$\delta a/\delta t$	@P_{max} G_{Ic} (P_{max})	K_{Ic}
-	mm	mm	-	N^{-1}	mm	mm	N	N	$MPa.m^{1/2}$	$mm.s^{-1}$	$J.m^{-2}$	$MPa.m^{1/2}$
1	5.41	48.51	0.86	8.53E-07	50.16	0.00	715	690	3.60	1.699	40.30981	3.647223
2	5.43	48.58	0.86	8.43E-07	49.76	5.70	695	662.5	3.43	1.791	37.48795	3.517247
3	5.43	48.61	0.86	8.42E-07	53.66	0.00	725	690	3.57	1.721	40.76487	3.667752
4	5.76	48.54	0.85	broke in set-up		-	-	-	invalid	invalid	invalid	invalid
5	5.94	48.60	0.85	broke in set-up		-	-	-	invalid	invalid	invalid	invalid
6	5.30	48.51	0.86	9.04E-07	50.38	0.00	650	597.5	3.24	1.851	36.04701	3.448987
7	5.66	48.53	0.85	7.50E-07	51.60	19.94	813	795	3.80	1.676	43.81149	3.80234
8	5.71	48.56	0.85	7.31E-07	50.96	0.00	712	682	3.21	2.005	32.46644	3.273214
9	5.61	48.57	0.85	7.69E-07	50.50	0.00	702	676	3.29	1.925	33.76105	3.337836
10	5.21	48.50	0.86	9.50E-07	50.56	42.56	857	647	invalid	invalid	invalid	invalid
11	5.60	48.42	0.85	7.75E-07	29.42	83.54	855	855	invalid	invalid	invalid	invalid
12	5.13	48.41	0.87	9.95E-07	51.60	72.90	missing	-	invalid	invalid	invalid	invalid
13	5.32	48.44	0.86	8.96E-07	50.18	0.00	649	621.5	3.35	1.795	35.47958	3.421734
Averages	5.50	48.52	0.86				**737**	**692**	**3.44**	**1.81**	**37.52**	**3.51**
Std. Devs.	0.24	0.07	0.01				**77**	**78**	**0.21**	**0.11**	**3.85**	**0.18**

Material **MP 99**
Poisson's r 0.21 ν
Shear Mod 140.4959 μ GPa

Specimen number	Dimensions t	W	Corr. fact ζ	eqn 3.9 Theoretical $B = dC/da$	Notch a_0	dist from edge, b	Loads from plots P_{max}	P_{const}	@P_{const} $K_I(P_{const})$	$\delta a/\delta t$	@P_{max} G_{Ic} (P_{max})	K_{Ic}
-	mm	mm	-	N^{-1}	mm	mm	N	N	$MPa.m^{1/2}$	$mm.s^{-1}$	$J.m^{-2}$	$MPa.m^{1/2}$
1	5.35	47.60	0.86	8.74E-07	50.46	19.48	583	536.5	2.89	2.133	27.75393	3.071862
2	5.29	47.60	0.86	9.02E-07	47.72	10.40	556	530	2.92	2.092	26.35884	2.993661
3	5.57	47.60	0.85	7.80E-07	49.92	12.22	672	547	2.73	2.345	31.59932	3.277769
4	5.50	47.62	0.85	8.08E-07	49.96	10.90	631	545	2.78	2.272	29.22882	3.152427
5	5.61	47.61	0.85	7.64E-07	50.58	0.00	620	535	2.63	2.447	26.16524	2.982647
6	5.16	47.62	0.86	9.68E-07	49.16	0.00	527	500	2.89	2.067	26.04208	2.975619
7	5.20	47.61	0.86	9.47E-07	49.42	33.26	535	455	invalid	invalid	invalid	invalid
8	5.51	47.62	0.85	8.03E-07	50.64	23.94	608	505	2.57	2.465	26.94875	3.026974
9	5.22	47.62	0.86	9.36E-07	49.22	0.00	578	500	2.82	2.136	29.96583	3.191925
10	5.26	47.60	0.86	9.17E-07	49.70	0.00	555	480	2.67	2.272	26.84364	3.021066
11	5.25	47.64	0.86	9.21E-07	30.26	82.34	704	704	invalid	invalid	invalid	invalid
12	5.14	47.61	0.86	9.79E-07	49.22	15.40	526	431	2.51	2.371	26.33975	2.992577
Averages	5.34	47.61	0.86				**591**	**522**	**2.74**	**2.26**	**27.72**	**3.07**
Std. Devs.	0.17	0.01	0.00				**57**	**68**	**0.14**	**0.15**	**1.91**	**0.10**

APPENDIX I

Raw data for CVNB tests

Chevron Notched Bend Bar (CVNB) data

Material **MP 92**
Outer span 40 S_1 mm
Inner span 20 S_2 mm
1 α_1

	Dimensions		Chevron notch					
Specimen	***B***	***W***	a_0	α_0	$0.07<\alpha_0<0.37$	Y^*_m	P_{max}	K_{Ic}
	mm	mm	mm	–	yes/no	-	kN	$MPam^{1/2}$
1	5.65	10.86	1.4875	0.137	yes	7.353	broke in setup	
2	5.76	10.82	1.6	0.148	yes	7.532	0.243	3.05
3	5.77	10.83	1.35	0.125	yes	7.207	0.294	3.53
4	5.435	10.82	2.725	0.252	yes	9.162	0.147	2.38
5	5.61	10.86	very badly machined chevron notch - offcentre					
6	5.95	10.75	1.65	0.153	yes	7.662	0.240	2.98
7	5.645	10.78	1.35	0.125	yes	7.249	0.303	3.74
8	5.62	10.68	0.9	0.084	yes	6.791	broke in setup	
9	5.67	10.76	2.7	0.251	yes	9.198	broke in setup	
Average	5.68	10.80	1.72	0.16		7.769	0.245	**3.14**
Std. Dev	0.14	0.06	0.65	0.06		0.908	0.062	**0.53**

Material **MP 96**
Outer span 20 S_1 mm
Inner span 40 S_2 mm
1 α_1

	Dimensions		Chevron notch					
Specimen	***B***	***W***	a_0	α_0	$0.07<\alpha_0<0.37$	Y^*_m	P_{max}	K_{Ic}
	mm	mm	mm	–	yes/no	-	kN	$MPam^{1/2}$
1	6.06	10.69	1.05	0.098	yes	6.958	0.326	3.62
2	5.99	10.07	0.75	0.074	yes	7.085	0.300	3.53
3	6.08	10.44	0.75	0.072	yes	6.797	0.307	3.36
4	5.81	10.07	0.575	0.057	no	6.871	0.290	invalid
5	6.07	10.44	0.55	0.053	no	6.572	0.450	invalid
6	6.13	10.8	0.875	0.081	yes	6.675	0.393	4.12
7	6.06	10.9	1.1	0.101	yes	6.855	0.387	4.19
8	6.1	10.68	1.3	0.122	yes	7.271	0.338	3.90
9	6.085	10.63	1.7	0.160	yes	7.844	broke during setup	
10	5.95	10.79	1.85	0.171	yes	7.894	0.333	4.25
11	6.06	10.63	0.9	0.085	yes	6.829	0.421	4.60
Average	6.04	10.56	1.04	0.10		7.059	0.354	**3.95**
Std. Dev	0.09	0.28	0.43	0.04		0.442	0.055	**0.42**

Material **MP 99**

Outer span 40 S_1 mm

Inner span 20 S_2 mm

1 α_1

	Dimensions		Chevron notch					
Specimen	***B***	***W***	a_0	α_0	$0.07<\alpha_0<0.37$	Y^*_m	P_{max}	K_{Ic}
	mm	mm	mm	–	yes/no	-	kN	$MPam^{1/2}$
1	5.75	10.02	1.375	0.137	yes	7.985	0.260	3.61
2	5.63	9.97	1.4	0.140	yes	8.074	0.252	3.62
3	5.64	10.15	1.425	0.140	yes	7.927	0.247	3.45
4	5.74	10.03	1.55	0.155	yes	8.238	0.243	3.49
5	5.53	10.3	1.525	0.148	yes	7.922	0.254	3.58
6	5.53	10.29	1.4375	0.140	yes	7.807	0.257	3.57
7	5.52	10.29	1.35	0.131	yes	7.685	0.275	3.77
8	5.36	9.99	0.925	0.093	yes	7.379	0.289	3.98
9	5.36	9.97	0.85	0.085	yes	7.297	0.297	4.05
10	5.53	10.16	1.0125	0.100	yes	7.347	0.286	3.77
11	5.73	10.02	1.375	0.137	yes	7.985	broke during setup	
12	5.53	10.03	0.9	0.090	yes	7.311	0.299	3.95
Average	5.57	10.10	1.26	0.12		7.747	0.269	**3.71**
Std. Dev	0.13	0.13	0.26	0.03		0.333	0.021	**0.21**